SELF-PROPULSION OF CONTAMINATED MICROBUBBLES

A Thesis

Submitted to the Faculty

of

Purdue University

by

Nathaniel H. Brown

In Partial Fulfillment of the

Requirements for the Degree

of

Master of Science in Agricultural and Biological Engineering

May 2020

Purdue University

West Lafayette, Indiana

THE PURDUE UNIVERSITY GRADUATE SCHOOL
STATEMENT OF THESIS APPROVAL

Dr. Osvaldo H. Campanella, Co-Chair

    Department of Food Science and Technology, Ohio State University

Dr. Carlos M. Corvalan, Co-Chair

    Department of Food Science

Dr. Jiakai Lu

    Department of Food Science, University of Massachusetts

Dr. Nathan Mosier

    Department of Agricultural and Biological Engineering

Dr. Paul E. Sojka

    School of Mechanical Engineering

Approved by:

    Dr. Nathan Mosier

        Head of Graduate Program

ACKNOWLEDGMENTS

TABLE OF CONTENTS

LIST OF FIGURES

ABSTRACT

Brown, Nathaniel H. MSABE, Purdue University, May 2020. Self-propulsion of Contaminated Microbubbles. Major Professor: Dr. Osvaldo H. Campanella and Dr. Carlos M. Corvalan.

In many natural and industrial processes, bubbles are exposed to surface-active contaminants (surfactants) that may cover the whole or part of the bubble interface. A partial coverage of the bubble interface results in a spontaneous self-propulsion mechanism, which is yet poorly understood. The main goal of this study is to enhance the understanding of the flow and interfacial mechanisms underlying the self-propulsion of small surfactant contaminated bubbles. The focus is on characterizing the self-propulsion regimes generated by the presence of surface-active species, and the influence of surfactant activity and surface coverage on the active bubble motion. The study was developed by simultaneously solving the full system of partial differential equations governing the free-surface flow physics and the surfactant transport on the deforming bubble interface using multi-scale numerical simulation. Results show in microscopic detail how surface tension gradients (Marangoni stresses) induced by the uneven interfacial coverage produce spontaneous hydrodynamics flows (Marangoni flows) on the surrounding liquid, leading to bubble motion. Results also establish the influence of both surfactant activity and interfacial coverage on total displacement and average bubble velocity at the macroscale. Findings from this research improve the fundamental understanding of the free-surface dynamics of self-propulsion and the associated transport of surface-active species, which are critical to important natural and technological processes, ranging from the Marangoni propulsion of microorganisms to the active motion of bubbles and droplets in microfluidic devices. Overall, the findings advance our understanding of active matter behavior; that is, the behavior of

material systems with members able to transduce surface energy and mass transport into active movement.

1. INTRODUCTION

1.1 Overview

In a variety of natural and technological multi-phase systems, particles such as drops and bubbles are exposed to surface-active contaminants (surfactants) that may cover the whole, or part, of the particle interface. Since surfactants lower the surface tension, a partial coverage of the particle's interface creates an imbalance of forces leading to a spontaneous self-propulsion mechanism, which is yet poorly understood (Figure 1.1).

This thesis discusses, in detail, results from high-fidelity simulations to elucidate the flow and interfacial physics underlying the self-propulsion of small contaminated bubbles. Accurate numerical analysis incorporating all of the relevant phenomena that influence the active motion driven by gradients of surface tension were included to provide insight into the fundamental mechanisms of self-propulsion, and to probe variables that are not readily accessible in experiments. Results show, in microscopic detail, how surface tension gradients (Marangoni-stresses) induced by uneven interfacial coverage produce spontaneous hydrodynamic flows (Marangoni flows) on the surrounding liquid, leading to bubble motion. Results also establish the influence of both surfactant activity and interfacial coverage on the outer hydrodynamic flow, total bubble displacement, and bubble velocity at the macroscale (Figure 1.2).

Self-propulsion is the main feature of active matter, therefore a better understanding of the physics of self-propulsion is relevant to important natural and technological systems able to transduce surface energy into active movement, such as swimming microorganisms and autophoretic particles. Controlled active motion is also relevant to the Marangoni propulsion of drops and bubbles in sensors and microfluidic de-

vices. Moreover, better understanding of the spontaneous Marangoni flow regimes generated by active motion may provide insight into self-organization and collective dynamics of systems with many active members such as bacterial colonies, and the rheology of active colloid suspensions.

1.2 Research Objective and Thesis Outline

1.2.1 Research Objective

The overall goal of this thesis is to enhance the understanding of the fundamental flow physics and interfacial mechanisms underlying the Marangoni propulsion of small surfactant-laden bubbles, with focus on characterizing self-propulsion regimes, and the influence of surfactant activity and surface coverage on the active bubble motion (Figure 1.2).

Above all, the computational model used in this thesis also drives the discovery of previously unknown features of Marangoni propulsion that will offer opportunities for further research on this topic.

1.2.2 Thesis Outline

To analyze the spontaneous self-propulsion mechanism, and the effect of interfacial coverage and surfactant properties on the active bubble motion, a high-fidelity computational model is developed in Chapter 2. To enhance fidelity and accuracy, unnecessary simplifications in the computational model are avoided by simultaneously solving the full system of partial differential equations governing the free-surface flow physics and the surfactant transport on the deforming bubble interface.

The normal interfacial forces acting on the bubble interface are described using the Young-Laplace pressure jump, which links the normal capillary pressure across the interface to the shape (curvature) of the bubble. Critically, the tangential interfacial stress condition is extended to account for the development of viscous stresses in the
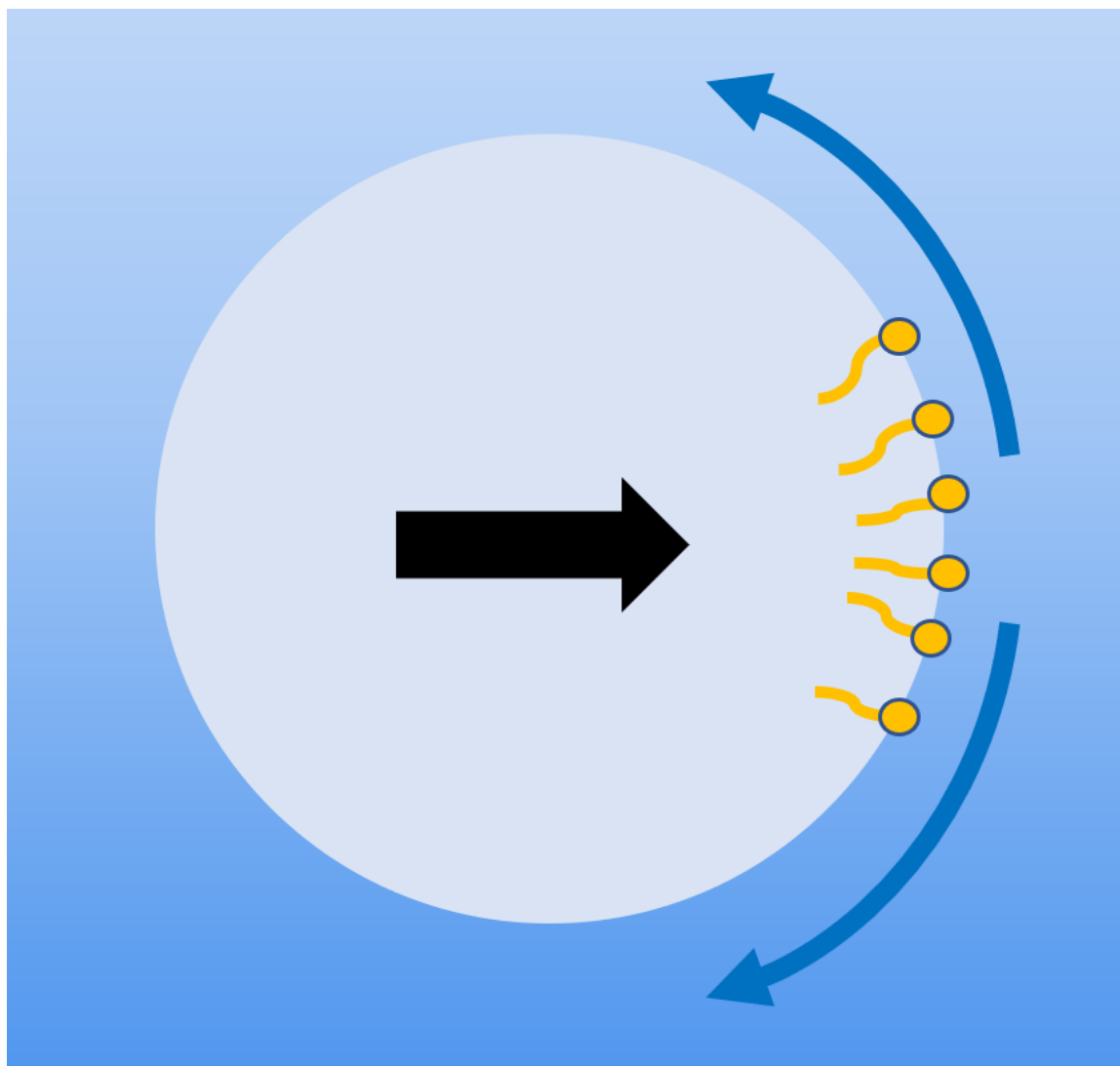
Fig. 1.1. **Self-propulsion of a small surfactant-laden bubble.** The uneven distribution of surface active species at the bubble interface generates surface tension gradients (blue arrows) leading to active bubble motion in the direction of the contaminated cap (black arrow).
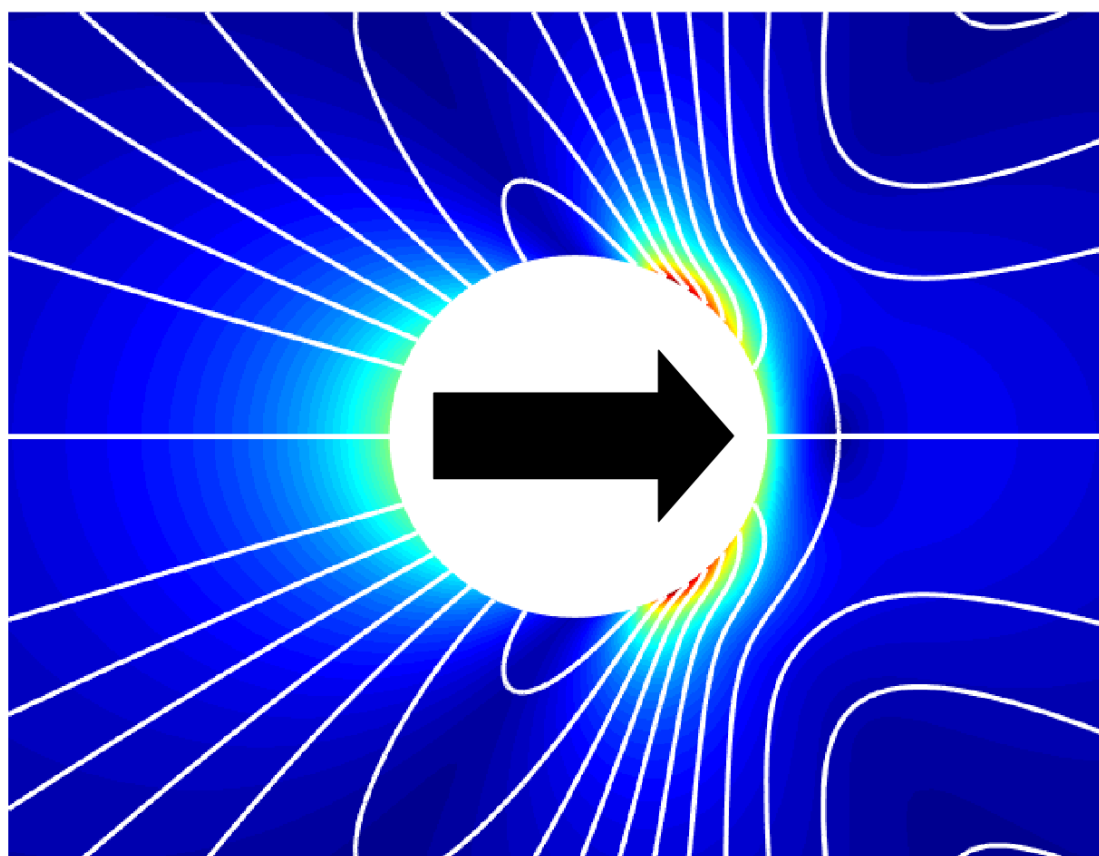
Fig. 1.2. **Cross sectional velocity field induced by active bubble motion.** Interfacial tension gradients (Marangoni stresses) produce hydrodynamic flows in the outer liquid through viscous momentum transfer, leading to bubble motion (black arrow). These direct numerical simulations accurately display the impact interfacial surfactant transport has on the external Marangoni flows associated with active motion.

bulk outer fluid induced by the surface tension gradients (Marangoni stresses) at the interface.

The Navier-Stokes equations governing the outer flow and the convection-diffusion equation governing the interfacial surfactant transport solved using the finite element method (FEM) for discretization in space, and finite difference for discretization in time with adaptive time step. To track the location of the deforming bubble interface, the model uses arbitrary Lagrangian-Eulerian method.

The second part of Chapter 2 presents the simulation results for self-propulsion of a small contaminated bubble in a highly-viscous liquid. By simultaneously solving the full system of governing equations, the simulations enable a detailed description of the microscopic physical mechanisms of self-propulsion. Initially, the simulations are benchmarked against the spreading of contaminant on interfaces from theoretical predictions from Jensen and Grotberg [1]. Then, results are used to explain in microscopic detail how surface tension gradients induced by the uneven interfacial coverage produce spontaneous hydrodynamic flows (Marangoni flows) on the surrounding bulk liquid, leading to bubble motion (Figure 1.2).

Chapter 3 extends the results of Chapter 2 to characterize parametrically the influence of material properties and initial conditions on Marangoni propulsion. The chapter provides a thorough quantitative study of the influence of the surfactant properties, the influence of neighboring solid boundaries, and the degree of surface contamination on both the microscopic mechanisms of self-propulsion and the overall bubble displacement and velocity at the macroscale.

Lastly, Chapter 4 offers concluding remarks along with recommendations for subsequent work while emphasizing the importance of examining experimentally previously unobserved features uncovered by the simulations.

1.3   Background

When a contaminant comes into contact with a bubble interface Marangoni flows are generated, created by uneven surface tension distributions, resulting in bubble propulsion. Marangoni-induced motion is a significant mechanism of motion seen in many natural and industrial processes.

The importance of Marangoni flows, which are integral to Marangoni-driven propulsion, was first studied by Carlo Marangoni who investigated these surface tension gradient induced flows for his dissertation. These surface tension differences can be created by a variety of means including differences in electric potentials, chemical concentrations, and temperatures at an interface. The Marangoni flows that propel small organisms and particles created by surfactants (surface-active agents) ([2], [3], [4]), has been thoroughly investigated for many decades because of how important and common this mechanism is in the environment, biomedical, and industrial food and pharmaceutical processes.

In the natural environment, the propulsion of some microorganisms depend on Marangoni flows ([5], [6]). Often, bacteria move by generating surfactant molecules on their interface to lower a localized surface tension on a bio-film [5]. This creates a gradient in surface tension, therefore inducing a Marangoni flow propelling the bacteria [5]. Marangoni driven propulsion is also seen in rove beetles where they release a surfactant to propel towards land if the insects were to accidentally fall into a body of water [7]. This Marangoni movement is significant for the existence of many natural organisms, in addition to aiding the natural environment. In an attempt of developing an environmental cleanup strategy for oil spills, multiple studies have used the mechanics of Marangoni propulsion of micro-capsules in the direction of surface active contaminant (oils) to assist in the cleanup and removal of oil from contaminated environments ([8], [9]). Self-propulsion due to interfacial surface tension gradients have previously been investigated in droplets where the surface tension gradients were

shown to generate internal spontaneous Marangoni flows along with external flows propelling the droplet in a viscous fluid [10].

Biomedical processes also utilize these surfactant induced Marangoni flows. An instance of the importance of self-driven propulsion in a biomedical process includes the movement of particles inside the body, driven by a diffusing solute on its interface, creating a surface tension gradient allowing for directed drug delivery ([11], [12], [13]). These Marangoni flows on microbubbles involved in gas embolisms have also previously been investigated in order to help develop therapeutic measures to reduce the possibility of an embolism ([14], [15]). These investigations of the Marangoni effect on microbubbles involved in gas embolisms are performed in close proximity to a wall, as discussed in Chapter 3, replicating the movement of the particle inside a vein or artery.

Active microbubbles play an important role in the cleaning of industrial and food processing equipment. Previous investigations show microbubble infused water is superior compared to traditional cleaning methods [16]. Physicochemical properties of bubbles of micro-scale or smaller posses a cleaning ability that is absent in bubbles of the milli-scale and larger ([17], [18], [19], [20]). The properties that microbubbles incorporate are smaller buoyant forces allowing for them to be submersed longer and the large microbubble surface to volume ratio provides a surface area capable of scavenging insoluble organic molecules in the water. Previous work [21] shows that surfactants play a large factor in altering the dynamics of bubble interactions. Microbubbles attach to grease and lipid molecules in cleaning processes [22]. Understanding the influence that surface active species have on the bubble movement is of considerable importance. Microbubbles can assist in providing answers to many industrial cleaning challenges with little environmental impact due to the simplicity of their production, the low material cost, and the possibility of cleaning without the addition of detergents [23]. The USDA Agriculture and Food Research Initiative for Food Manufacturing Technology supports the importance that this relatively new microbubble technology has on advancing food manufacturing technologies, and

understanding the mechanisms of motion involved with this technology will be imperative. Because of these needs, the USDA has funded part of this study.

Due to the importance of understanding the practical and fundamental significance of Marangoni flows, this work utilizes numerical simulations to advance the knowledge of previously unknown mechanisms of Marangoni flows while considering the interactions of interfacial dynamics and nearby tubular boundaries on the system.

2. SELF-PROPULSION OF CONTAMINATED MICROBUBBLES IN AN OUTER VISCOUS FLUID

In this chapter, the self-propulsion of a surfactant-laden bubble in a viscous liquid is studied using high-fidelity numerical simulations. Results from the simulations are used to characterize, in microscopic detail, how interfacial gradients induced by uneven surfactant coverage produce spontaneous Marangoni flows on the surrounding liquid, leading to active bubble motion. A previously unobserved transition in the macroscopic flow regime is also analyzed. Findings from this research improve the fundamental understanding of the free-surface dynamics of self-propulsion and the associated transport of surface-active species, which are critical to important natural and technological processes, ranging from the Marangoni propulsion of microorganisms to the active motion of bubbles and droplets in microfluidic devices.

2.1 Introduction

Surfactant-driven propulsion created by Marangoni flows are caused by an asymmetric distribution of surface-active contaminants (surfactants) at an interface such as the bubble surface ([2], [3], [4]). These interfacial concentration gradients are what creates Marangoni-driven flows in the surrounding liquid, generating motion. This chapter uses direct numerical simulations to enhance the understanding of the dynamics of Marangoni-induced propulsion of microbubbles in a highly-viscous outer-fluid.

For several decades, Marangoni flows in a viscous fluid have been investigated, theoretically and experimentally, for both its fluid mechanical interest and practical applications ([2], [3], [4], [24]). These studies have investigated the hydrodynamic influence of Marangoni flows created by surface-active substances and inhomogenous

temperature distributions on bubbles, droplets, and surface tension generated interfacial waves occurring at phase boundaries between liquid-gas and liquid-liquid phases. Characterizing the dynamics of Marangoni-induced propulsion in a viscous outer-fluid is critical to understand, predict, and ultimately finely tune microbubble cleaning processes ([22], [25]). Understanding how microbubbles interact with contaminants at a micro scale allows for a more efficient and directed cleaning effort. Characterizing these dynamics are also pertinent in regulating biomedical tasks such as targeted drug delivery using small particles ([11], [12], [13]) and surfactant assisted propulsion of microorganisms ([5], [6]).

The following section describes how simulations are used to identify, in microscopic detail, how gradients in surface tension induced by irregular surfactant coverage produce Marangoni flows on the surrounding viscous fluid. This is completed by simultaneously solving the convection-diffusion equation for surfactant transport and the full Navier-Stokes system. This model allowed for an exhaustive examination of the micro-scale mechanisms of surfactant transport on the bubble interface. It is also made possible to investigate the free-surface flows generated by the Marangoni stresses induced by surface tension gradient on a bubble interface. The system is considered highly viscous ($Re \ll 1$) due to the small bubble radius being the characteristic length-scale for the model resulting in a small Reynolds value.

The model system is described in Section 2.2 and introduces the equations governing the fluid mechanics of Marangoni flows. Section 2.3 first validates the simulation results against previous theoretical work for Marangoni flows in thin viscous films. Then, results from the simulations are used to explain in microscopic detail how surface tension gradients induced by uneven interfacial coverages produce spontaneous hydrodynamic flows on the surrounding bulk liquid. These resulting flows in bulk fluid lead to bubble motion. These results are then extended to the study of Marangoni propulsion of contaminated bubbles.

2.2 System Description and Governing Equations

Here, an accurate model (Sections 2.2.1 and 2.2.2) and high-fidelity simulations (Section 2.2.3) incorporating all of the relevant phenomena that influence the active motion of microbubbles are developed to help provide insight into the fundamental mechanisms of self-propulsion and probe variables that are not readily accessible in experiments.

2.2.1 The Fluid Mechanics of Marangoni Propulsion

As a model system, the self-propulsion of a bubble of small radius $\hat{R}$ surrounded by a viscous liquid of density $\hat{\rho}$ and viscosity μ is considered. The surface of the bubble is partially covered with an insoluble surfactant as sketched in Figure 2.1. This configuration is common, for example when a small contaminated bubble coalesces with a larger clean bubble resulting in a bubble with a small surfactant patch, as seen in Figure 2.2, or when a small bubble approaches a contaminated surface. The initially surfactant-laden region subtends a solid angle ω of contaminated spherical interface. This solid-angle ω of initial contaminated interface subtends a fraction ε

$$\varepsilon = \frac{\omega}{4\pi} * 100\% \tag{2.1}$$

representing the percentage of contaminated spherical interface based off the solid-angle of contamination (ω) normalized by the solid angle of the entire sphere (4π). Thus, a surfactant coverage $\varepsilon > 50\%$ describes a bubble with surfactant contaminating more than half the spherical interface in relation to the clean interface. Conversely, $\varepsilon < 50\%$ describes a comparatively smaller region of contamination where less than half of the spherical interface is contaminated in relation to the clean bubble interface. The surfactant-laden area has an initial concentration of surfactant $\hat{\gamma}_0$. The initial location of the surfactant front along the normalized arc-length s of the bubble is $s = \alpha$ as shown by Figure 2.1.

Due to asymmetric surfactant distribution, the bubble free-surface experiences differences in surface tension. These gradients generate flow in the outer-fluid causing bubble motion as shown in Figure 2.3.

Since the system is considered axisymmetric, it is described using a cylindrical coordinate system (z, r) as shown in Figure 2.1. The dimensional velocity components, where a hat (ˆ) specifies dimensional variables, in $\hat{z}$ and $\hat{r}$ directions are $\hat{u}$ and $\hat{v}$ respectively.

The system and results are described in dimensionless forms in the thesis. The system is cast dimensionless using capillary velocity $V = \hat{\sigma}_0/\mu$ as characteristic velocity scale, initial bubble radius $\hat{R}$ as characteristic length scale, and $\mu V/\hat{R}$ as the stress scale, where $\hat{\sigma}_0$ is the surface tension that corresponds to $\hat{\gamma}_0$. Accordingly, the characteristic time scale is $\tau = \hat{R}\mu/\hat{\sigma}_0$. The dimensionless concentration of surfactant γ is measured in units of initial dimensional concentration $\hat{\gamma}_0$, and the corresponding dimensionless surface tension σ is measured in units of the initial dimensional surface tension $\hat{\sigma}_0$. The relationship between the dimensional variables and dimensionless variables is given as:

$$r = \frac{\hat{r}}{\hat{R}}, \quad z = \frac{\hat{z}}{\hat{R}}, \quad \sigma = \frac{\hat{\sigma}}{\hat{\sigma}_0}, \quad \gamma = \frac{\hat{\gamma}}{\hat{\gamma}_0}, \tag{2.2}$$

$$t = \frac{\hat{\sigma}_0}{\hat{R}\mu}\hat{t}, \quad (u, v) = \frac{\mu}{\hat{\sigma}_0}(\hat{u}, \hat{v}), \quad p = \frac{\hat{R}}{\hat{\sigma}_0}\hat{p} \tag{2.3}$$

The evolution of the velocity field $\mathbf{v}$ and pressure p in the outer-liquid is governed by the axisymmetric dimensionless continuity equation,

$$\nabla \cdot \mathbf{v} = 0, \tag{2.4}$$

and the conservation of momentum,

$$Re\left(\frac{\partial \mathbf{v}}{\partial t} + \mathbf{v} \cdot \nabla \mathbf{v}\right) = \nabla \cdot \mathbf{T}, \tag{2.5}$$

where $\mathbf{T}$ is the viscous stress tensor given by

$$\mathbf{T} = -p\mathbf{I} + (\nabla \mathbf{v} + \nabla \mathbf{v}^T). \tag{2.6}$$
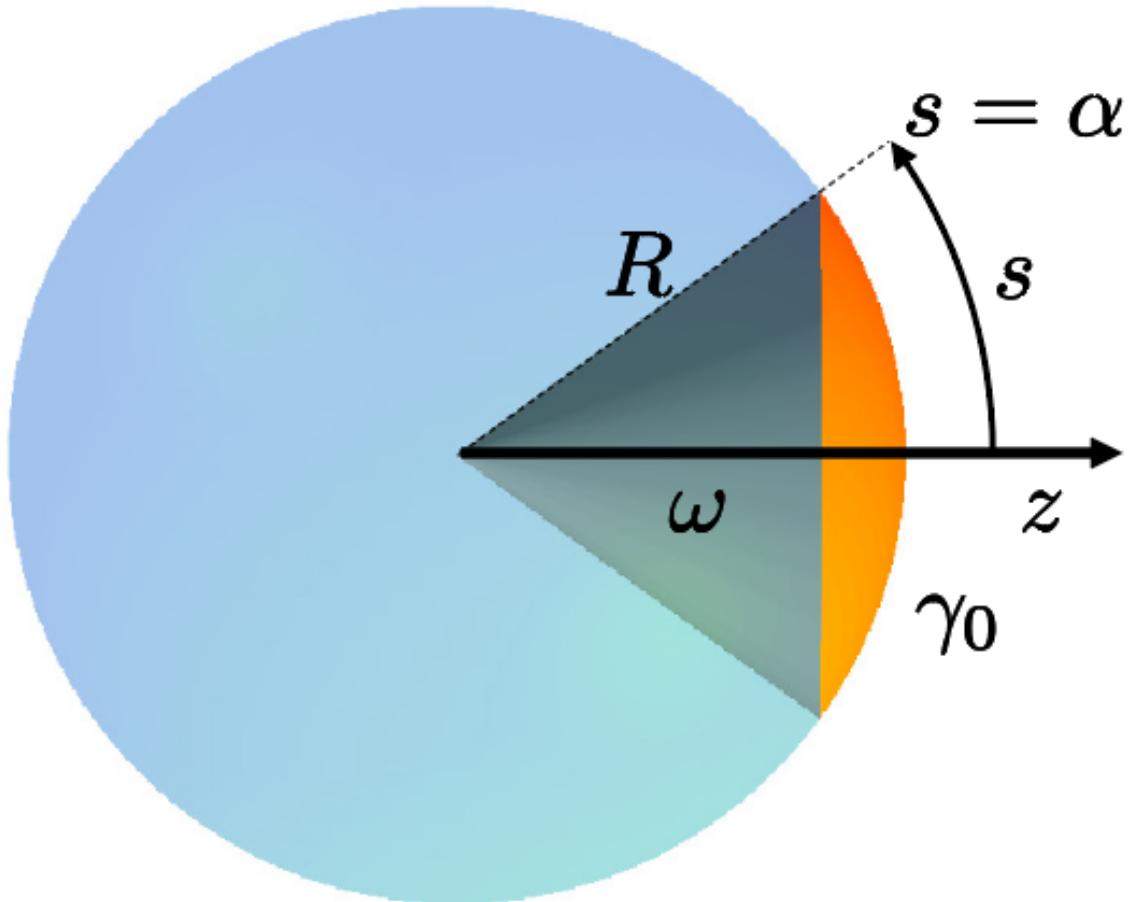
Fig. 2.1. **Schematic of active bubble with surfactant patch.** A bubble with a clean interface (blue) and a surfactant coated patch (orange). The radius of the bubble is R. The initial surfactant coverage extends across the bubble normalized arc-length s until $s = \alpha$ with the initial surfactant concentration being γ_0. The initial solid-angle of contaminated bubble interface is ω. The z-axis is shown by the horizontal black arrow.
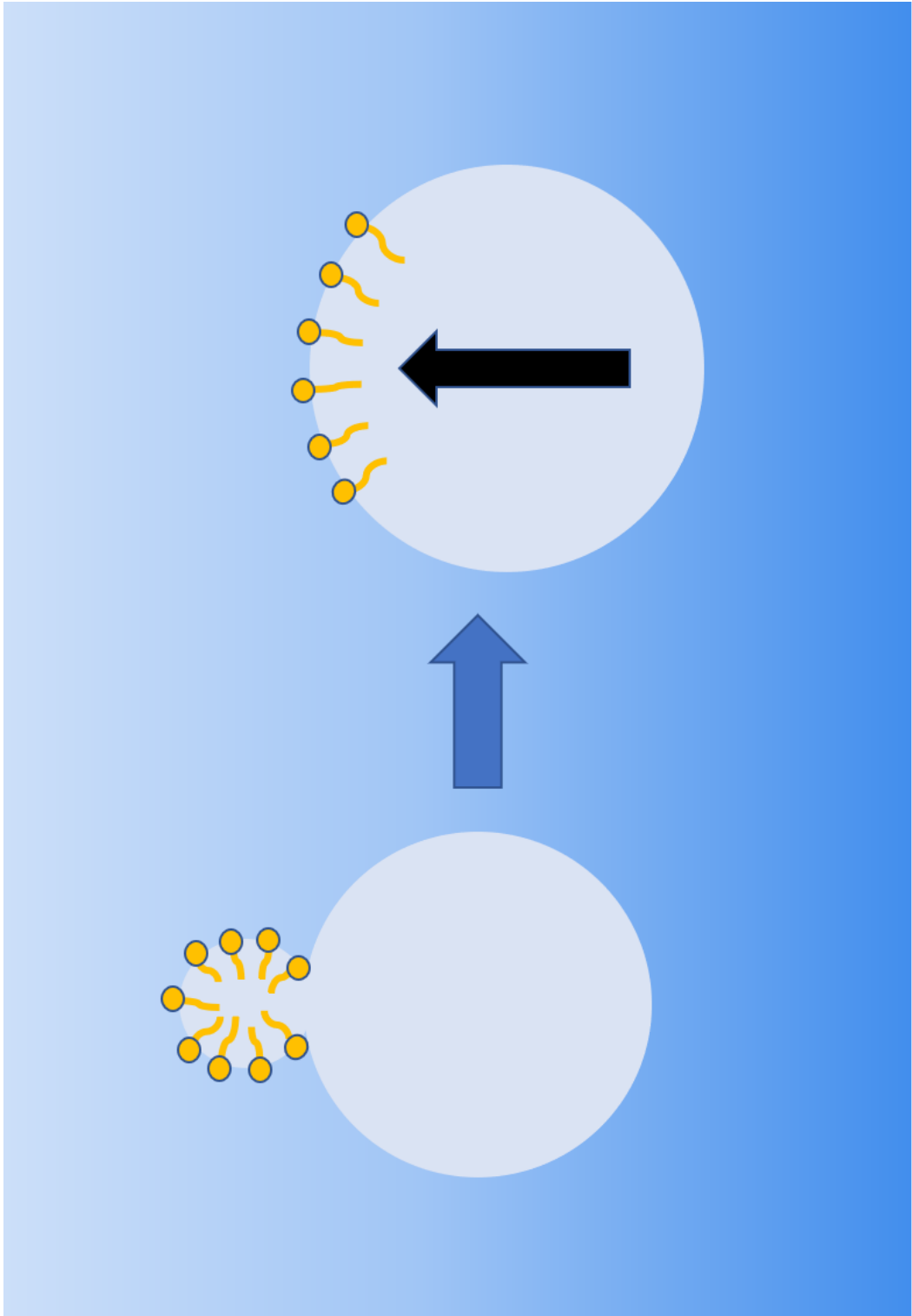
Fig. 2.2. **Sketch of a larger clean bubble coalescing with a small surfactant coated bubble.** This describes how bubble coalescence (occurring on the left) in a fluid can result in a bubble with a small contaminated patch (image on the right) creating an active bubble moving in the direction of the black arrow.
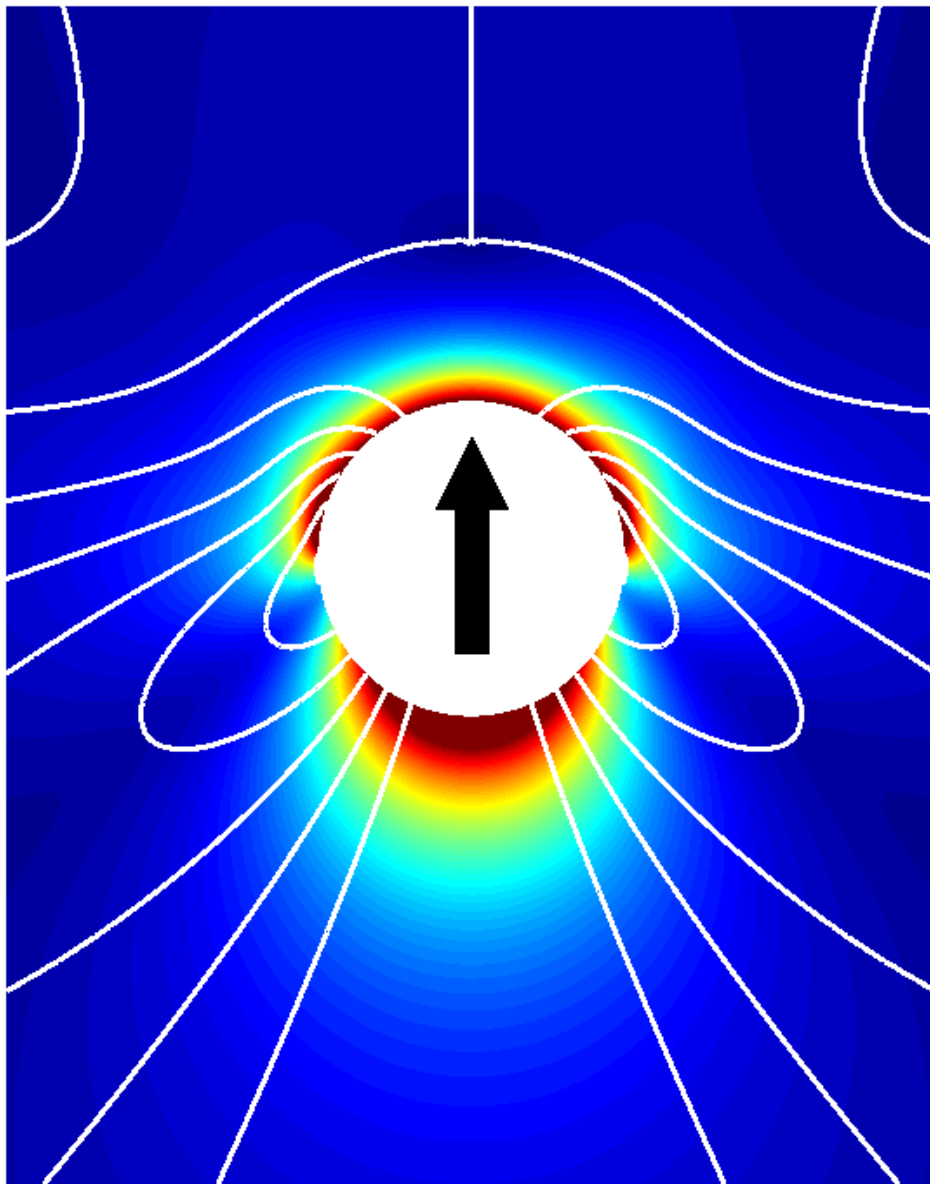
Fig. 2.3. **Cross sectional velocity field induced by active bubble motion.** Interfacial tension gradients (Marangoni stresses) produce hydrodynamic flows in the outer liquid through viscous momentum transfer, leading to bubble motion (black arrow). The initial coverage is $\varepsilon = 9.6\%$, Marangoni number is $Ma = 2$, $Pe = 140$, and the Reynolds number is $Re = 10^{-4}$ with the cross sectional velocity field shown at $t \approx 6$.

Since the choice of characteristic length scale and characteristic velocity scale are $\hat{R}$ and $\hat{\sigma}_0/\mu$ respectively, the Reynolds number in Equation (2.5) is

$$Re = \frac{\rho\hat{\sigma}_0\hat{R}}{\mu^2}, \tag{2.7}$$

which measures the relative significance of the inertial and viscous forces. Because of the small size of the bubble, this thesis focuses on the limit of negligible inertia $Re \ll 1$. This is due to the small size of the bubble radius $\hat{R} \ll 1$.

At the bubble interface, the traction boundary condition is applied [26]

$$2\mathcal{H}\sigma\mathbf{n} + \nabla_s\sigma = \mathbf{n} \cdot \mathbf{T}, \tag{2.8}$$

where $\mathbf{n}$ is the unit vector normal to the interface and $2\mathcal{H}$ is the mean interface curvature $2\mathcal{H} = -\nabla_s \cdot \mathbf{n}$. The traction boundary condition includes both normal capillary stresses $2\mathcal{H}\sigma\mathbf{n}$ and tangential (Marangoni) stresses $\nabla_s\sigma$ induced by surface tension gradient due to the presence of surfactant.

At the bubble interface the kinematic boundary condition is also imposed assuring that there is no mass transfer across the gas-liquid interface

$$\mathbf{n} \cdot (\mathbf{v} - \mathbf{v}_s) = 0, \tag{2.9}$$

where $\mathbf{v}_s$ is the velocity of the free surface. At the solid boundary of the tube, the radial limit of the model, $r = R_t$, where $R_t = 20$, the no-slip and no-penetration boundary conditions are applied:

$$u(z, R_t) = 0, \quad v(z, R_t) = 0. \tag{2.10}$$

Since the system is considered axisymmetric where the symmetric boundary condition is applied until the end of the tube at $z = \pm 20$:

$$v(z, 0) = 0, \quad \frac{dv}{dr}(z, 0) = 0. \tag{2.11}$$

The simulations start with an outer-fluid considered undisturbed. Thus, at $t = 0$, the initial conditions are:

$$u(z, r) = 0, \quad v(z, r) = 0, \quad R(z, r) \pm \sqrt{r^2 + z^2} = 1. \tag{2.12}$$

2.2.2 Surfactant Transport and Marangoni Stress

The transport of surfactant on the surface of the bubble is described by the full convection-diffusion equation ([27], [28], [29]),

$$(\frac{\partial \gamma}{\partial t})_s + \gamma(\mathbf{v}_s \cdot \mathbf{n})(\nabla_s \cdot \mathbf{n}) + \nabla_s \cdot (\gamma \mathbf{v}_s \cdot \mathbf{t})\mathbf{t} - Pe^{-1}\nabla_s^2 \gamma = 0, \qquad (2.13)$$

which is solved simultaneously with the Navier-Stokes system of equations, where $\mathbf{t}$ is the unit vector tangent to the interface and $\nabla_s = (\mathbf{I} - \mathbf{nn}) \cdot \nabla$ is the surface gradient operator. The second term of Equation (2.13) describes changes in surfactant concentration due to changes in local surface area. The third term describes changes in surfactant concentration due to convection, and the fourth term describes changes in surfactant concentration due to diffusion. In the diffusion term, the Peclet number is given as:

$$Pe = (\hat{\sigma}_0 \hat{R}/\mu \mathcal{D}), \qquad (2.14)$$

where $\mathcal{D}$ is the surfactant diffusion coefficient. For the typical values of the physico-chemical parameters, the diffusive timescale is far larger than the visco-capillary timescale, even when the size of the bubble can be as small as tens of microns. In the simulations presented in this chapter, the order of magnitude for the Peclet number is set $Pe = O(100)$ calculated by using typical $\mathcal{D} = O(10^{-9})$ and bubble radius $\hat{R} = O(10^{-5})$.

The surfactant transport is strongly coupled with the free-surface hydrodynamics since both terms on the left side of Equation (2.8) depend on the surfactant concentration distribution $\gamma(s, t)$ through surface tension $\sigma(s, t)$. Here, a linear equation of state is used to represent the relationship between surfactant concentration γ and surface tension σ ([30], [31], [32]):

$$\sigma = 1 - Ma(\gamma - 1), \qquad (2.15)$$

where Ma is the Marangoni number, which characterizes the surfactant strength. Larger Marangoni numbers create greater surface tension gradients and consequently higher Marangoni stress. The Marangoni number is given as:

$$Ma = \frac{d\hat{\sigma}}{d\hat{\gamma}} \frac{\hat{\gamma}_0}{\hat{\sigma}_0}. \tag{2.16}$$

As stated in the previous section, simulations start with a bubble having an initial dimensionless radius of $R = 1$. The initial deposition of the surfactant on the bubble interface extended across the normalized arc-length of the bubble s until $s = \alpha$, with $\alpha = 0.2$, as seen in Figure 2.1.

$$\gamma(s, t = 0) = \begin{cases} 1 & s \leq \alpha \\ 0 & s > \alpha \end{cases} \tag{2.17}$$

2.2.3 Direct Numerical Simulation

This section presents the numerical methods used to solve the theoretical model stated in the previous two sections. The non-linear system of partial differential equations (Equations (2.4), (2.5), and (2.13)) describing the free-surface dynamics of Marangoni flows induced by surfactant is solved based on a finite element algorithm. The algorithm used in this Chapter is also applied to the simulations in Chapter 3.

The complexity of the numerical algorithm is considerable since the problem of surfactant-induced Marangoni flows is highly nonlinear and strongly coupled. The transport of surfactant is coupled with the bulk liquid flow. Furthermore, the gradient of the surfactant concentration over the bubble surface determines the Marangoni stress, which drives the Marangoni flow. This flow determines the surfactant concentration distribution on the bubble interface. This leads to a strongly coupled free-surface problem.

The full set of equations including the Navier-Stokes, continuity, kinematic, and convection-diffusion equation along with their boundary conditions have to be solved in a domain (Ω) that is unknown *a priori*. For that purpose, a numerical scheme based on the Finite Element Method (FEM) [33], combined with a mapped mesh technique

[34], which is implemented by the commercial code Comsol Multiphysics [35] is used. The Comsol algorithm was extended to include the surfactant convection-diffusion equation (Equation (2.13)) discussed in previous sections and is used throughout the thesis.

In our numerical procedure, the elements of the mesh and the associated points of the grid have a fixed configuration in a reference domain Ω_0. Each point $(\mathbf{x}_0 = (r_0, z_0))$ in the reference domain (Ω_0) is mapped to each point $(\mathbf{x} = (r, z))$ in the physical domain of the problem, Ω, by means of a one-to-one mapping. Therefore, there exists an inverse mapping, that in our case obeys the equation set

$$\begin{cases} \dfrac{\partial^2 r_0}{\partial r^2} + \dfrac{\partial^2 r_0}{\partial z^2} = 0, \\ \dfrac{\partial^2 z_0}{\partial r^2} + \dfrac{\partial^2 z_0}{\partial z^2} = 0, \end{cases} \tag{2.18}$$

which is usually know as the Winslow's Smoothing Method [36]. The boundary conditions for Equation (2.18) are (a) $r_0 = R_t$ with $R_t = 20$ and $\partial z_0/\partial r = 0$ at the surface of the tube, (b) $r_0 = 0$ and $\partial z_0/\partial r = 0$ at symmetry axis, (c) $z_0 = \pm R_t$ and $\partial r_0/\partial z = 0$ at both ends of the tube, and (d) $\mathbf{n} \cdot \nabla \mathbf{x}_0 = \lambda \mathbf{n}$ at the free surface, λ being an additional variable. The size of the axi-symmetric domain is sufficiently large not to affect the results extending 20 radius away in each direction.

Our numerical scheme implements the classical Galerkin/FEM weighted residuals formulation to solve simultaneously the Navier-Stokes, continuity, kinematic, conservation of surfactant, and Equation (2.18) along with their boundary conditions. Lagrange elements were employed with piecewise-quadratic, continuous approximations for all variables except pressure, using a piecewise-linear, continuous approximation. The mesh used in this chapter consists of 19,600 triangular elements; 314 of them are located along the free surface. This spatial discretization procedure results in a system of non-linear algebraic equations that was solved by Newton iterations. The linear solver for this iteration loop was MUMPS [37]. The number of degrees of freedom solved for is 170300 in the investigation completed in this chapter. The number of triangular elements and degrees of freedom solved for is dependent on the geometry

of the system which is altered in Chapter 3 when investigating the influence of the tubular boundary.

2.3 Spreading of a Surfactant on a Plane Gas-liquid Interface

In this section, simulations of the free-surface dynamics of viscous Marangoni flows is illustrated for the case of thin films, and compared against previous results from the literature. This is completed by benchmarking theoretical predictions from Jensen and Grotberg [1] against computations completed by the model described in Section 2.2 with the geometry adapted spreading of a circular surfactant patch on a thin film. The modified model investigates a spreading surfactant monolayer on a flat air-liquid interface under viscous conditions. Results show that for thin viscous films, the theory agrees with the simulations.

The system for the validation is based off cylindrical coordinates of (r, z) with the gas-liquid interface height h being a function of radial distance r, and time t. The characteristic length in the axial direction is the interface thickness. Jensen and Grotberg's theoretical equation, that takes into account the balance of Marangoni and viscous stresses, can anticipate the location of the circular surfactant front r_S as a function of the initial radius of the surfactant patch $\tilde{R}_P$ (made dimensionless with the thickness of the fluid layer), Marangoni number Ma, and time t in the lubrication limit [1]. This scaling theory from Jensen and Grotberg [1] was created using the lubrication approximation with the extra assumptions of no capillary or gravitational forces, and a thin ($\tilde{R}_P \gg h$) and viscous ($Re \ll 1$) liquid film follows the similarity solution

$$h = \left(\frac{r}{(16\tilde{R}_P{}^2 Ma)^{1/4} t^{1/4}} \right)^2 \tag{2.19}$$

at later times.

A qualitative scaling discussion is presented below in order to justify the results. The Marangoni stress $\nabla_s \sigma$ driving the Marangoni flow, is approximated as

$$\nabla_s \sigma \approx d\sigma/dr \tag{2.20}$$

This is because of the small curvature of the liquid interface in the lubrication approximation. A linear equation of state, $\sigma = 1 - Ma(\gamma - 1)$ (Equation (2.15)), relates the local surfactant concentration γ to the surface tension σ. The location on the radius of the surfactant patch is r_S and the location on the radius of the liquid wave peak (maximum height) is r_L. Consequently, the Marangoni stress can be written as

$$\nabla_s \sigma \approx -Ma \, d\gamma/dr \tag{2.21}$$

where the concentration of surfactant scales as $\gamma \sim M/r_s^2 \sim \pi \tilde{R}_P^2 r_s^{-2}$ when following the investigation by Jensen [38] and defining the total mass of surfactant as M, producing

$$\nabla_s \sigma \sim Ma \pi \tilde{R}_P^2 r_s^{-3}. \tag{2.22}$$

The Marangoni stress is balanced by the viscous stress approximated as dV/dz over the viscous interface, where the radial velocity scale V is given by the surfactant front average velocity $V \sim r_s/t$. By reconstructing the equations, viscous stresses can be estimated by

$$dV/dz \sim r_s/t. \tag{2.23}$$

Finally, using the stress balance over the radius interface

$$d\sigma/dr \sim dV/dz \tag{2.24}$$

yields the scaling for the radius of the surfactant front

$$r_s \sim (\pi \tilde{R}_P^2 Mat)^{1/4}. \tag{2.25}$$

The viscous and Marangoni stress (Equation (2.24)) balances were combined by Jensen and Grotberg [1] with the added assumption that the leading edge speed of the surfactant-laden interface r_S equals the speed of the wave generated at the leading edge r_L. The prefactor to the (2.25), derived using similarity analysis, was found to be

$$r_s = (16 Ma \tilde{R}_P^2 t)^{1/4}. \tag{2.26}$$

Figure 2.4 displays how the simulated results for the radius of the surfactant patch r_S and the radius of the liquid wave peak r_L closely follows the scaling described in Equation 2.26 for viscous interfaces, primarily at later times $t > 10^3$.

In this section results from the simulation were shown to follow the scaling law predictions discussed in literature related to viscous Marangoni flows. The strength of the simulated results were shown by benchmarking this modified simulation with Jensen and Grotberg's theoretical scaling law.
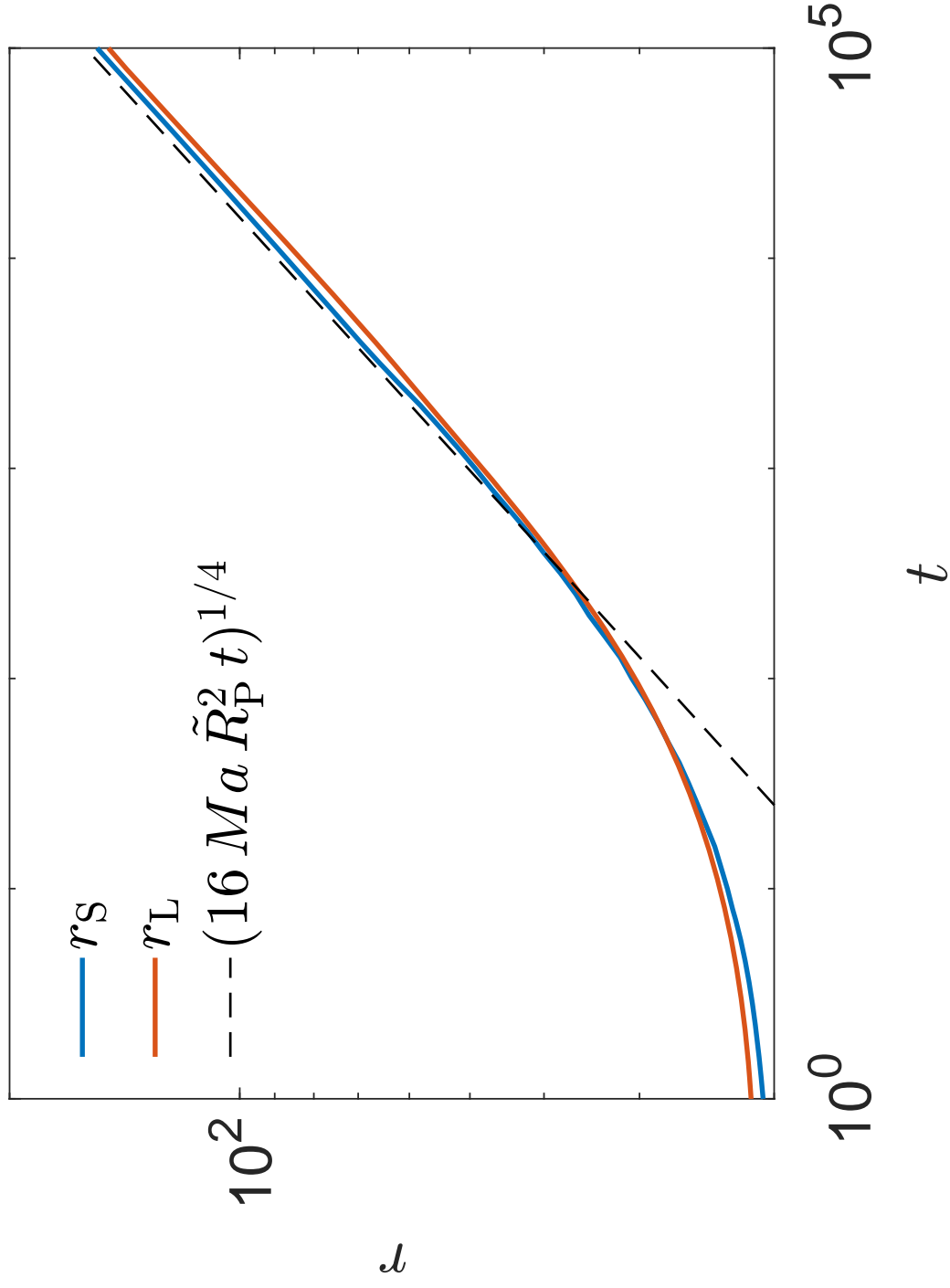
Fig. 2.4. **Logarithmic plot comparing theoretical scaling solutions with simulated results for surfactant spreading on a viscous interface.** This plot shows the radial location r of the surfactant patch r_S and the liquid wave peak r_L over time t compared to the scaling described in Equation 2.26. This is for a liquid of $Re = 0.01$ and a surfactant of $Ma = 1$ and $Pe = 10^{-4}$.

2.4 Self-propulsion of Contaminated Microbubbles: Interfacial Mechanisms and Flow Regimes

2.4.1 Active Motion

This subsection discusses the overall motion of a small contaminated bubble during Marangoni-induced propulsion. This is done by investigating the displacement and velocity of the bubble interface associated with the propulsion and deformation of the bubble for the duration of the active motion.

As illustrated in Figure 2.3, surface-tension gradients induced by the presence of surfactant produce flow in the outer fluid driving the motion of the bubble. To begin discussing this motion, a small bubble is considered with approximately 1/10 of its surface ($\varepsilon = 9.6\%$) uniformly covered with a moderate surfactant ($Ma = 2$) leading to self-propulsion in the axial direction. This thesis focuses on the limit of negligible inertia with $Re = 10^{-4} \ll 1$.

This transient motion is examined by following the speed v_M of the bubble center of mass over several decades in time in Figure 2.5. Initially, the surface-tension gradients are strong, and the speed of the bubble grows rapidly. Starting from rest, the speed rapidly increases to $v_M \approx O(10^{-1})$ at early times and then remains approximately constant. The v_M speed increases moderately at $t \approx 0.3$, and then decays with time as the surface-tension gradients vanish.

The corresponding displacement d of the bubble center of mass z_M is shown in Figure 2.6. Bubble displacement becomes detectable at early times $t \approx 10^{-2}$ and increases steadily for approximately three decades in time. When the bubble returns to rest at $t \approx 50$, the total displacement is of the order of the bubble size.

It is also observed that because of the asymmetric surfactant distribution the front F and back B of the bubble, shown in Figure 2.7, move at different speeds causing the interface to deform. The leading edge of the bubble has a larger initial velocity v_F (solid red line) shown by Figure 2.8. At time $t \approx 10^{-2}$ the leading edge of the bubble begins to slow down and the back end velocity v_B (dashed red line) slightly

increases at $t \approx 1$. Following $t \approx 1$, the back end velocity v_B began decreasing to follow the same slope as v_F at $t \approx 5$ where both ends shared identical speeds until the the end of the bubble movement. In this case the bubble front moves comparatively faster at early times resulting in the bubble elongating in the direction of the motion. Figure 2.9 shows the displacement of the front d_F and back d_B ends of the bubble with elongation becoming noticeable at $t \approx 10^{-2}$ with the front end displacement d_F (solid black line) becoming larger than the back end displacement d_B (dashed black line) until $t \approx 5$. After $t \approx 5$ the bubble regains its circular shape and the paths that d_F and d_B follow become nearly identical for the remainder of the bubble motion.

This elongation is visualized in Figures 2.10 and 2.11 where the initial shape of the bubble (dashed black line) is compared to the bubble shape at the time of maximum interfacial deformation $t \approx 0.6$. Due to the elongation, the bubble attains a flattening $f = 1 - (b/a)^2 \approx 0.45$ at $t \approx 0.6$ as shown in Figure 2.12. Here, a is the maximum bubble size in the axial direction and b is the maximum size in the radial direction. The velocity magnitude field shown in Figure 2.13 of the bubble at $t \approx 1.6$ depicts the movement of the back end in the direction of the elongated front end.

The results in this section explained the overall movement of the active bubble interface for the duration of the active swimming. Here, the deformation, displacement, and speed of the bubble interface movement along the axis of propulsion (z-axis) was explored in depth.

2.4.2 Interfacial Mechanisms

In this subsection the mechanisms associated with the Marangoni-induced propulsion on the bubble interface are investigated. The interfacial properties inspected include the tangential velocity, normal velocity, and the surfactant concentration across the interface over the duration of this bubble active movement.

Figure 2.14 shows the variation of the interfacial concentration of surfactant γ as a function of the normalized arc-length s along the surface of the bubble (see Figure
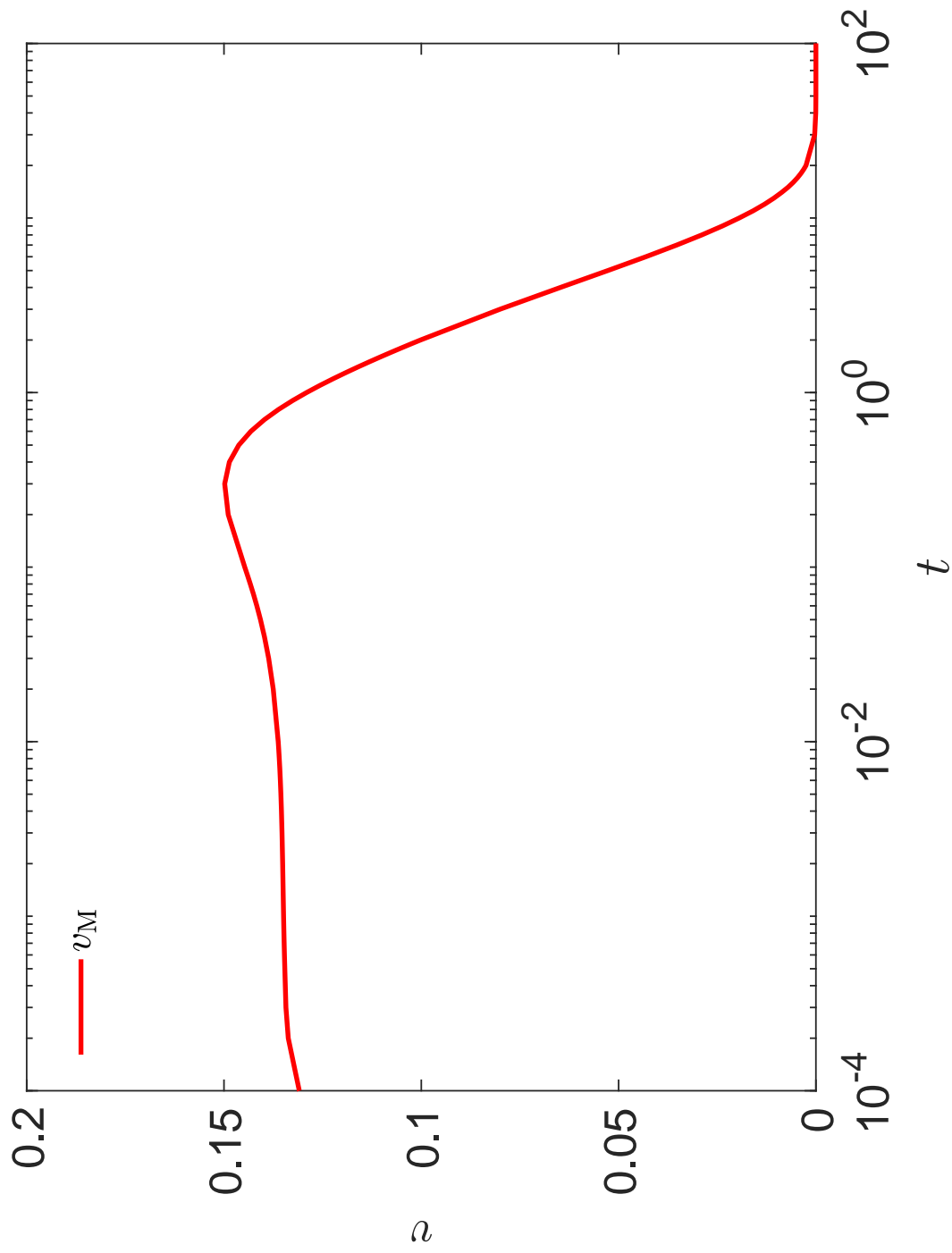
Fig. 2.5. **Temporal evolution of the center of mass velocity.** Velocity v of the center of mass v_M over time t during self-propulsion of a small contaminated bubble with $\varepsilon = 9.6\%$, $Ma = 2$, $Pe = 140$, and $Re = 10^{-4}$.
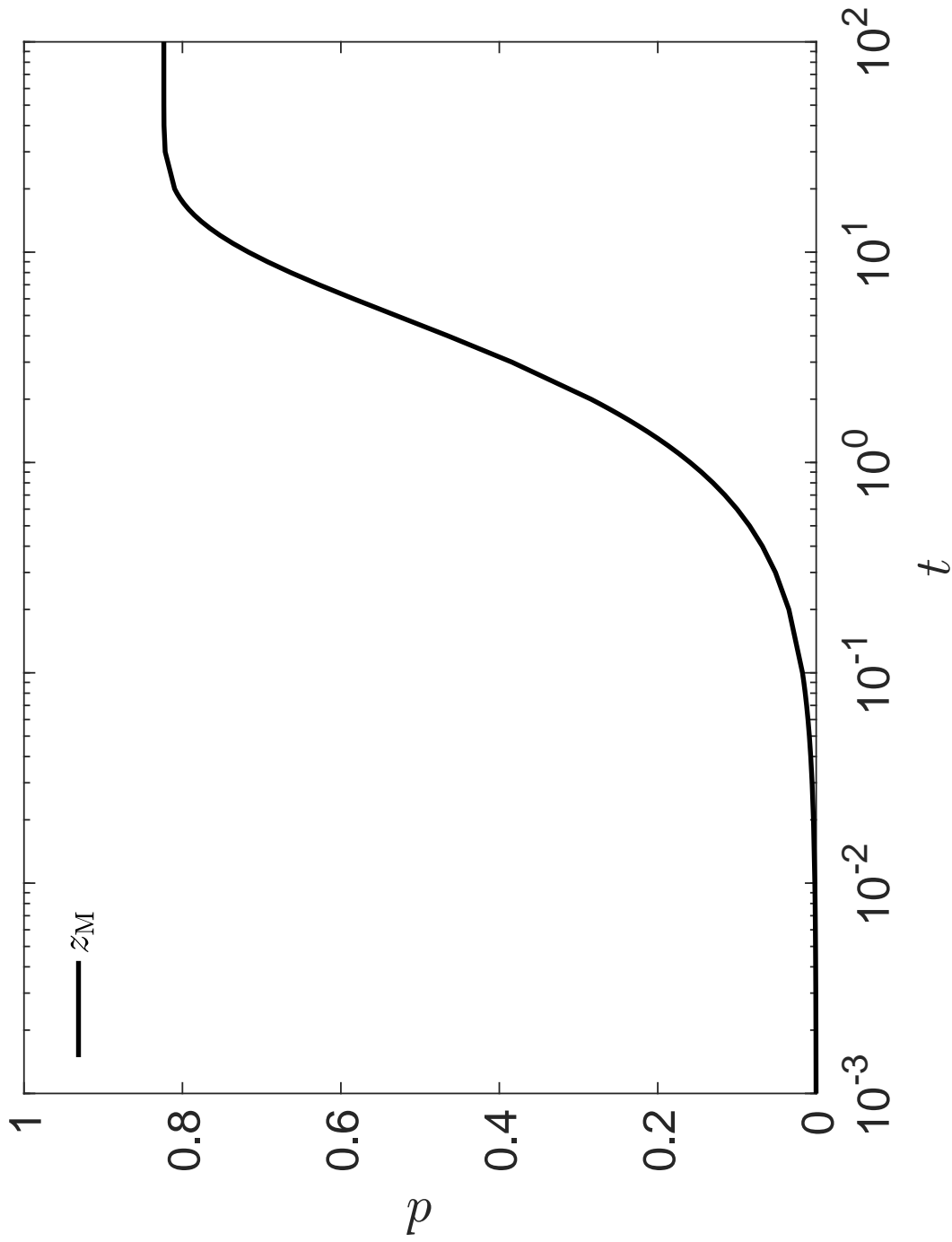
Fig. 2.6. **Temporal evolution of the displacement of the active bubble's center of mass.** Plot showing the displacement d of the bubble center of mass z_M over time t during self-propulsion of a small contaminated bubble with $\varepsilon = 9.6\%$, $Ma = 2$, $Pe = 140$, and $Re = 10^{-4}$.
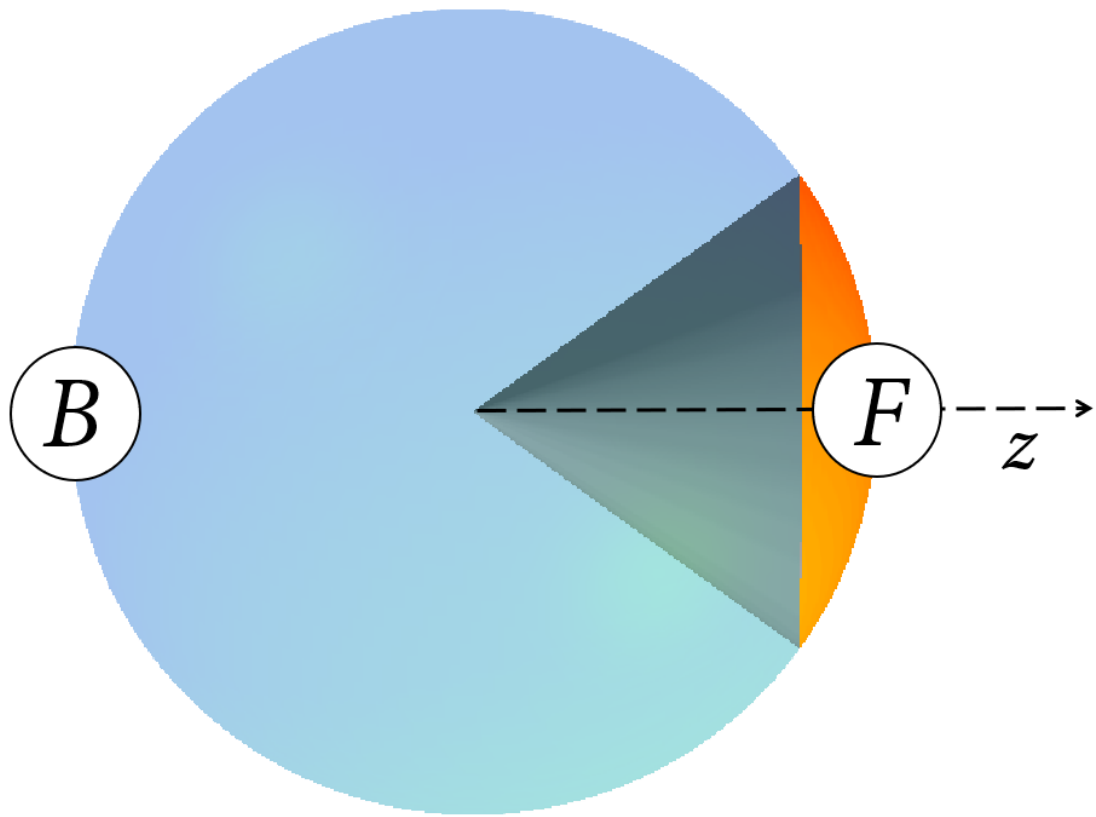
Fig. 2.7. **Sketch displaying directional nomenclature for the active bubble.** The plot shows the clean (blue) back end B and contaminated (yellow) $\varepsilon = 9.6\%$ front end F of the bubble on the positive side of the z-axis.
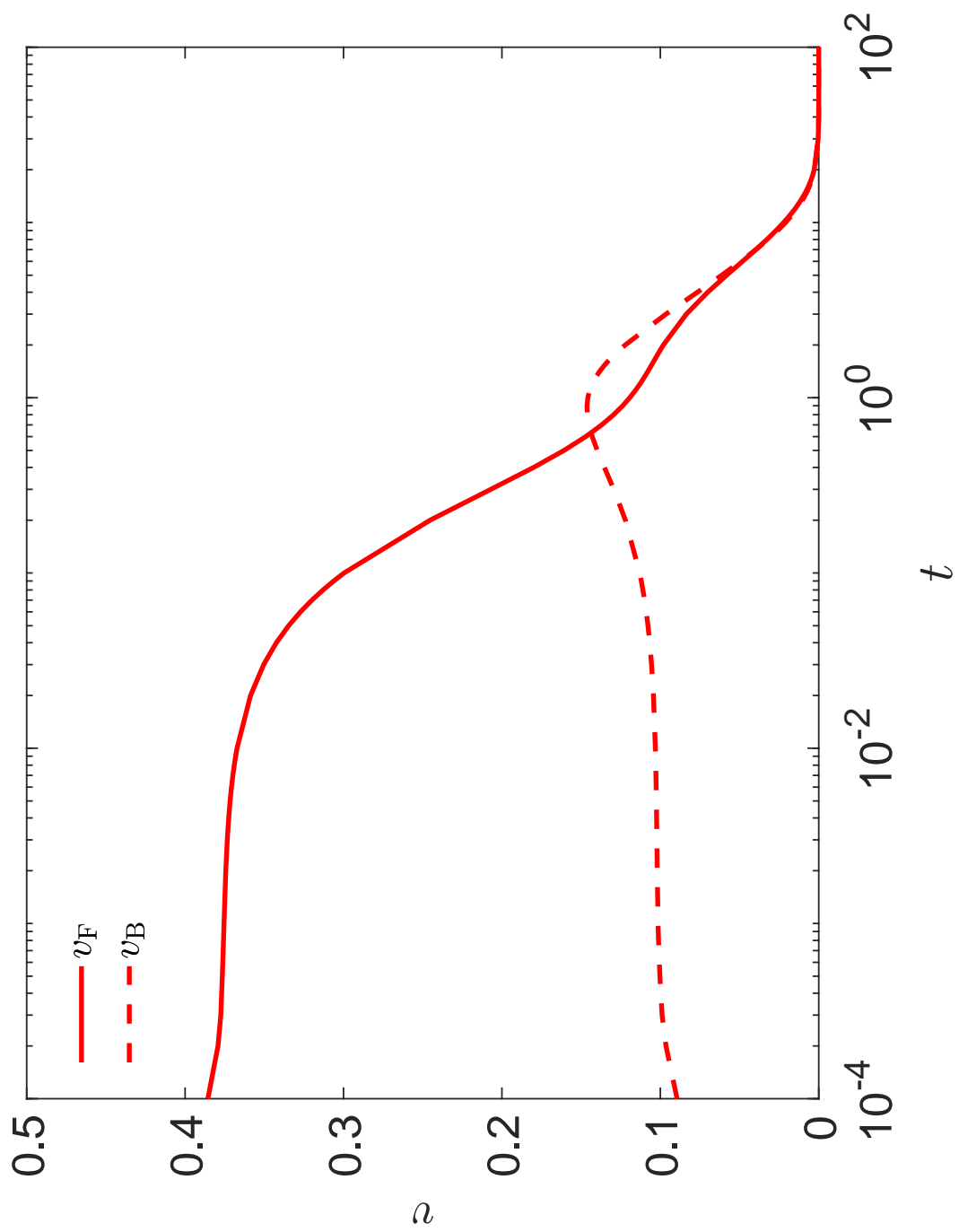
Fig. 2.8. **Temporal evolution of the active bubble front and back end velocities.** This figure shows the velocity v of the bubble front v_F (solid red line) and back v_B (dashed red line) end over time t during self-propulsion of a small contaminated bubble with $\varepsilon = 9.6\%$, $Ma = 2$, $Pe = 140$, and $Re = 10^{-4}$.
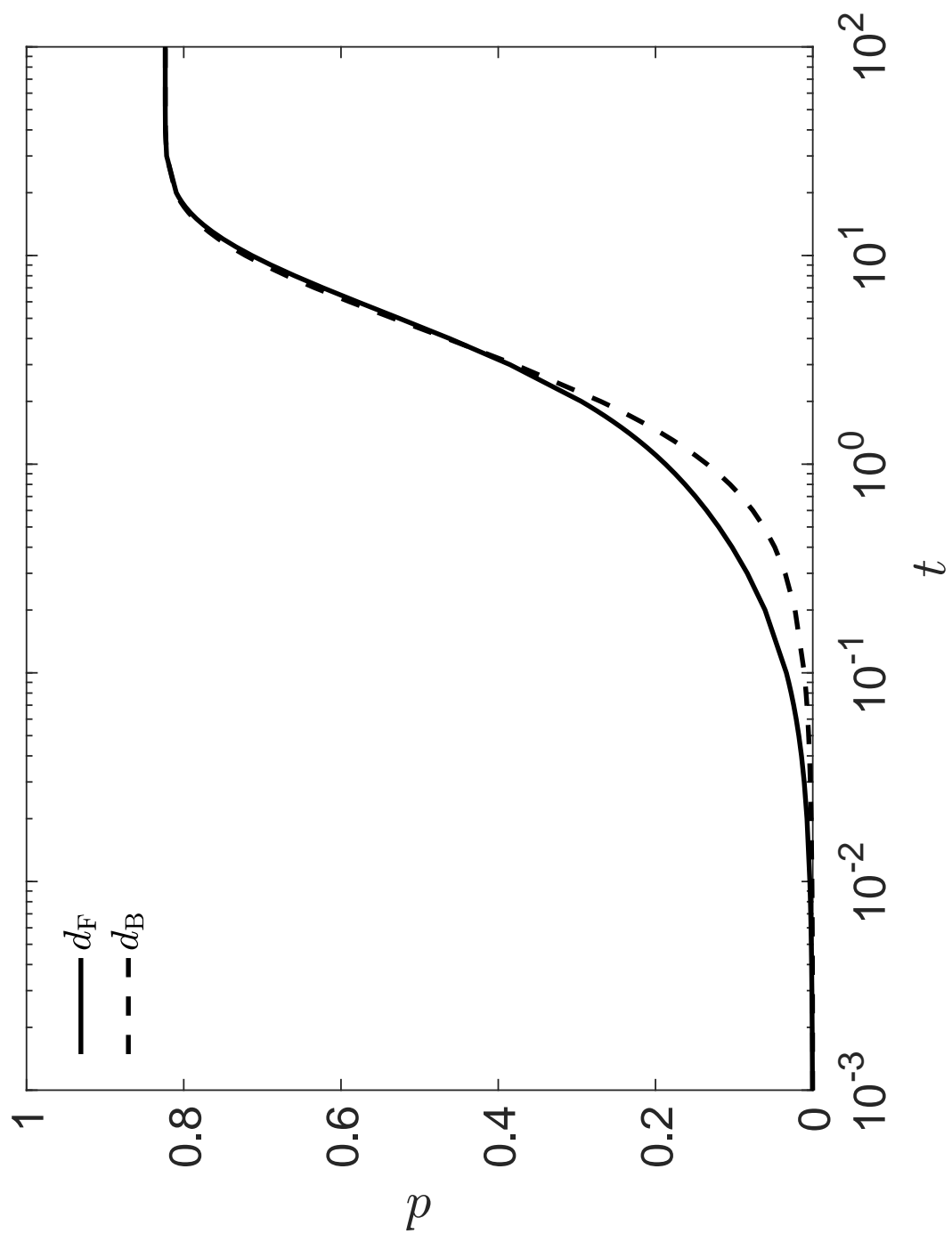
Fig. 2.9. **Temporal evolution of the active bubble front and back end displacements.** This figure shows the displacement d of the bubble front d_F (solid black line) and back d_B (dashed black line) end over time t of the case discussed with $\varepsilon = 9.6\%$, $Ma = 2$, $Pe = 140$, and $Re = 10^{-4}$.
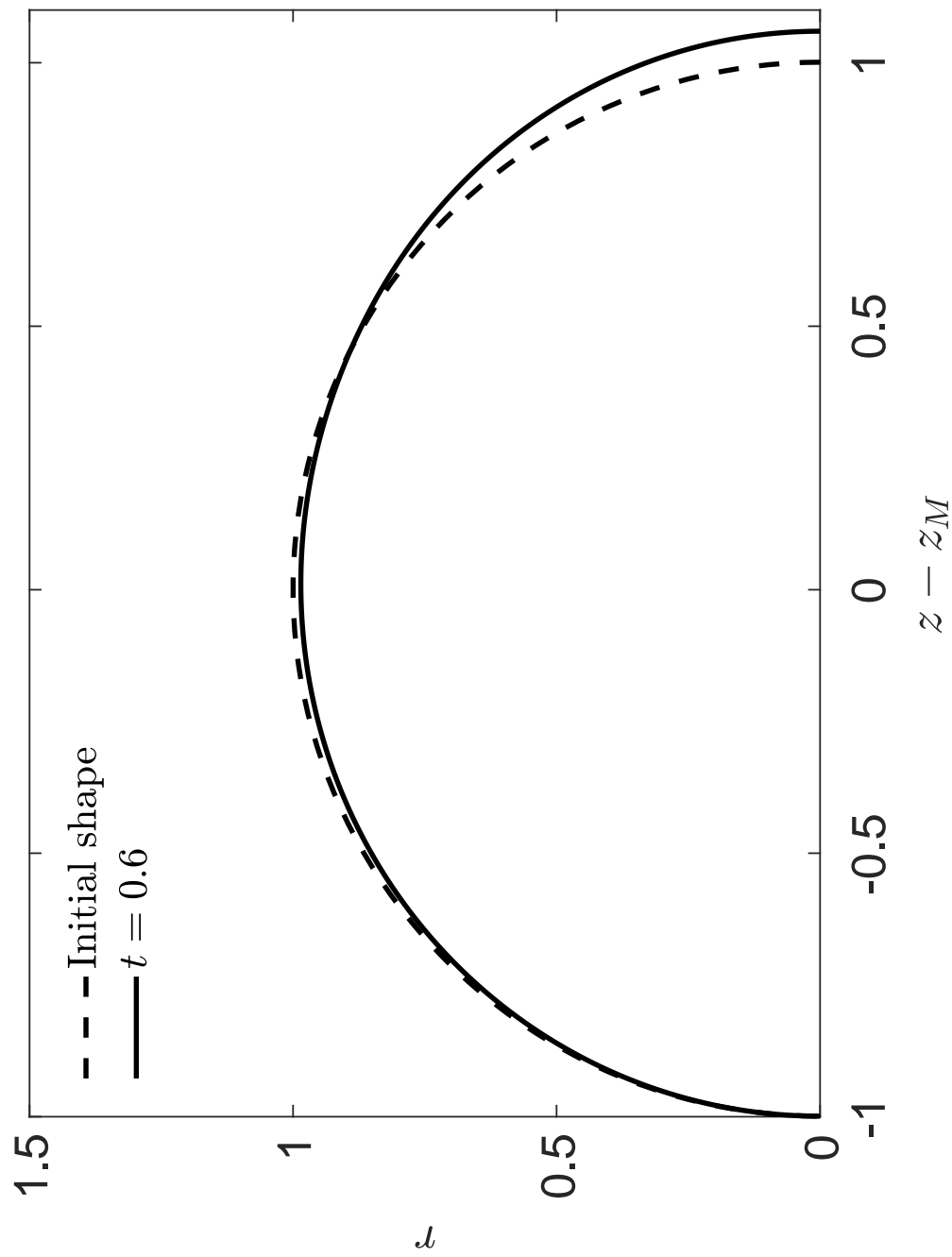
Fig. 2.10. **Maximum deformation interface shape of active bubble.** Comparing the maximum deformed interface shape (solid black line) against the initial bubble interface shape (dashed black line) during self-propulsion of a small contaminated bubble with $\varepsilon = 9.6\%$, $Ma = 2$, $Pe = 140$, and $Re = 10^{-4}$.
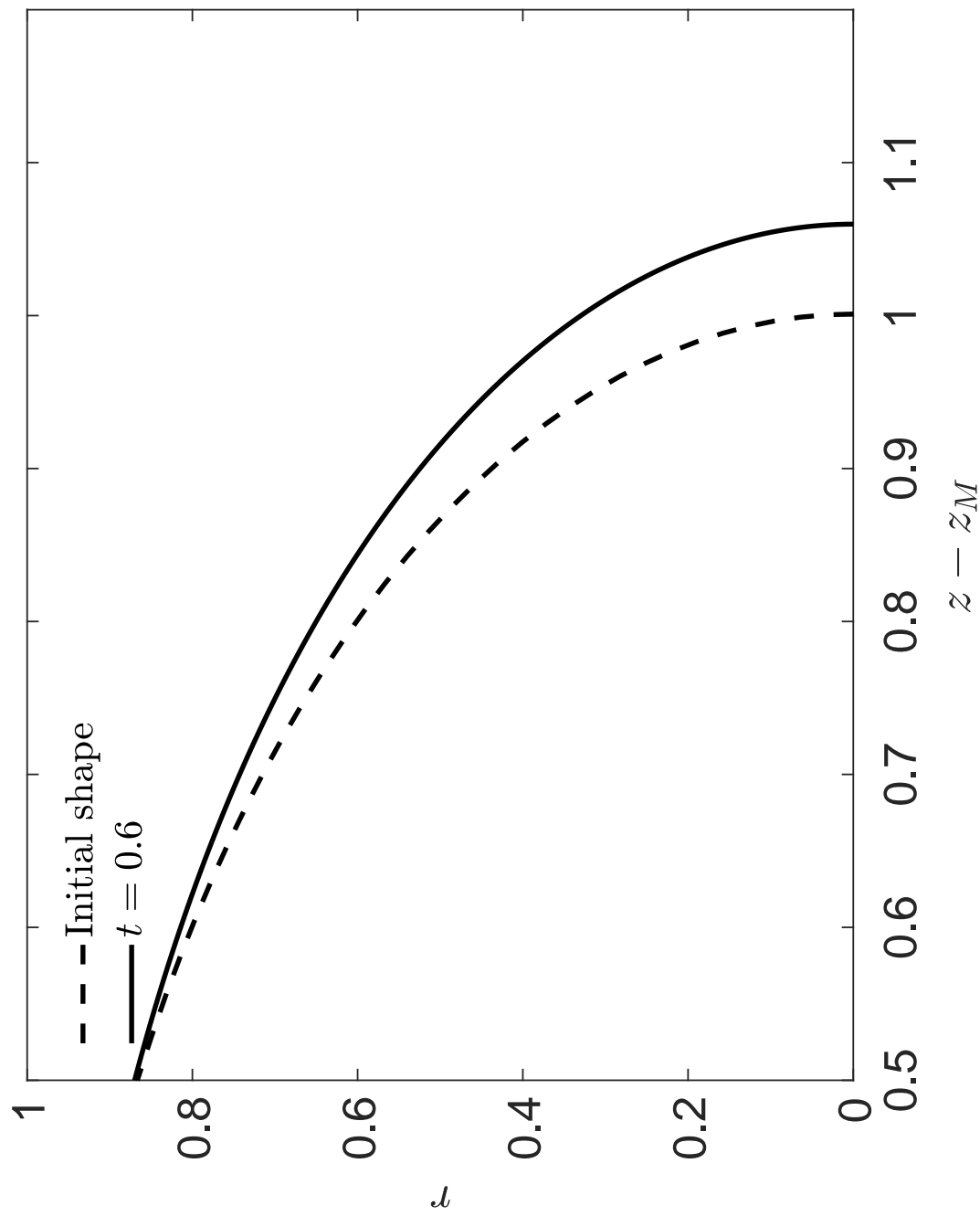
Fig. 2.11. **Focused maximum deformation interface shape of active bubble.** Comparing the maximum deformed interface shape (solid black line) against the initial bubble interface shape (dashed black line) during self-propulsion of a small contaminated bubble with $\varepsilon = 9.6\%$, $Ma = 2$, $Pe = 140$, and $Re = 10^{-4}$.
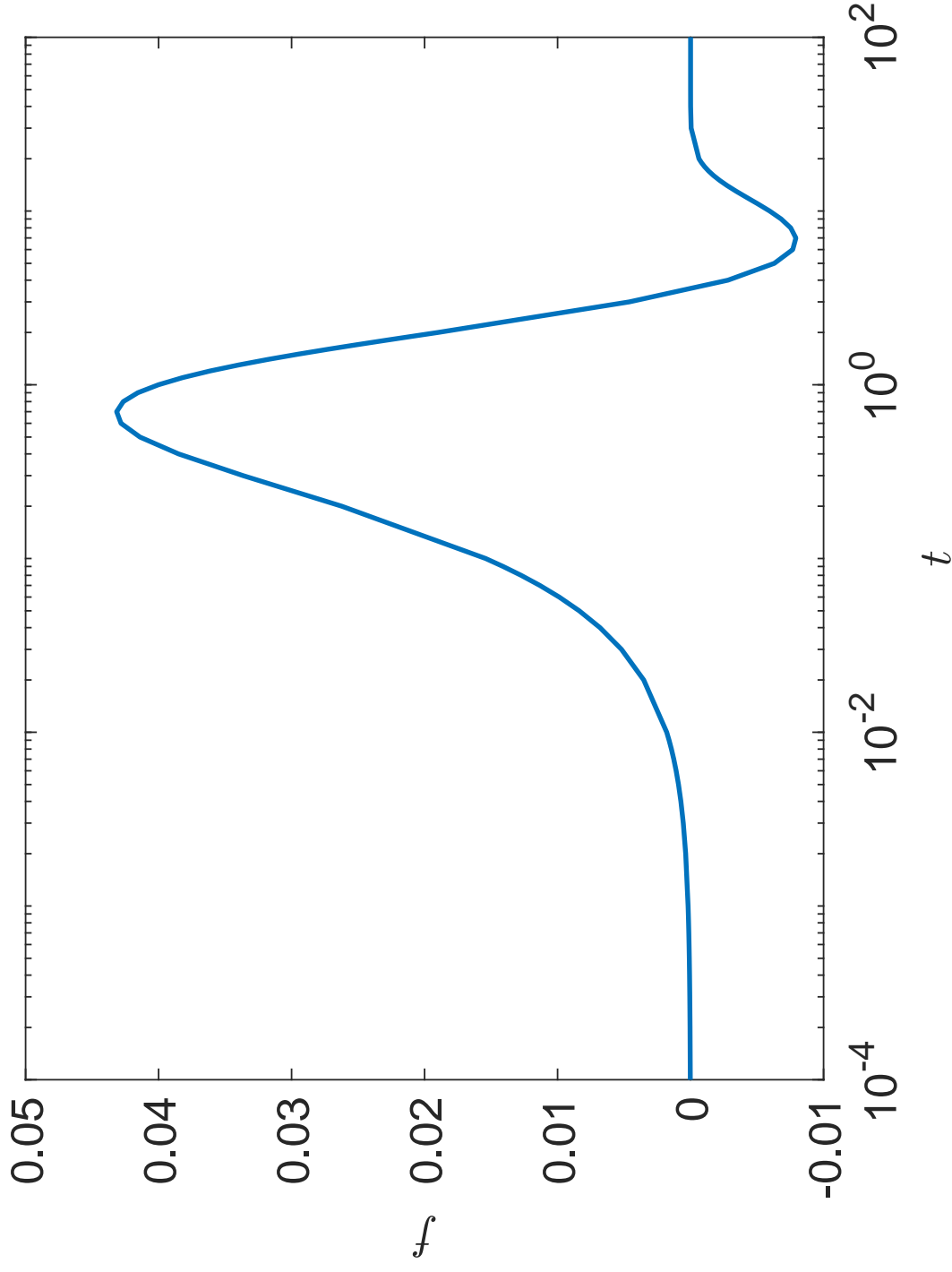
Fig. 2.12. **Temporal evolution of the bubble flattening.** Plot showing the flattening f over time t during self-propulsion of a small contaminated bubble with $\varepsilon = 9.6\%$, $Ma = 2$, $Pe = 140$, and $Re = 10^{-4}$. Flattening is described as $f = 1 - (b/a)^2$, where a is the maximum bubble size in the axial direction and b is the maximum size in the radial direction.
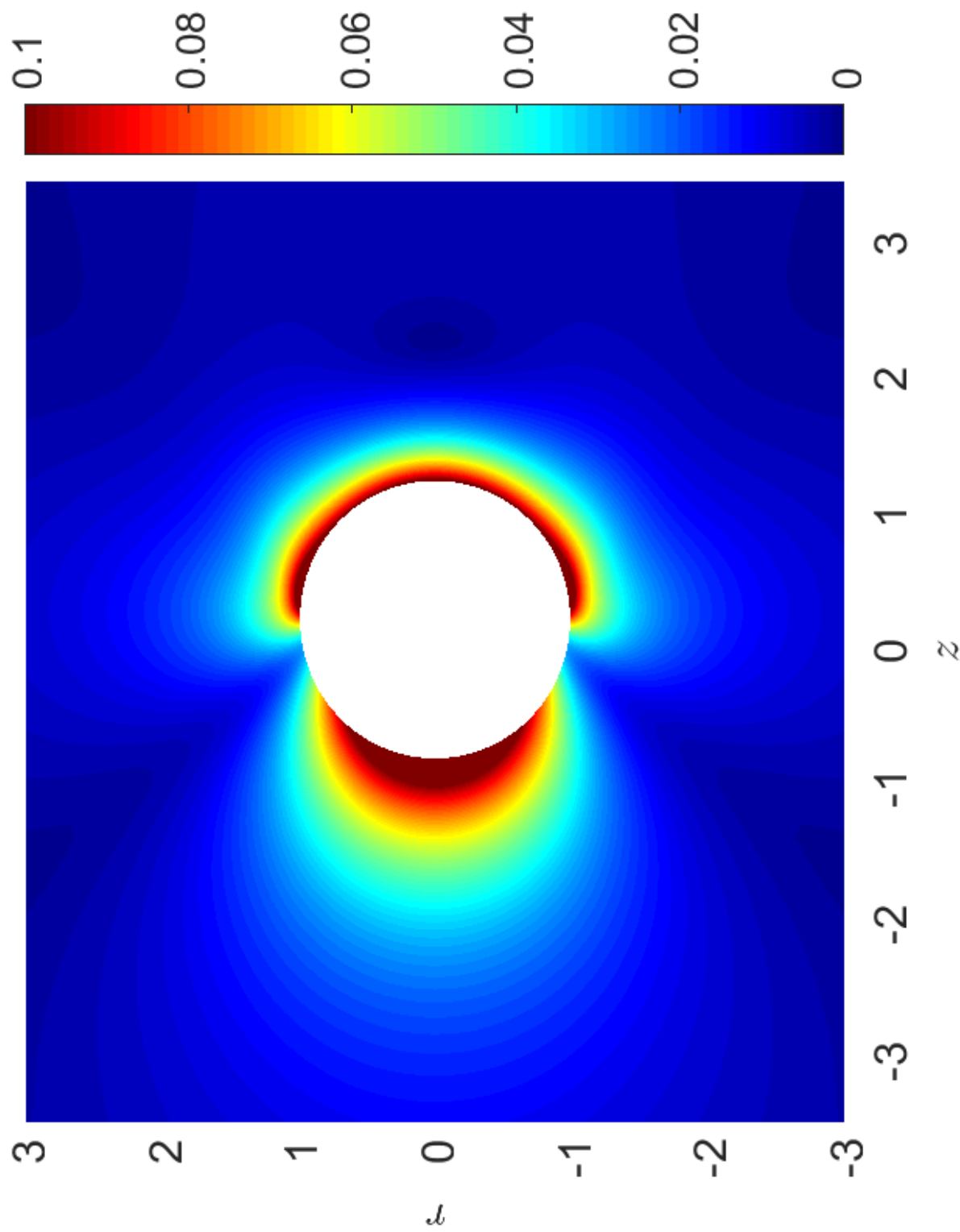
Fig. 2.13. **Cross sectional velocity field showing the velocity magnitude field of an active bubble moving across the z-axis.** The velocity magnitude $|V|$ of the outer viscous fluid with red representing higher $|V|$ and blue representing little to no $|V|$ during self-propulsion of a small contaminated bubble with $\varepsilon = 9.6\%$, $Ma = 2$, $Pe = 140$, and $Re = 10^{-4}$.

2.1). Starting from the normalized initial value $\gamma = 1$, the surfactant concentration at the front of the bubble ($s = 0$) decreases monotonically with time, and eventually attains the value corresponding to the theoretical equilibrium concentration $\gamma = 0.096$ shown by the dashed black line. Figure 2.15 represents the migration of surfactant (red) across the interface of the bubble as it coats the clean (blue) surface at different times from $t \approx 0.3$ to $t \approx 11$.

The presence of the surfactant lowers the surface tension, creating an imbalance of stresses on the bubble interface that leads to interfacial motion. Figure 2.16 shows the tangential velocity of the interface v_t induced by the surfactant gradients (Marangoni stresses). The results show that the maximum interfacial velocity is large at early times when the interfacial gradients are strong and then decrease with time as the interfacial surfactant gradients weaken. The velocity generated by the interfacial gradients drags the surfactant causing the surfactant to spread toward the back of the bubble.

As surfactant migrates across the bubble surface Marangoni stresses are generated. By focusing on the tangential velocity v_t (solid blue line) and surfactant concentration γ (solid red line) values across the interface at a single time ($t = 0.3$) in Figure 2.17, it is seen that the peak v_t occurs at the location on the bubble surface with the strongest surfactant gradient.

The impact of a large surface tension gradient is shown by the larger peaks in tangential v_t and normal v_n velocities (Figures 2.16 and 2.18) across the bubble normalized arc-length s at earlier times. These large velocities on the bubble interface resulted in the deformation and elongation of the bubble. As the magnitude of the concentration γ front on the bubble interface begins to diminish at later times (Figure 2.14) the corresponding tangential v_t and normal v_n velocities (Figures 2.16 and 2.18) on the bubble interface are also shown to diminish with the peaks becoming smaller as the bubble finishes its movement with the concentration reaching equilibrium across the interface.

Mechanisms associated with the active bubble movement on the bubble interface were discussed in this section. Large tangential and normal velocities on the bubble normalized arc-length were seen at the location of the surfactant front. This surfactant front is the origin of Marangoni stresses causing the bubble motion.

2.4.3 Outer Flow Regime

The presence of surfactant gradients also influences the bulk hydrodynamics by the coupling of the interfacial motion with the bulk liquid flow through momentum transfer. Figure 2.19 shows how the motion of the concentration across the interface is linked to the bulk dynamics of the outer-fluid. During early stages of the process, when the gradients of concentration, and therefore Marangoni stresses, are comparatively large at $s \approx 0.2$ the outer-fluid is set into motion towards the rear part of the bubble. This is seen clearly in Figure 2.20 (a) and (b) by following the arrow direction. At these early times, fluid is being pulled from in front of the bubble, around the bubble interface and then inwards towards the rear end of the bubble.

The full picture, in general, shows fluid being pulled inward from in front of and behind the bubble on the axis of propulsion (z-axis) at early times (Figure 2.20 (a) and (b)). However, at $t \approx 3$ (Figure 2.20 (c)) the bubble experiences a transition from the hydrodynamics seen in (a) and (b), to the fluid being pushed outward from in front of the bubble and pulled inward at the back end of the bubble on the axis of propulsion.

After the hydrodynamic transition, shown in Figure 2.20 (c), the bubble enters into its final hydrodynamic state and remains in this state until the bubble motion is completed. Figure 2.20 (d) at $t \approx 6$ shows this final hydrodynamic state with fluid being pushed from in front of the bubble as well as from behind the on the axis of propulsion. This final hydrodynamic state of the external fluid (Figure 2.20 (d)) directly contrasts the initial hydrodynamic state (Figure 2.20 (a) and (b)) where the fluid is being pulled inward from in front of and behind of the bubble.
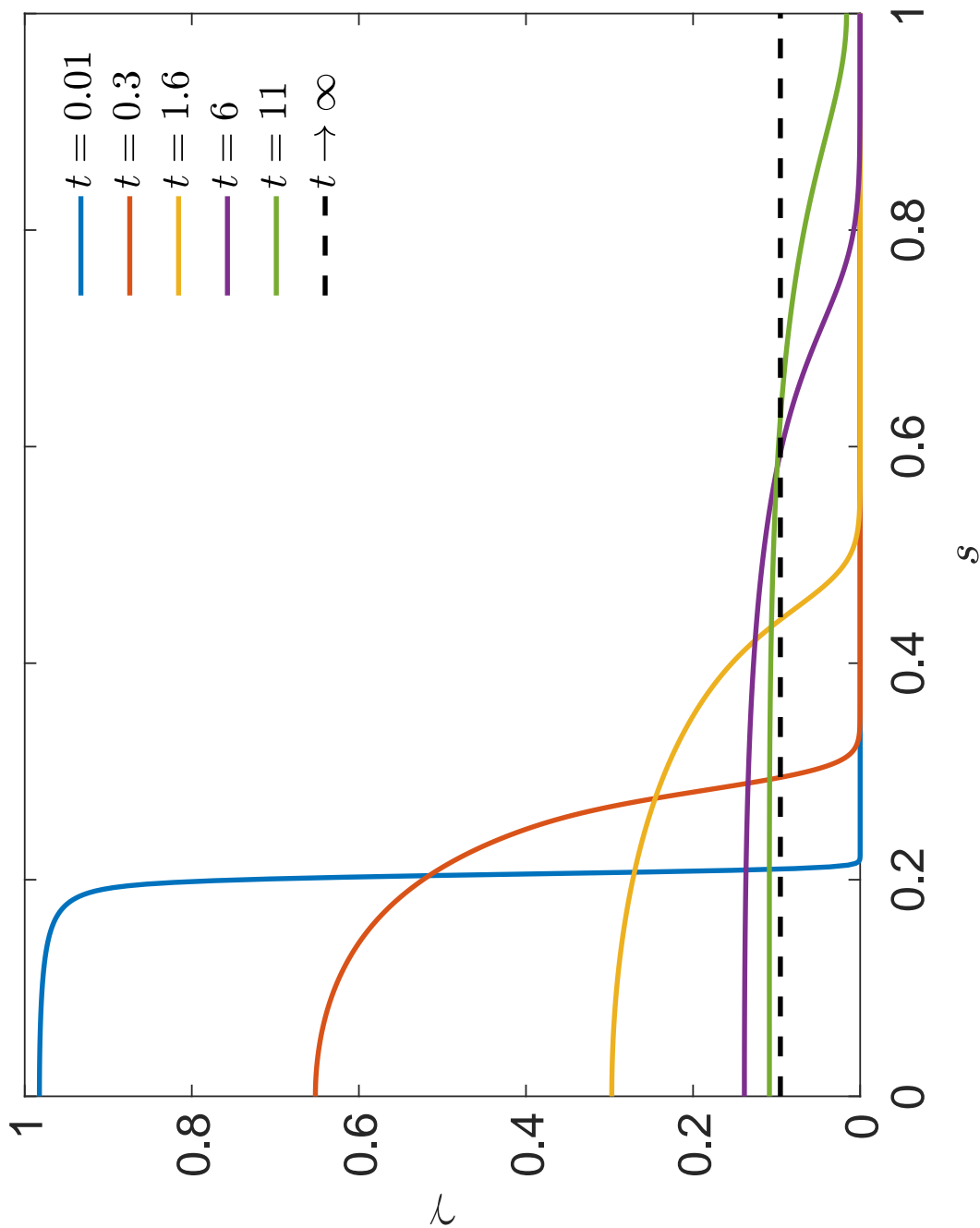
Fig. 2.14. **Temporal evolution of concentration profiles on the bubble interface.** Plot shows the surfactant concentration γ across the bubble normalized arc-length s at various times during self-propulsion of a small contaminated bubble with $\varepsilon = 9.6\%$, $Ma = 2$, $Pe = 140$, and $Re = 10^{-4}$.

(a) $t = 0.3$

(b) $t = 0.6$

(c) $t = 3$

(d) $t = 4$

(e) $t = 6$

(f) $t = 11$
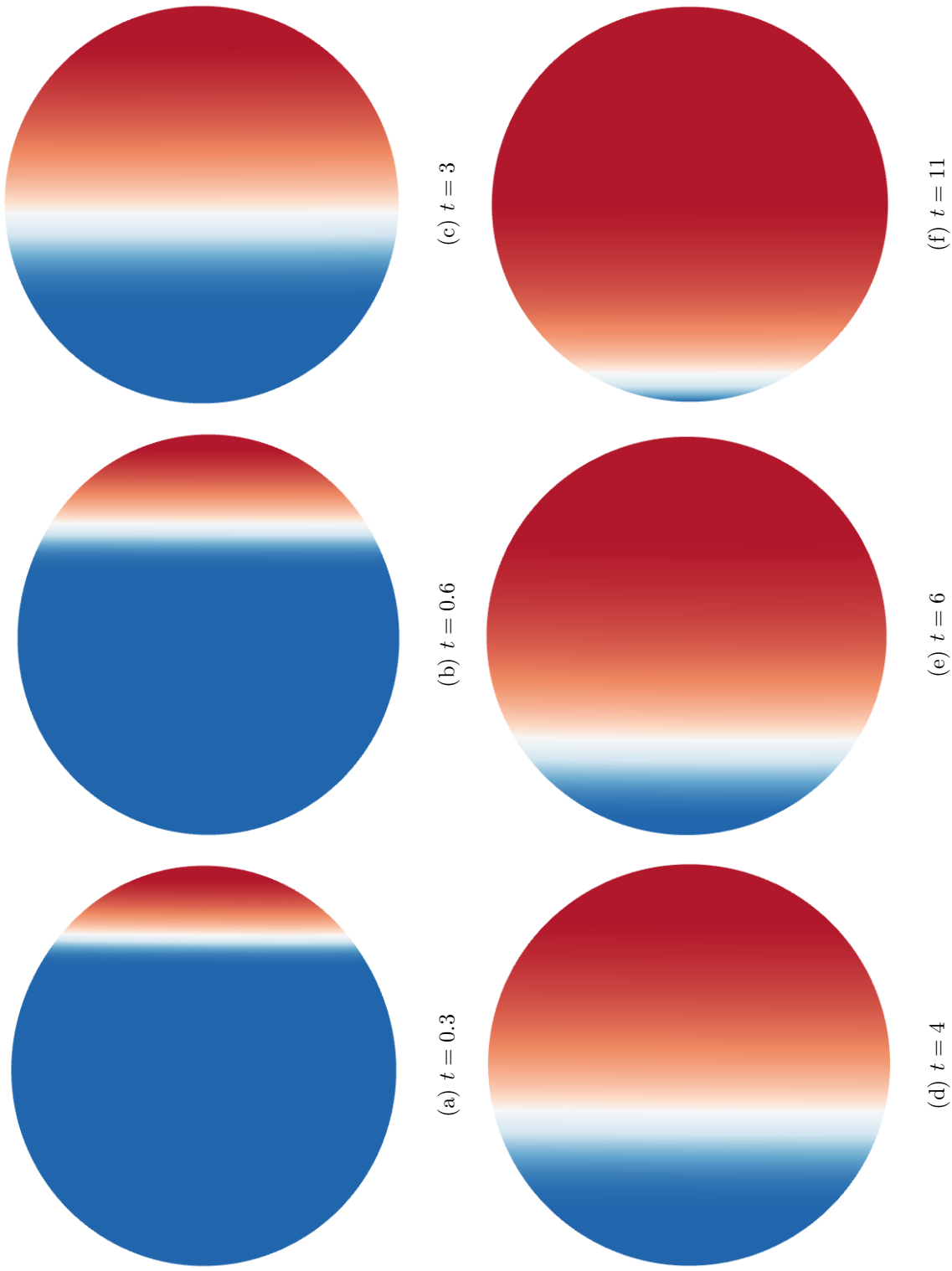
Fig. 2.15. **Temporal evolution of concentration contour on the bubble interface.** Shows the surfactant concentration on the bubble normalized arc-length s at various times t. Where blue is a clean interface and red is a contaminated interface during self-propulsion of a small contaminated bubble with $\varepsilon = 9.6\%$, $Ma = 2$, $Pe = 140$, and $Re = 10^{-4}$.
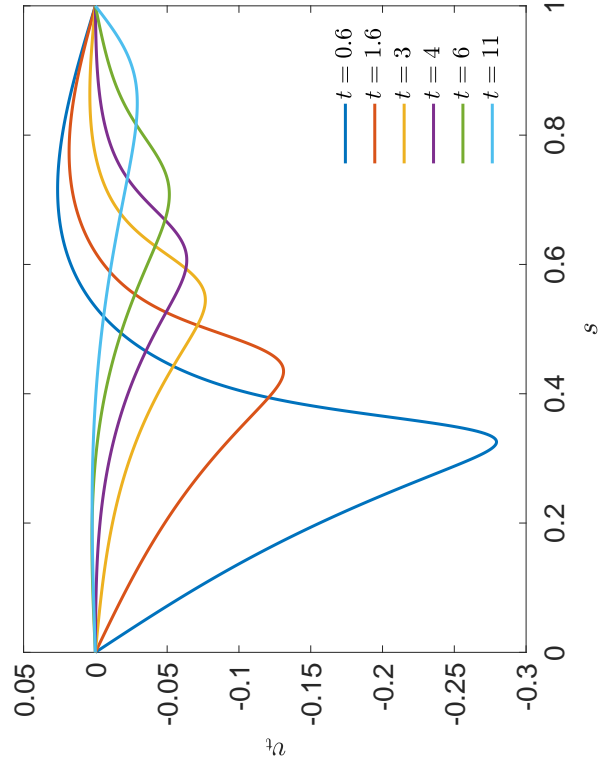
(a) Early times
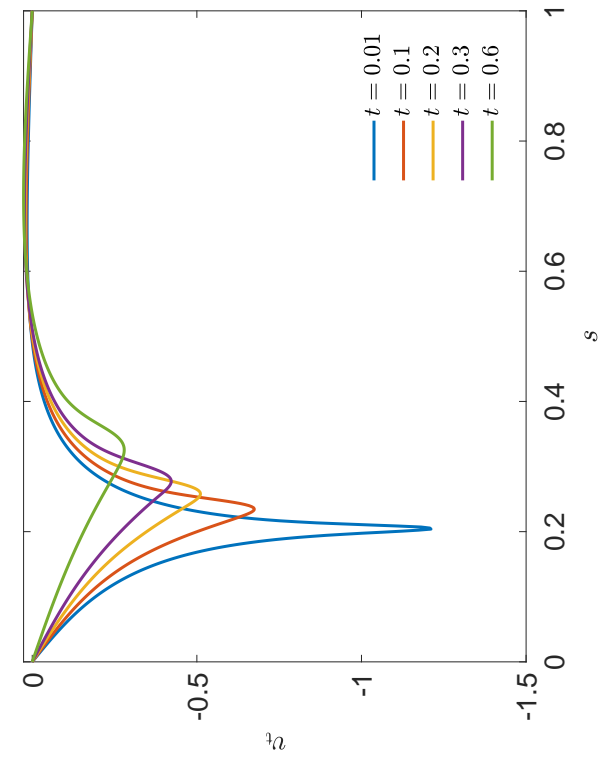
(b) Later Times

Fig. 2.16. **Temporal evolution of tangential velocity profiles on the bubble interface.** Plot shows the tangential velocity v_t across the bubble normalized arc-length s at various early (a) and late (b) times during self-propulsion of a small contaminated bubble with $\varepsilon = 9.6\%$, $Ma = 2$, $Pe = 140$, and $Re = 10^{-4}$.
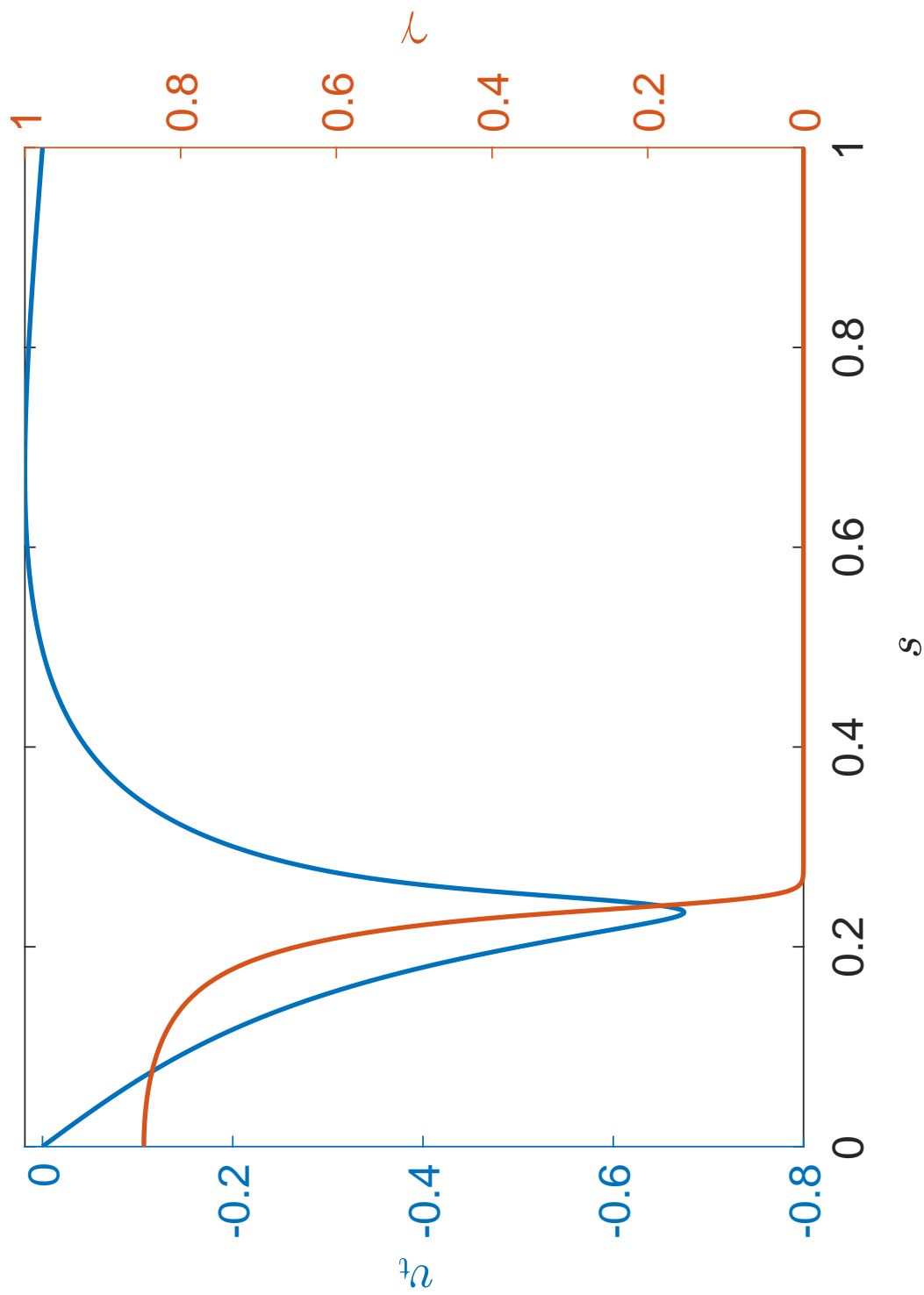
Fig. 2.17. **Active bubble interfacial tangential velocity and concentration comparison.** This plot shows the tangential velocity v_t (blue, left) and concentration γ (orange, right) along the bubble interfacial normalized arc-length s at $t = 0.3$ during self-propulsion of a small contaminated bubble with $\varepsilon = 9.6\%$, $Ma = 2$, $Pe = 140$, and $Re = 10^{-4}$.
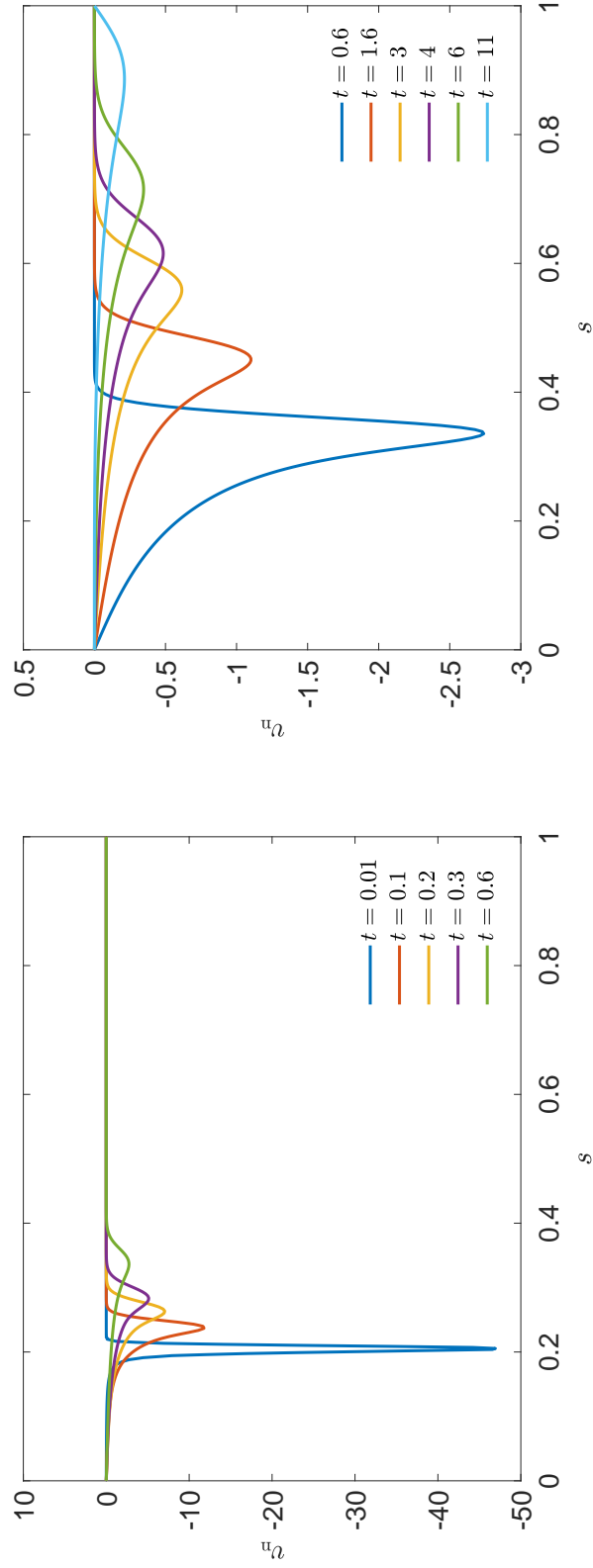
(a) Early times

(b) Later times

Fig. 2.18. **Temporal evolution of normal velocity profiles on the bubble interface.** Plot shows the normal velocity v_n across the bubble normalized arc-length s at various early (a) and late (b) times during self-propulsion of a small contaminated bubble with $\varepsilon = 9.6\%$, $Ma = 2$, $Pe = 140$, and $Re = 10^{-4}$.

This critical transition discussed above between two characteristic hydrodynamic states of self-propulsion is to my knowledge investigated for the first time in self-induced surface-active bubbles. The initial dynamic of this active bubble, seen in Figure 2.20 (a) and (b), is described by the far-field hydrodynamics created by the active motion of the bubble producing inflow of the outer liquid along the self-propulsion axis from both in front of and behind the bubble. This hydrodynamic behavior is characteristic of a general class of swimmers classified as 'pullers' [39], and is illustrated by the black arrows on the z-axis and the red circle at the location of the stagnation point in the snapshot at $t = 0.6$ in Figure 2.21(a). Examples of pullers in nature include *Chlamydomonas reinhardtii* [40], *P. aeruginosa* [41], and amoebae [42]. Pullers initially parallel to one another repel each other [43]. This pulling dynamic is present whenever the surfactant front occurs on the front half of the bubble $s < 0.5$.

The reversal of this behavior is observed at intermediate times, attributed to the crossing of the surfactant front beyond the equator dividing the bubble into front and back hemispheres. Figure 2.20 (c) at $t \approx 3$ clearly shows the transition of the hydrodynamic states with the concentration gradient present approximately at the midpoint of the bubble normalized arc-length at $s \approx 0.5$.

The dynamic after this transition is shown by the black arrows on the z-axis and the red circle at the location of the stagnation point in the snapshot at $t = 6$ in 2.21(b). It is observed that at this time the motion produces outflow of the liquid away from the bubble along the self-propulsion axis (z-axis), which in previous works is described as a 'pusher' [39]. Examples of pushers seen in nature include flagellated cells [42], *Escherichia coli* [40], and spermatozoa [44]. Contrary to pullers, parallel pushers approach one another due to hydrodynamic attractions [43]. This phenomenon is important to understanding swarming tendencies exhibited by many microorganisms and bacteria [45], as well as understanding how to concentrate active swimmers for oil recovery or microbubble cleaning.

The results in Figure 2.21 provide evidence, for the first time, of self-induced 'puller-to-pusher' transition in a bubble. Alternating puller-to-pusher transition was previously only seen by microorganisms [41]. The first definition of a puller and pusher comes from [42] where a 'puller' is described as having the propelling edge of the microswimmer also being the leading edge. A 'pusher' is described as having the propelling edge as the lagging edge on the self-propulsion axis. The results provided in Figure 2.9 support that the bubble is a puller initially with the leading front edge having a larger velocity v_F (solid red line) at early times. At later times the lagging back edge v_B becomes larger when the bubble transitions into a pusher. Figure 2.22 (a) and (b) show at early times the bulk fluid in front of the bubble experiences the larger velocity, and at later times for (c) and (d) the outer fluid at the back end experiences larger velocity as the hydrodynamics transition from a puller to a pusher. This time dependent transition in the far-field hydrodynamics may have important consequences for interactions between swimmers or with swimmers having neighboring boundaries ([14], [15], [46]), originating transitory patterns of attraction and repulsion depending on the Marangoni influence at the interface.

(a) $t = 0.3$

(b) $t = 0.6$

(c) $t = 3$

(d) $t = 6$
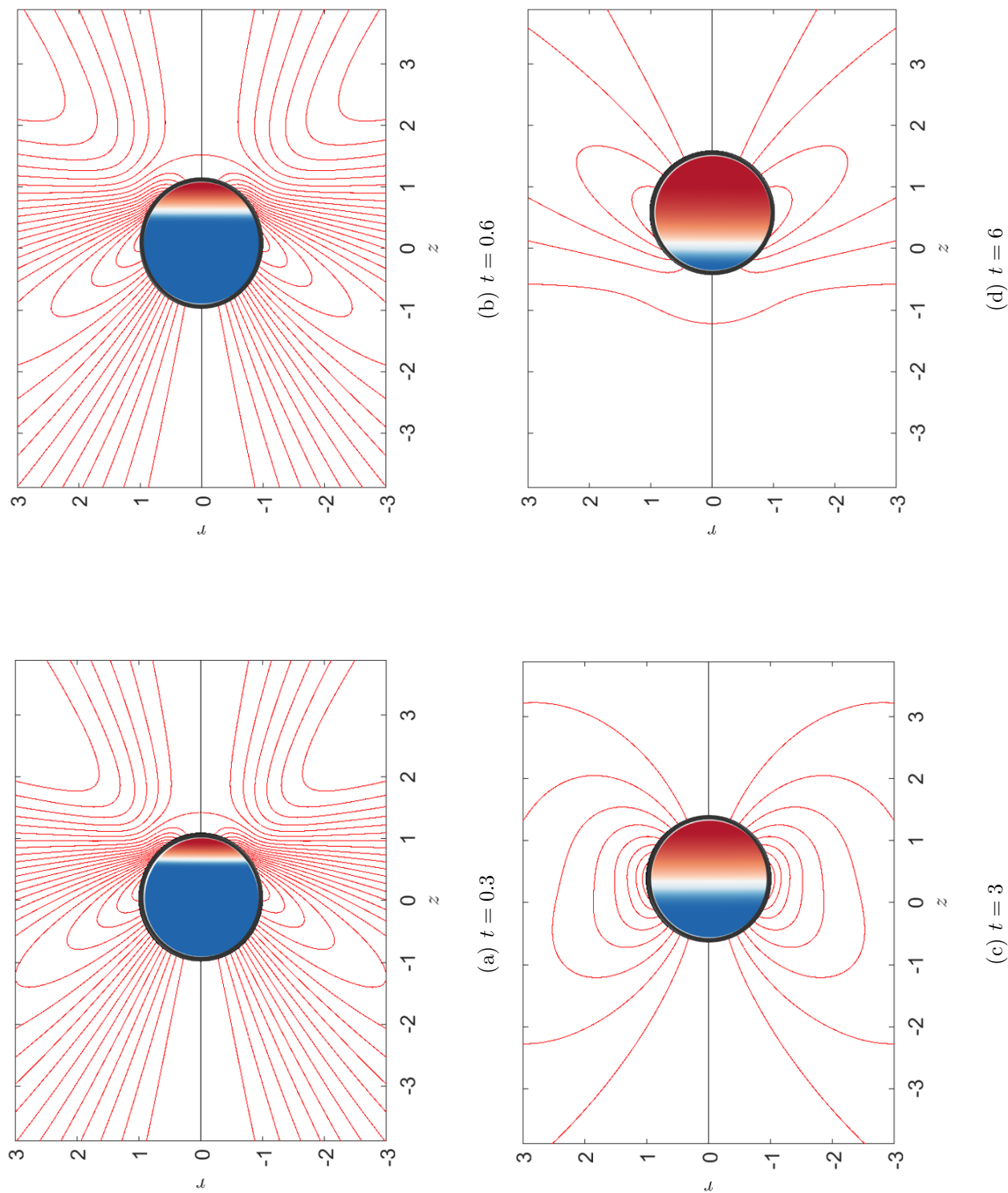
Fig. 2.19. **Temporal evolution of the outer-fluid velocity streamlines and interfacial concentration contour for the active bubble.** Plot shows outer-fluid streamlines and surfactant concentration contour, where blue is a clean interface and red is a contaminated interface, at various times t from early time (a) to late time (d) during self-propulsion of a small contaminated bubble with $\varepsilon = 9.6\%$, $Ma = 2$, $Pe = 140$, and $Re = 10^{-4}$.

45

(a) $t = 0.3$

(b) $t = 0.6$

(c) $t = 3$

(d) $t = 6$
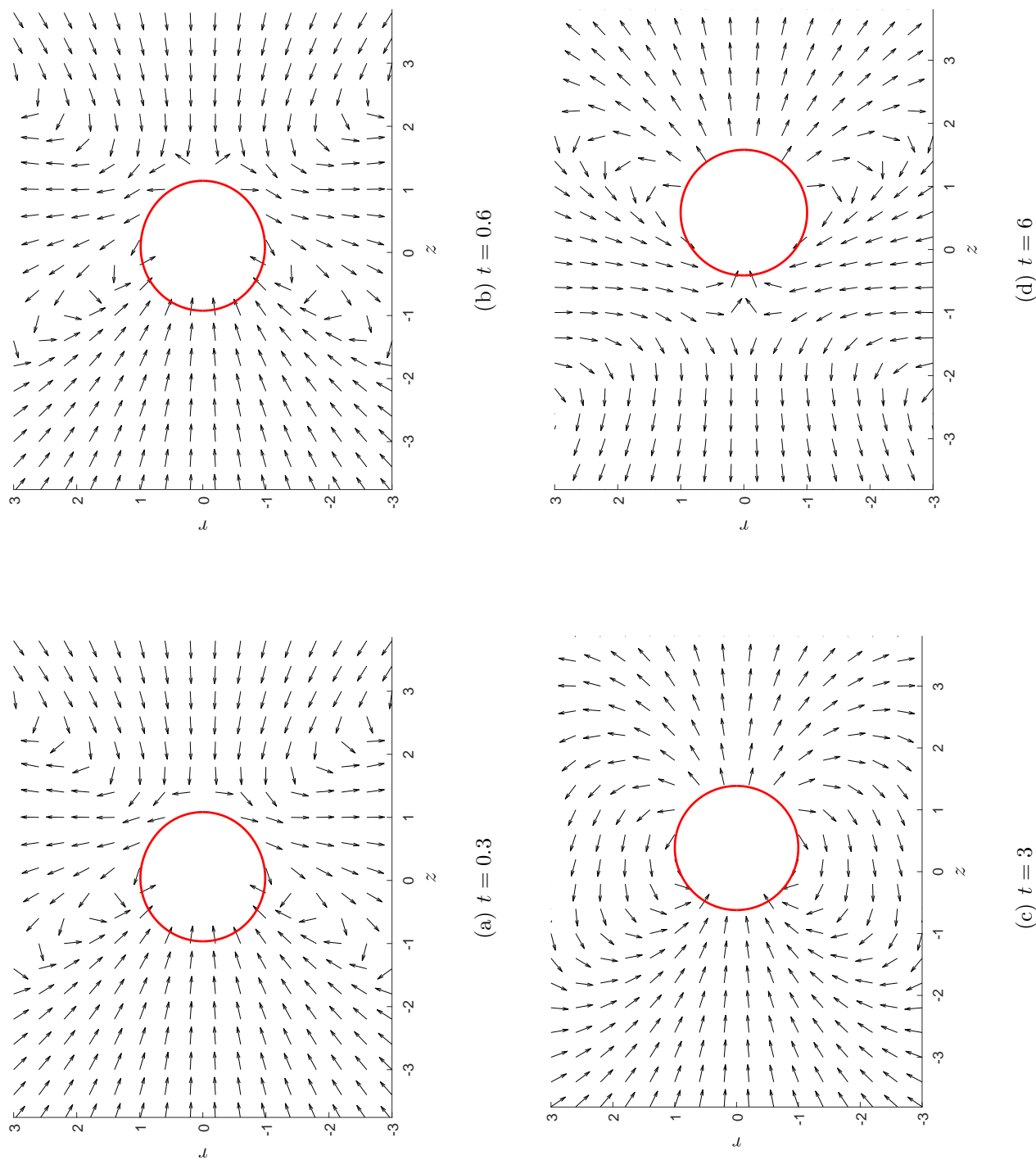
Fig. 2.20. **Temporal evolution of the velocity arrow field for the active bubble.** The evolution of the velocity arrow field of the outer viscous fluid over time, from early time (a) to late time (d), during self-propulsion of a small contaminated bubble with $\varepsilon = 9.6\%$, $Ma = 2$, $Pe = 140$, and $Re = 10^{-4}$.

(a) $t = 1.6$

(b) $t = 6$
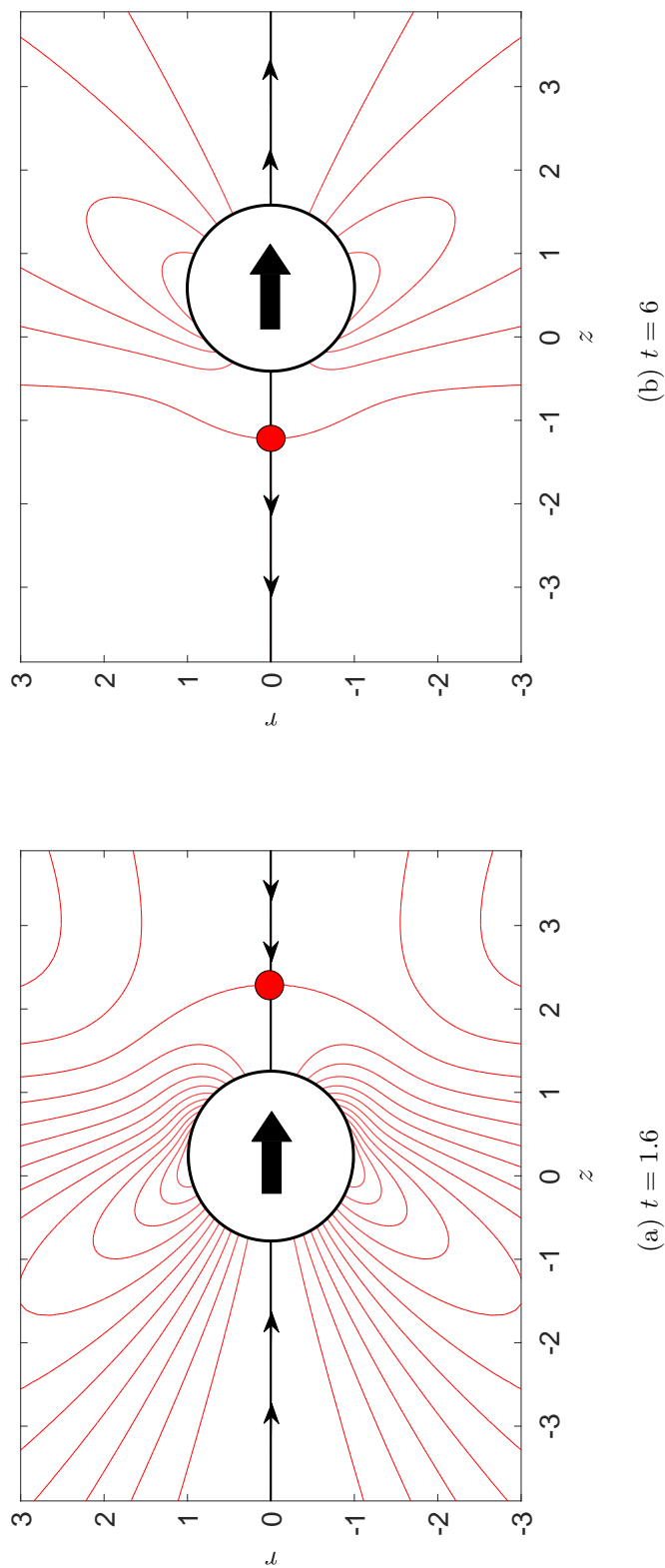
Fig. 2.21. **Active bubble hydrodynamic state streamline comparison.** Comparing the bubble stream-lines at an early time (a) where the bubble exhibits a pulling behavior, and at a later time (b) where the bubble exhibits a pushing behavior. The stagnation point is represented by the red circle on the z-axis and the direction the bubble is moving is represented by the black arrow inside the bubble during self-propulsion of a small contaminated bubble with $\varepsilon = 9.6\%$, $Ma = 2$, $Pe = 140$, and $Re = 10^{-4}$.
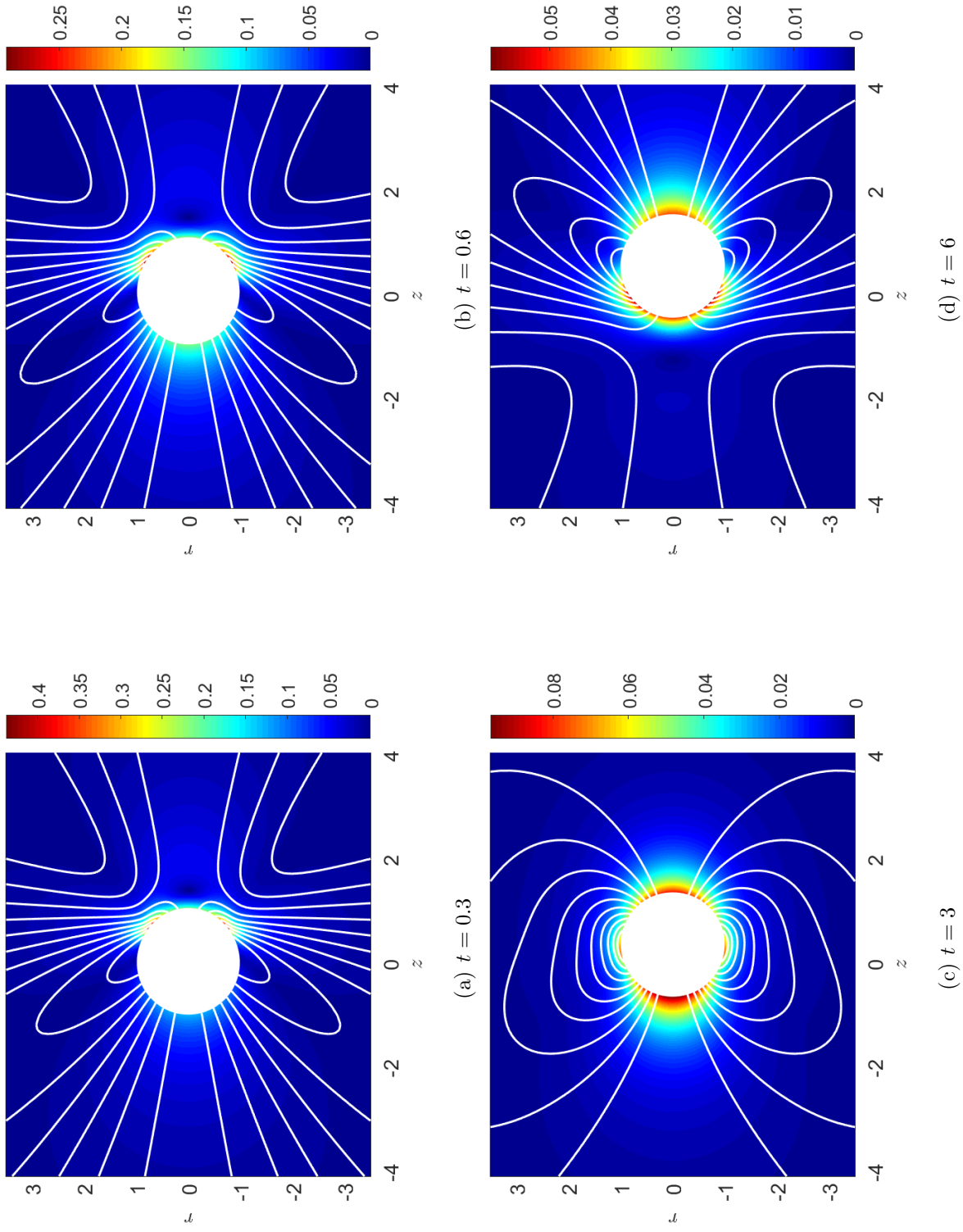
Fig. 2.22. **Temporal evolution of the velocity magnitude field and streamlines for the active bubble.** The evolution of the velocity magnitude $|V|$, blue represents little to no $|V|$ and red represents large $|V|$, of the outer viscous fluid at various times, from early time (a) to late time (d), during self-propulsion of a small contaminated bubble with $\varepsilon = 9.6\%$, $Ma = 2$, $Pe = 140$, and $Re = 10^{-4}$.

2.5   Conclusion

In this chapter a computational model was developed to investigate bubble Marangoni-driven propulsion and the mechanisms behind this motion. In-depth analysis into the mechanics of surfactant gradient generated interfacial motion coupled with the outer-fluid flows by momentum transfer, was made possible by high fidelity simulations. Surfactant spreading across an interface using this simulation was validated against theoretical results. This uneven distribution of surfactant on the bubble interface resulted in bubble deformation at early times when large Marangoni stresses were present. A shift in a bubble hydrodynamic condition first observed with the bubble changing from a puller, at early times when Marangoni stresses acted on the front half, to a pusher, at later times when Marangoni stresses were acting on the back half of the bubble. To help understand small scale dynamics involved with bubble cleaning and microorganism movement, it is important to know how the particles are interacting with one another based on whether they are in the pusher or puller state.

3. INFLUENCE OF SURFACTANT PROPERTIES AND SOLID BOUNDARIES ON BUBBLE SELF-PROPULSION

3.1 Introduction

In this chapter, the influence of initial conditions and surfactant properties on Marangoni propulsion are characterized parametrically. Here, a quantative study over the influence of the degree of initial surfactant coverage ε, the influence of surfactant strength Ma, and the influence of neighboring solid tubular boundaries R_t on the bubble microscopic active motion mechanisms as well as the overall bubble speed and displacement is conducted. Understanding the impact of these parameters will help understand the mechanisms of microbubble propulsion. Uncovering the affect that these parameters have on bubble self-propulsion macroscopic flow regime and the correlating transport of surfactant on the bubble free-surface is essential in further understanding the properties of bubble active motion.

3.2 Influence of Initial Surfactant Coverage ε on Bubble Propulsion

Here the influence of surfactant coverage on a self-propelled bubble moving in a viscous fluid is described. First, an initial coverage of $\varepsilon = 90.4\%$, $\alpha = 0.8$ (seen in Figure 3.1(a)) is examined. This is antipodal to the coverage discussed in Chapter 2 of $\varepsilon = 9.6\%$, $\alpha = 0.2$ (seen in Figure 3.1(b)). The initial surfactant coverage in Figure 3.1(a) is equivalent to the initial clean region of the bubble investigated in Chapter 2 seen in Figure 3.1(b). Qualitatively, the situation described with a bubble with surfactant coverage $\varepsilon = 90.4\%$ is a common occurrence in microbubble cleaning when a large contaminated bubble coalesces with a smaller clean bubble resulting in

a contaminated bubble with a small clean patch as seen in Figure 3.2. All bubble interactions in this section have Marangoni of $Ma = 2$, Peclet of $Pe = 140$ in a very viscous solution, i.e. $Re = 10^{-4} \ll 1$.

The bubble with initial coverage of $\varepsilon = 90.4\%$ shares similar qualities with a bubble of initial coverage $\varepsilon = 9.6\%$. During early stages of the process (up to $t \approx 0.01$) the center of mass z_M of the bubble moves in a nearly identical manner for both values of ε, as seen in Figure 3.3 where displacement d is plotted against time t. This is also seen by comparing the speed of the bubble center of mass v_M in Figure 3.4 where the velocities between $\varepsilon = 90.4\%$ and 9.6% are almost identical until they separate at $t \approx 0.01$. This is not surprising when considering that the initial coverage values are antipodal, area of the initial clean region for $\varepsilon = 90.4\%$ is equal to the area of the contaminated region for $\varepsilon = 9.6\%$, until time $t \approx 0.01$ (solid blue line). At the time $t \approx 0.01$ the concentration front has moved an insignificant amount from its initial position along the bubble normalized arc-length at $s = \alpha$ when $\alpha = 0.8$ in Figure 3.5 showing concentration γ over the normalized bubble arc-length s. As time advances. when the surfactant front moves further from its initial position, important differences become evident between both cases.

Figure 3.4 shows that the bubble with larger initial surfactant coverage has a decrease in speed v significantly earlier than the bubble with initially smaller coverage. Consequently, the bubble with larger coverage travels a shorter distance with time. The differences appear as the initial similarities in the location of the surfactant front across the plane $z = 0$ vanishes since in both cases the concentration front moves toward the rear part of the bubble. Once the concentration front reaches this point ($s = 1$), the Marangoni flow that drives the bubble forward starts to diminish. However, the bubble still moves an additional minor distance, shown in Figure 3.3 depicting displacement d versus time t. Given the smaller distance to the back part of the bubble, when $\alpha = 0.8$, the concentration front arrives to this point earlier, $t \approx 0.7$, than for $\alpha = 0.2$,$t \approx 11$. This smaller distance the front needs to travel
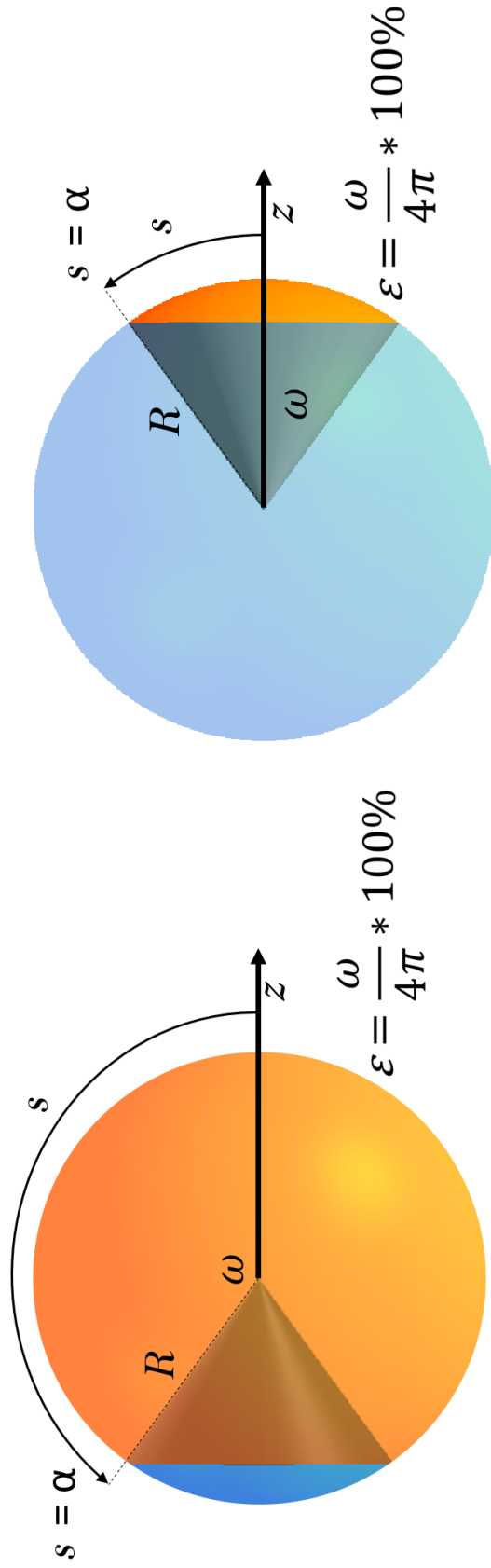
(a) $\varepsilon = 90.4\%$, $\alpha = 0.8$

(b) $\varepsilon = 9.6\%$, $\alpha = 0.2$

Fig. 3.1. **Sketch of complimentary initial surfactant coverages for active bubbles.** The two coverages initially compared in this section for a surfactant strength of $Ma = 2$ and outer-fluid viscosity of $Re = 10^{-4}$. The dimensionless radius of the bubble is R, and the location of the surfactant front along the arc length of the bubble is s. The location of the initial surfactant concentration along the bubble normalized arc-length is $s = \alpha$, the initial surfactant concentration is γ_0, the initial solid-angle of coverage of surfactant on the bubble interface is ω, and the initial percent surfactant coverage is ε. The z-axis is shown by the horizontal black arrow.
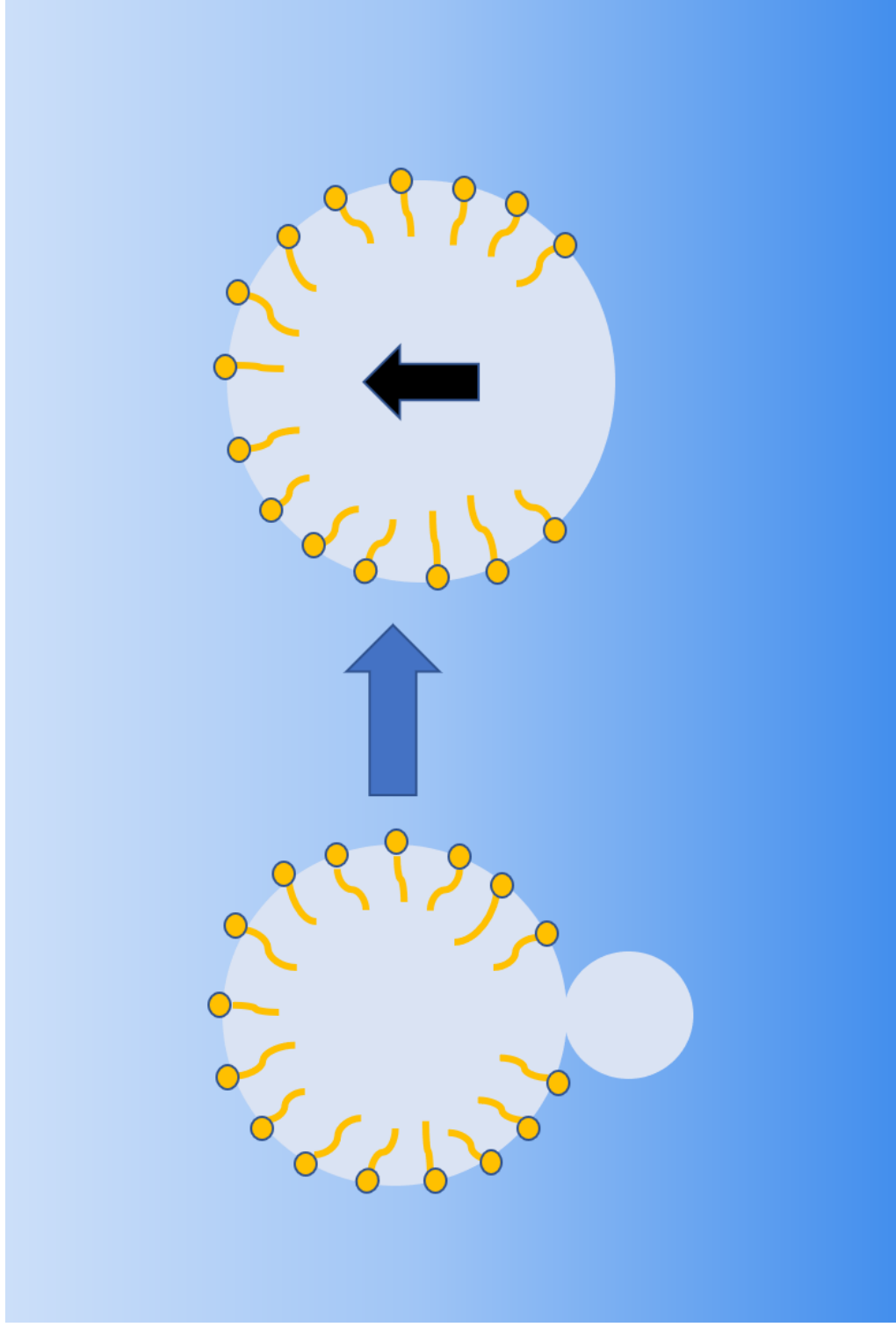
Fig. 3.2. **Sketch of a larger surfactant covered bubble coalescing with a small clean bubble.** This describes how bubble coalescence (occurring on the left) in a fluid can result in a bubble with a large contaminated area (image on the right) creating an active bubble moving in the direction of the black arrow.
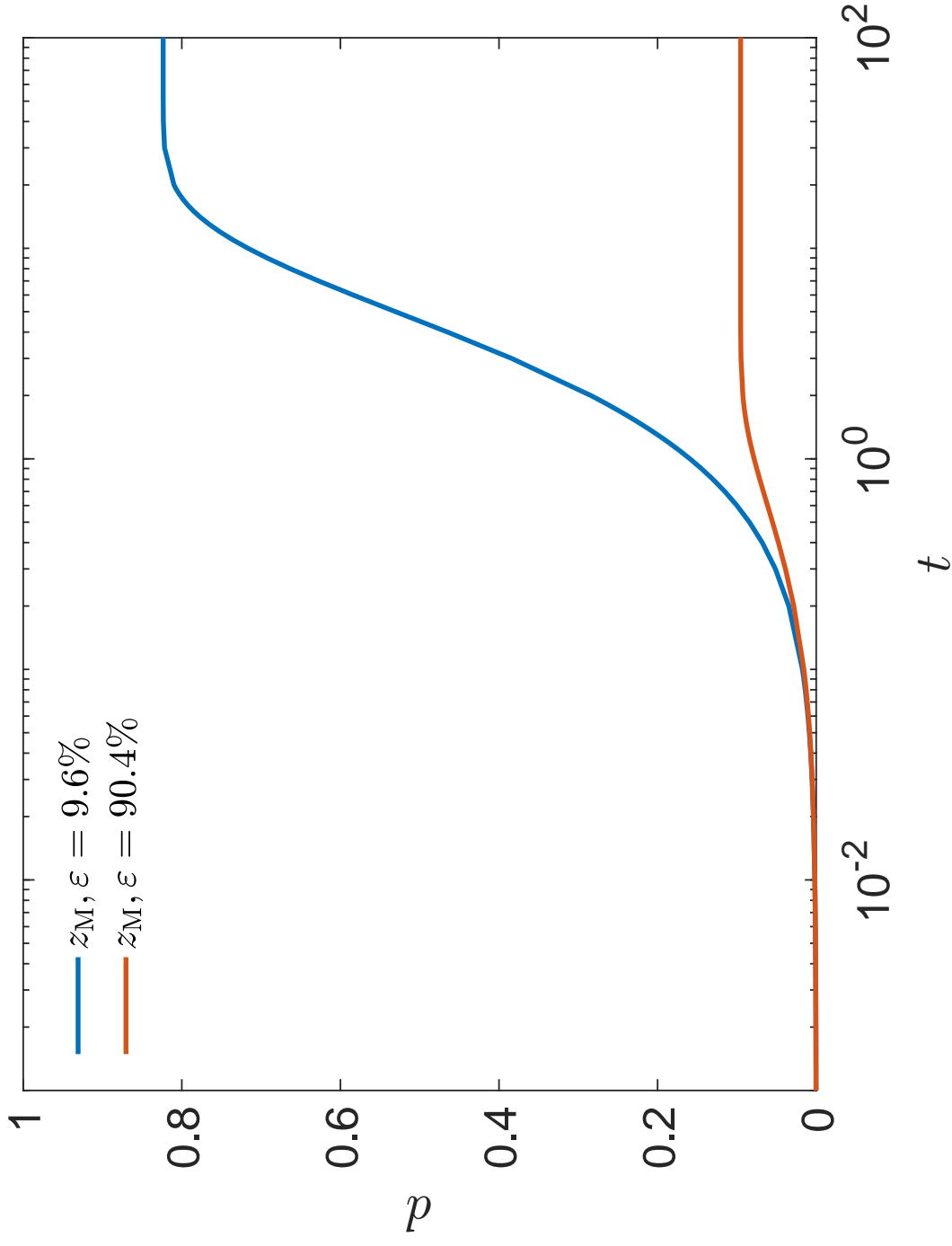
Fig. 3.3. **Temporal evolution of the bubble center of mass displacement for different initial surfactant coverages.** Comparing the displacement d of the center of mass z_M over time t of $\varepsilon = 9.6\%$ (blue line) and $\varepsilon = 90.4\%$ (orange line) for $Re = 10^{-4}$, $Pe = 140$, and $Ma = 2$.
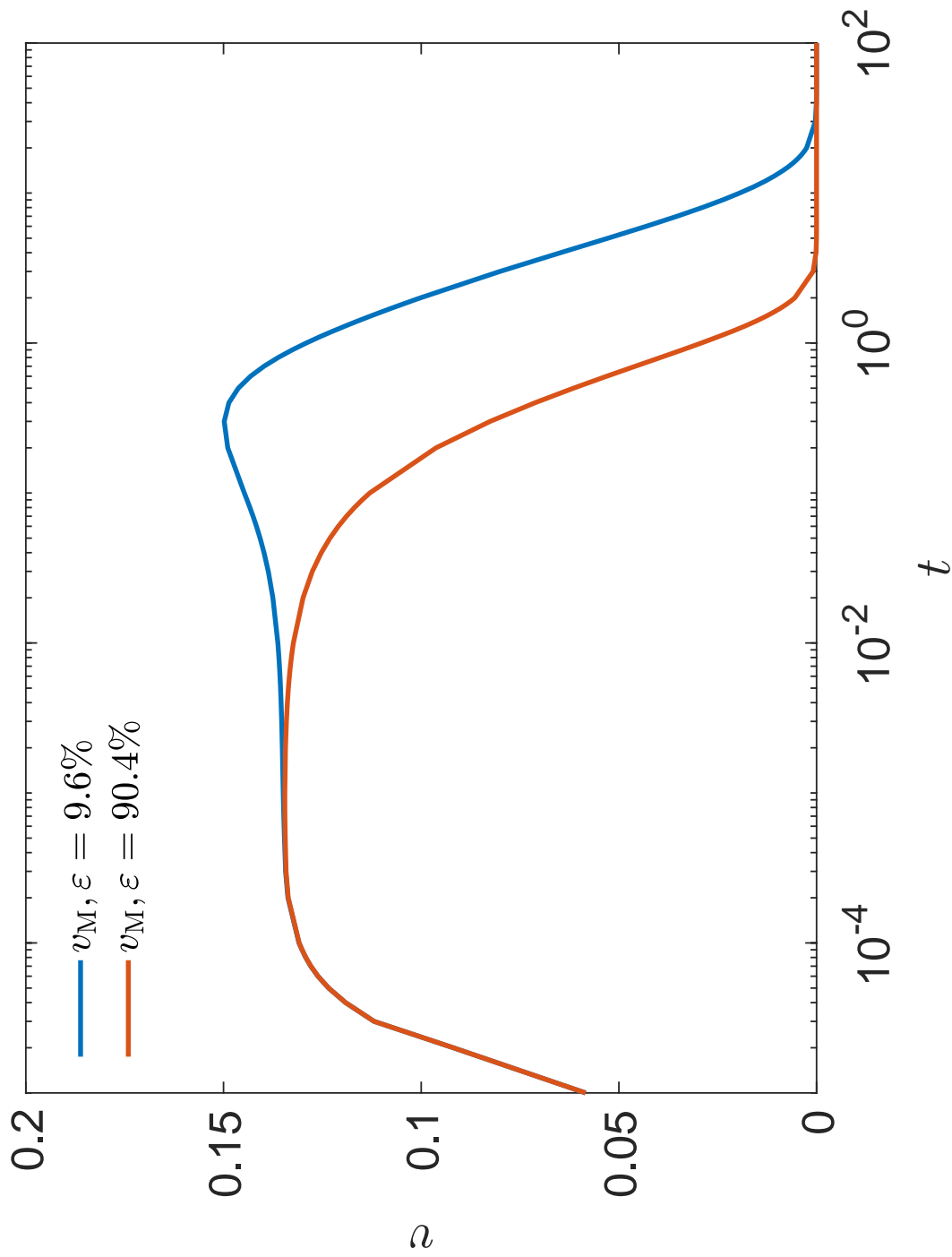
Fig. 3.4. **Temporal evolution of the bubble center of mass velocity for different initial surfactant coverages.** Comparing the velocity v of the center of mass v_M over time t of $\varepsilon = 9.6\%$ (blue line) and $\varepsilon = 90.4\%$ (orange line) for $Re = 10^{-4}$, $Pe = 140$, and $Ma = 2$.

results in a considerably smaller total distance (D) travelled by the bubble at the end of the process:

$$D \equiv \lim_{t \to \infty} z_M(t), \tag{3.1}$$

$D \approx 0.823$ for $\varepsilon = 9.6\%$, $D \approx 0.095$ for $\varepsilon = 90.4\%$. The fact that $D \approx 1 - \varepsilon$ in both cases is not due to a fortunate choice of parameters, but, as shown in the paragraphs below, represents a much more general behavior.

The location of the surfactant gradient has altered how the bubble is deformed depending on which half of the bubble is the location of initial leading edge. Figures 3.6 and 3.7 show the displacements d and velocities v, respectively, of the front and back ends of the bubble over time t. These figures show that the displacement and velocity of the front end of the $\varepsilon = 9.6\%$ bubble (solid blue line) and the back end of $\varepsilon = 90.4\%$ bubble (dashed orange line) follow nearly identical paths until $t \approx 0.1$. During this time the displacement and velocity of the front end of $\varepsilon = 9.6\%$ (solid blue line) and the back end of $\varepsilon = 90.4\%$ (dashed orange line) are larger than their opposite bubble ends. The solid and dashed blue lines for the $\varepsilon = 9.6\%$ bubble front and back, respectively, finally converge at a much larger overall displacement D ($D \approx 0.823$), whereas the solid and dashed orange lines for the $\varepsilon = 90.4\%$ bubble front and back, respectively, converge at a smaller overall displacement D ($D \approx 0.095$). The puller hydrodynamic state is seen at early times with the front end of the $\varepsilon = 9,6\%$ being the leading edge, while the pusher hydrodynamic state can be seen at early times for $\varepsilon = 90.4\%$ with the back end initially being the leading edge.

The result of this difference in displacement and velocity is seen in Figure 3.8 with $\varepsilon = 9.6\%$ shown by a positive flattening f curve (solid blue line) indicating bubble elongation. Flattening is described as $f = 1 - (b/a)^2$, where a is the maximum bubble size in the axial direction and b is the maximum size in the radial direction. This elongation due to the positive flattening curve for $\varepsilon = 9.6\%$ is clearly shown when comparing the initial bubble interface shape (dashed black line) to the interface shape at the time of maximum elongation (solid black line), $t \approx 0.6$, shown in Figure 3.9(b).
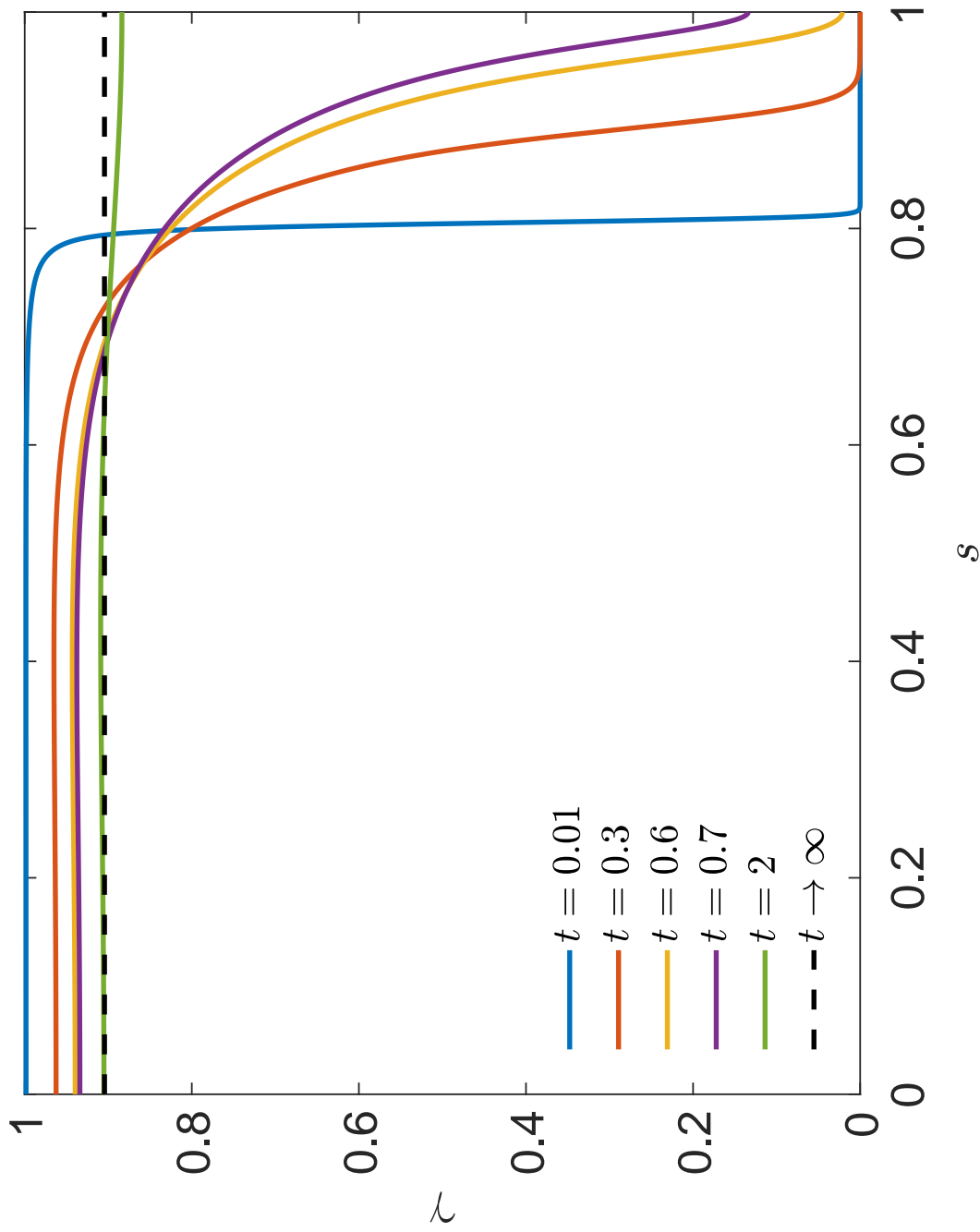
Fig. 3.5. **Temporal evolution of surfactant concentration profile on the bubble interface.** Shows the concentration γ across the bubble normalized arc-length s at various times t for $\varepsilon = 90.4\%$, $Re = 10^{-4}$, $Pe = 140$, and $Ma = 2$.
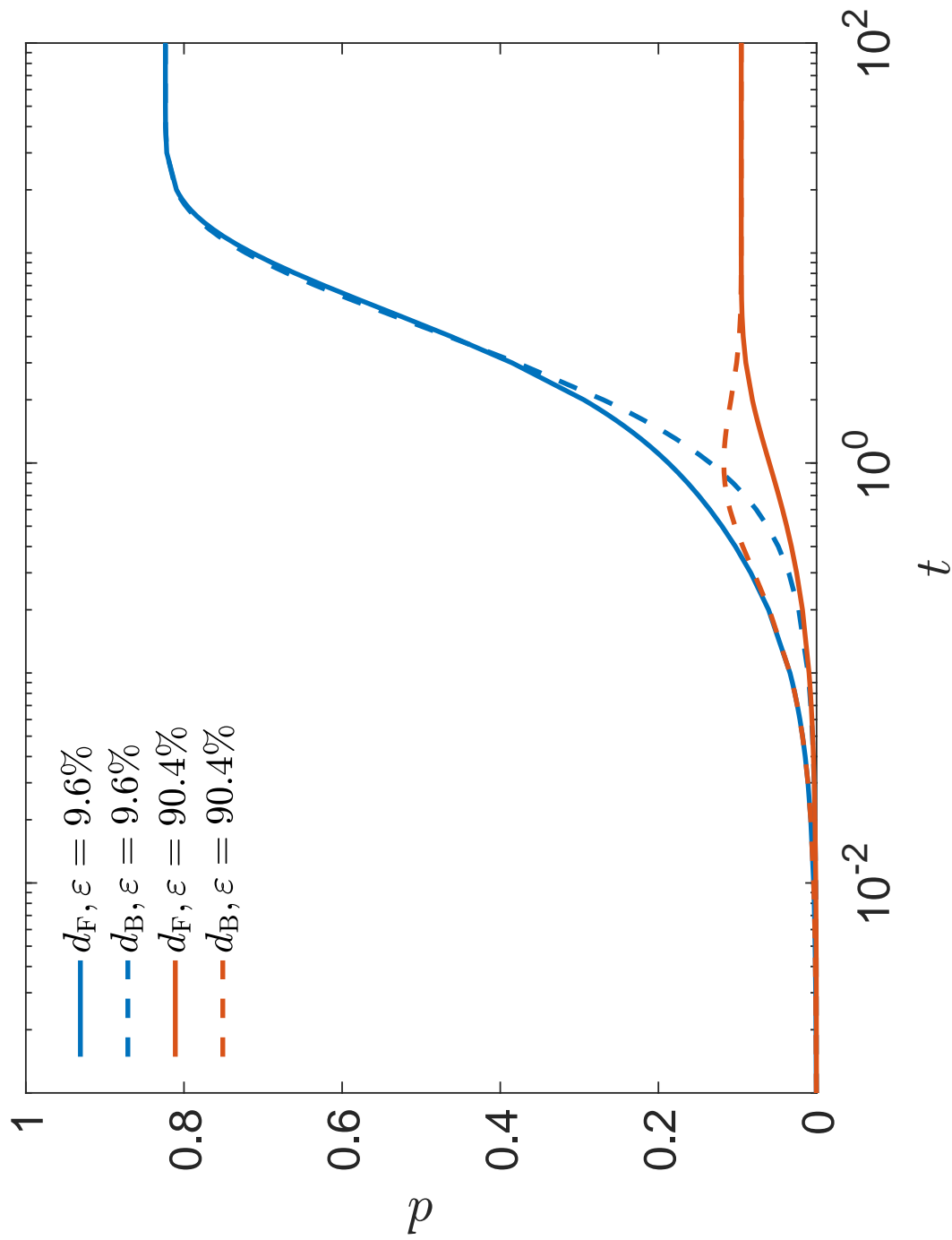
Fig. 3.6. **Temporal evolution of the bubble front and back end displacements for different initial surfactant coverages.** Comparing the displacement d of the bubble front d_F (solid line) and back d_B (dashed line) over time t of $\varepsilon = 9.6\%$ (blue) and $\varepsilon = 90.4\%$ (orange) for $Re = 10^{-4}$, $Pe = 140$, and $Ma = 2$.
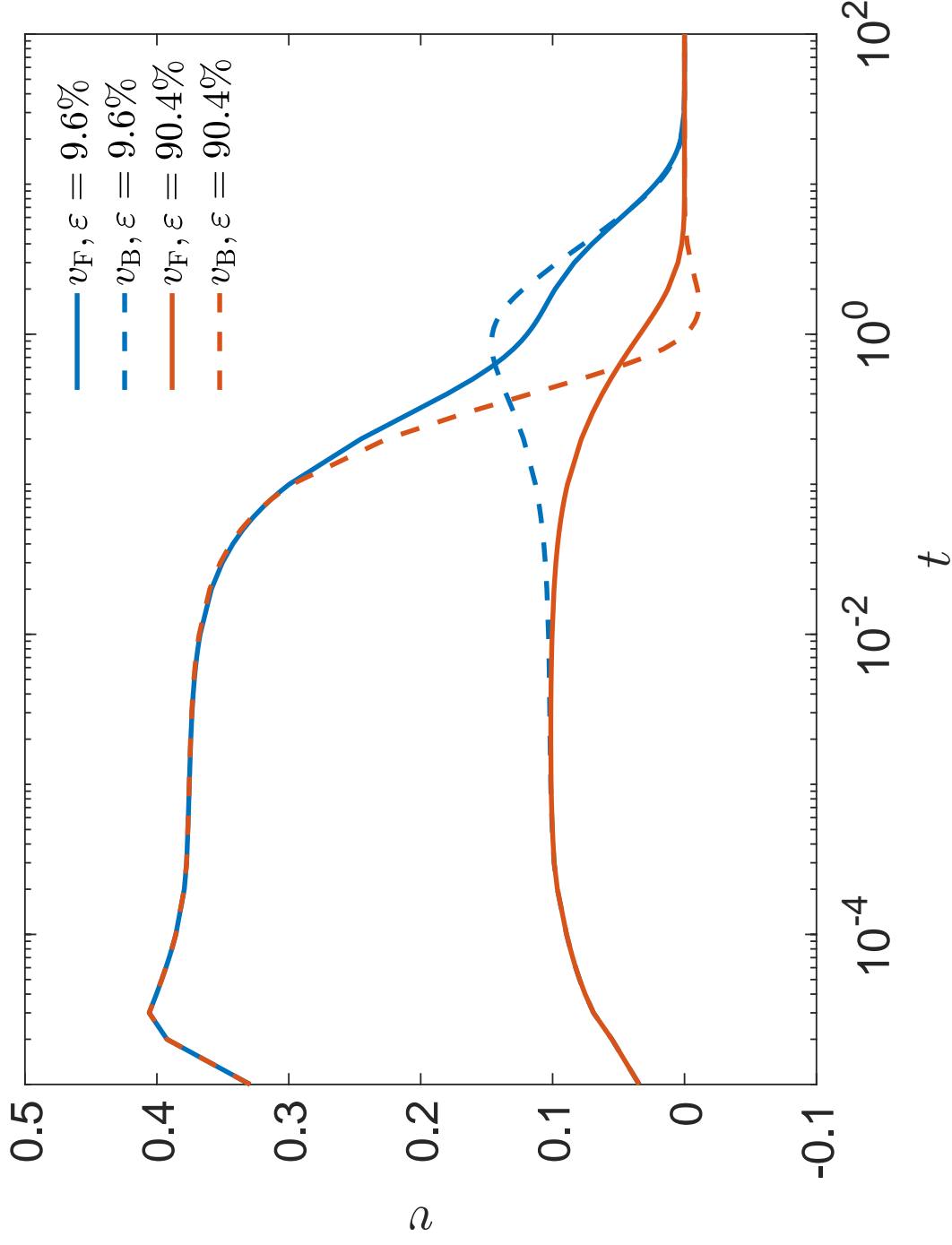
Fig. 3.7. **Temporal evolution of the bubble front and back end velocities for different initial surfactant coverages.** Comparing the velocity v of the bubble front v_F (solid line) and back v_B (dashed line) over time t of $\varepsilon = 9.6\%$ (blue) and $\varepsilon = 90.4\%$ (orange) for $Re = 10^{-4}$, $Pe = 140$, and $Ma = 2$.

$\varepsilon = 90.4\%$ is represented in Figure 3.8 by a similar inverted negative flattening f curve (dashed blue line) indicating compression. The compression of the interface shape is visualized when comparing the initial bubble interface shape (dashed black line) to the interface shape at the time of maximum elongation (solid black line), $t \approx 0.6$, shown in Figure 3.9(a). The minimum values of flattening for $\varepsilon = 9.6\%$ (dashed blue line) is about -5% seen in Figure 3.8. Since the curves for both values of initial coverage are almost symmetric across the horizontal axis, it occurs nearly at the same instant of time as the maximum flattening observed for $\varepsilon = 9.6\%$, at $t \approx 0.6$.

The location of the initial gradient of surface tension on the bubble determines if it is elongated ($\alpha < 0.5$) or compressed ($\alpha > 0.5$) with α describing the initial surfactant coverage across the normalized arc-length of the bubble s. When compression occurs, the bubble swimming with an initial coverage of $\varepsilon = 90.4\%$ has larger tangential velocities v_t at earlier times on the back end of the bubble normalized arc-length s (Figure 3.10) where the surfactant concentration γ gradient is also larger across the back region of bubble interface (Figure 3.5). The $\varepsilon = 90.4\%$ bubble has both the largest concentration gradients and tangential velocities located on the rear half of the bubble $s > 0.5$. As discussed in Chapter 2, elongation occurs in the swimming bubble with $\varepsilon = 9.6\%$ where larger tangential velocities v_t (Figure 2.16) occurring across the bubble normalized arc-length s at locations of large concentration γ gradients (Figure 2.14) located on the front half of the bubble $s < 0.5$.

Finally, since for $\varepsilon = 90.4\%$ there is no transition from puller-to-pusher flow configuration, after the maximum compression f (dashed blue line) (Figure 3.8) at $t \approx 0.6$ the bubble simply recovers its spherical shape. This breaks the symmetry across the horizontal axis of the curve of flattening f versus time t, when compared with the $\varepsilon = 9.6\%$ case (solid blue line) (Figure 3.8). The activity of the macroscopic flow during this compression is visualized in the progression of the velocity magnitude $|V|$ of $\varepsilon = 90.4\%$ in the outer-fluid field shown by Figure 3.11 along with the streamlines of the outer-fluid, whereas 3.12 depicts an enhanced view of the outer-fluid velocity magnitude $|V|$ without the streamlines at the same times for (a)

through (d). As time progresses, the Marangoni stresses, induced by the surfactant gradient, compresses the back end of the bubble as the surfactant travels to the back end of the bubble, by following the larger bulk velocities from (a) to (c) where the remaining Marangoni stresses propel the bubble slightly forward in the positive z direction. The pusher hydrodynamic state is shown throughout the entire movement of the $\varepsilon = 90.4$ bubble with the outer fluid being pushed away from the bubble along the axis of propulsion [39] as shown by arrow velocity field plots in Figure 3.13 (a) though (d).

Instead of the bubble transitioning from puller-to-pusher, the $\varepsilon = 90.4\%$ bubble remains a pusher for the duration of the surfactant migration to the back end $(s = 1)$. When the surfactant front has barely moved from its initial position at $s \approx \alpha$ for $\alpha = 0.2$ (Figure 3.14 (b)), the flow fields and streamline structure are very similar to when the initial coverage is $\alpha = 0.8$ (Figure 3.14 (a)) at the same time $t \approx 0.01$ upon reflection about the plane $z = 0$, except for the direction of the flow.

Figure 3.14(b) shows the early time $(t = 0.01)$ puller configuration corresponding to $\alpha = 0.2$ with a stagnation point ahead of the bubble on the symmetry axis (the bubble is moving to the right), contrastingly Figure 3.14(a) shows the early time $(t = 0.01)$ pusher configuration corresponding to $\varepsilon = 90.4\%$ with a stagnation point behind of the bubble. Figure 3.15(b) shows late time $(t = 6)$ pusher configuration corresponding to $\varepsilon = 9.6\%$ with a stagnation point that is now behind the bubble on the symmetry axis, while Figure 3.15(a) shows the early time $(t = 0.01)$ pusher configuration corresponding to $\varepsilon = 90.4\%$, with a stagnation point behind of the bubble. It also shows how similar the bulk flow fields are between the two configurations.
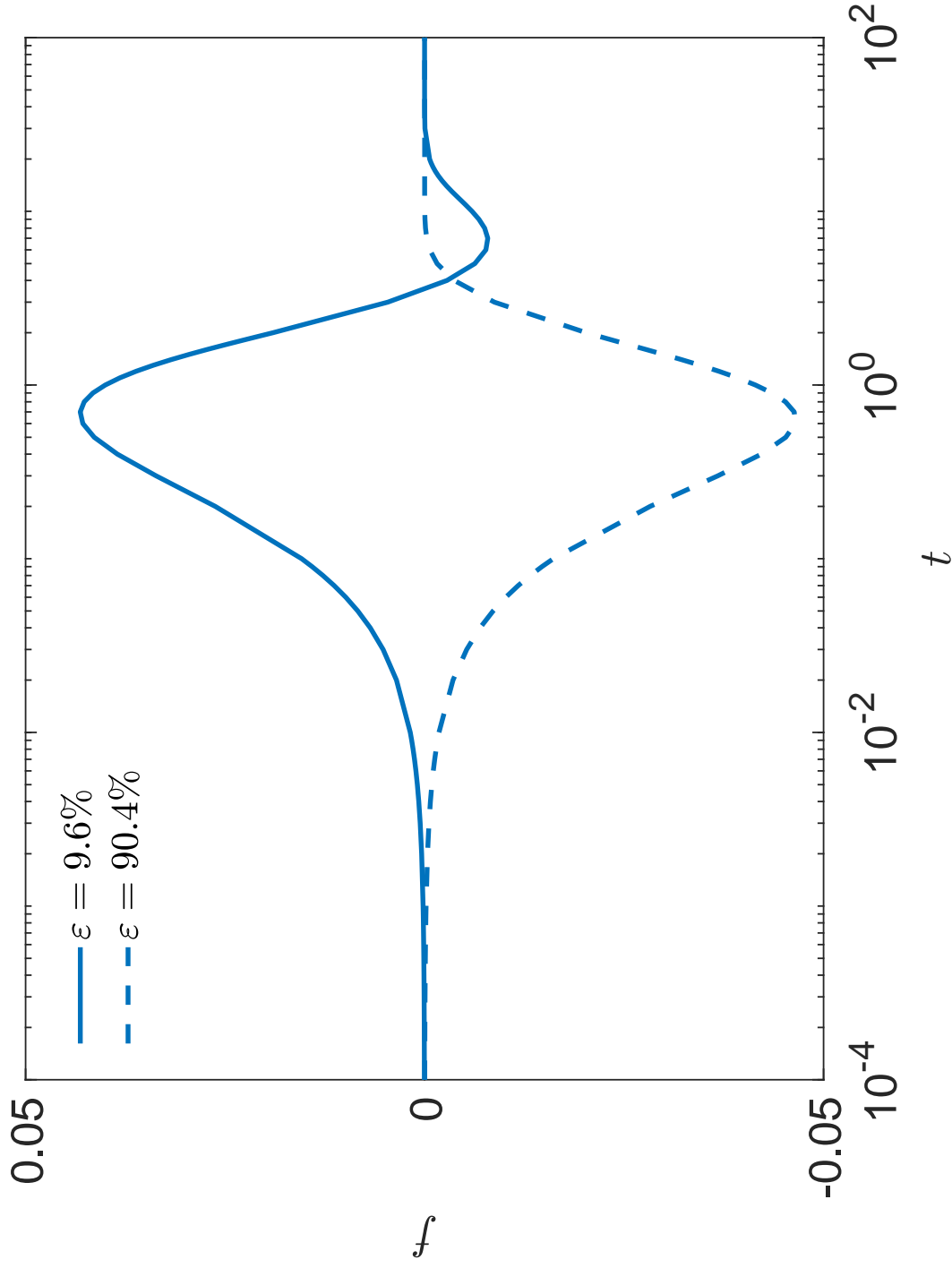
Fig. 3.8. **Temporal evolution of the bubble flattening for different initial surfactant coverages.** Comparing the Flattening f of the $\varepsilon = 9.6\%$ (solid blue line) and $\varepsilon = 90.4\%$ (dashed blue line) for $Re = 10^{-4}$, $Pe = 140$, and $Ma = 2$. Flattening is described as $f = 1 - (b/a)^2$, where a is the maximum bubble size in the axial direction and b is the maximum size in the radial direction.
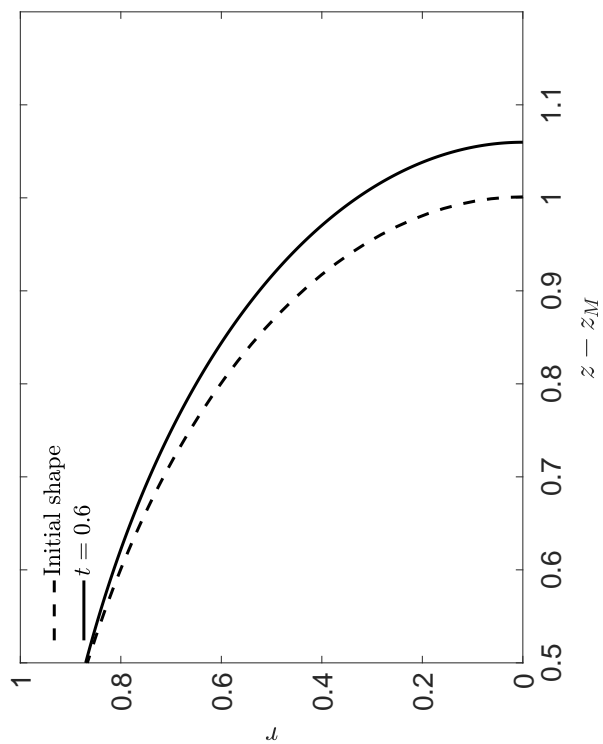
(a) $\varepsilon = 90.4\%$
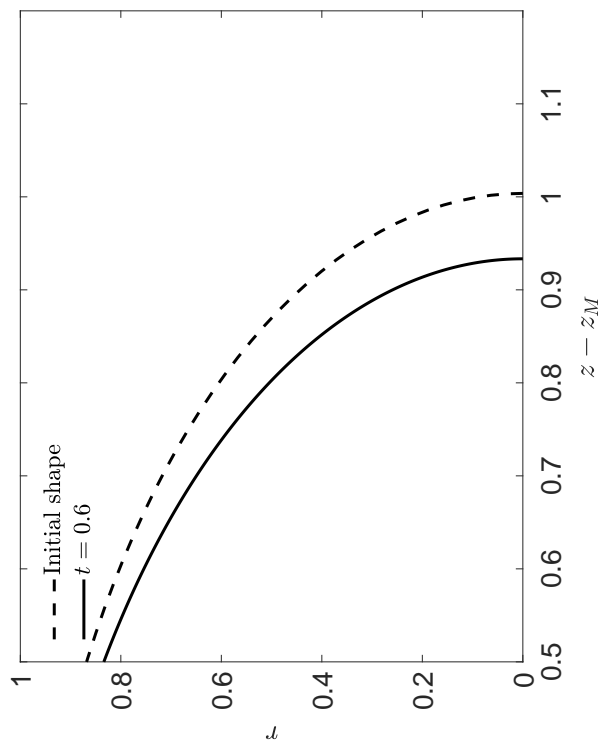
(b) $\varepsilon = 9.6\%$

Fig. 3.9. **Maximum deformation interface shapes of bubbles with different initial surfactant coverages.** Comparing the shapes of the maximum deformed bubble interface (solid black line) against the initial bubble interface (dashed black line) for a surfactant strength of $Ma = 2$, a Peclet of $Pe = 140$, and an outer-fluid viscosity of $Re = 10^{-4}$.
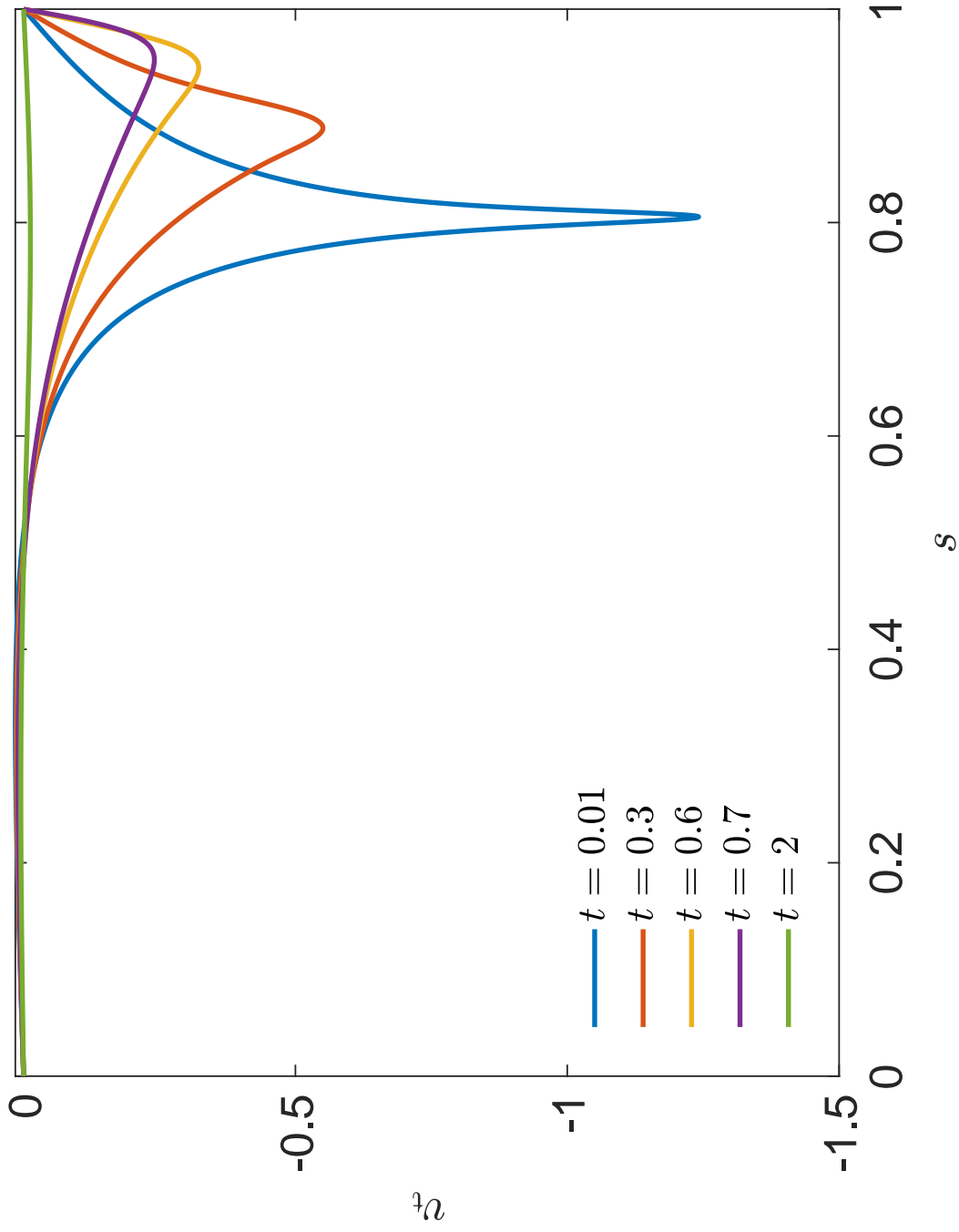
Fig. 3.10. **Temporal evolution of tangential velocities on the bubble interface.** Shows the tangential velocity v_t across the bubble normalized arc-length s at various times t for $\varepsilon = 90.4\%$, $Re = 10^{-4}$, $Pe = 140$, and $Ma = 2$.

(a) $\varepsilon = 90.4\%$, $t = 0.01$

(b) $\varepsilon = 90.4\%$, $t = 0.3$

(c) $\varepsilon = 90.4\%$, $t = 0.6$

(d) $\varepsilon = 90.4\%$, $t = 2$
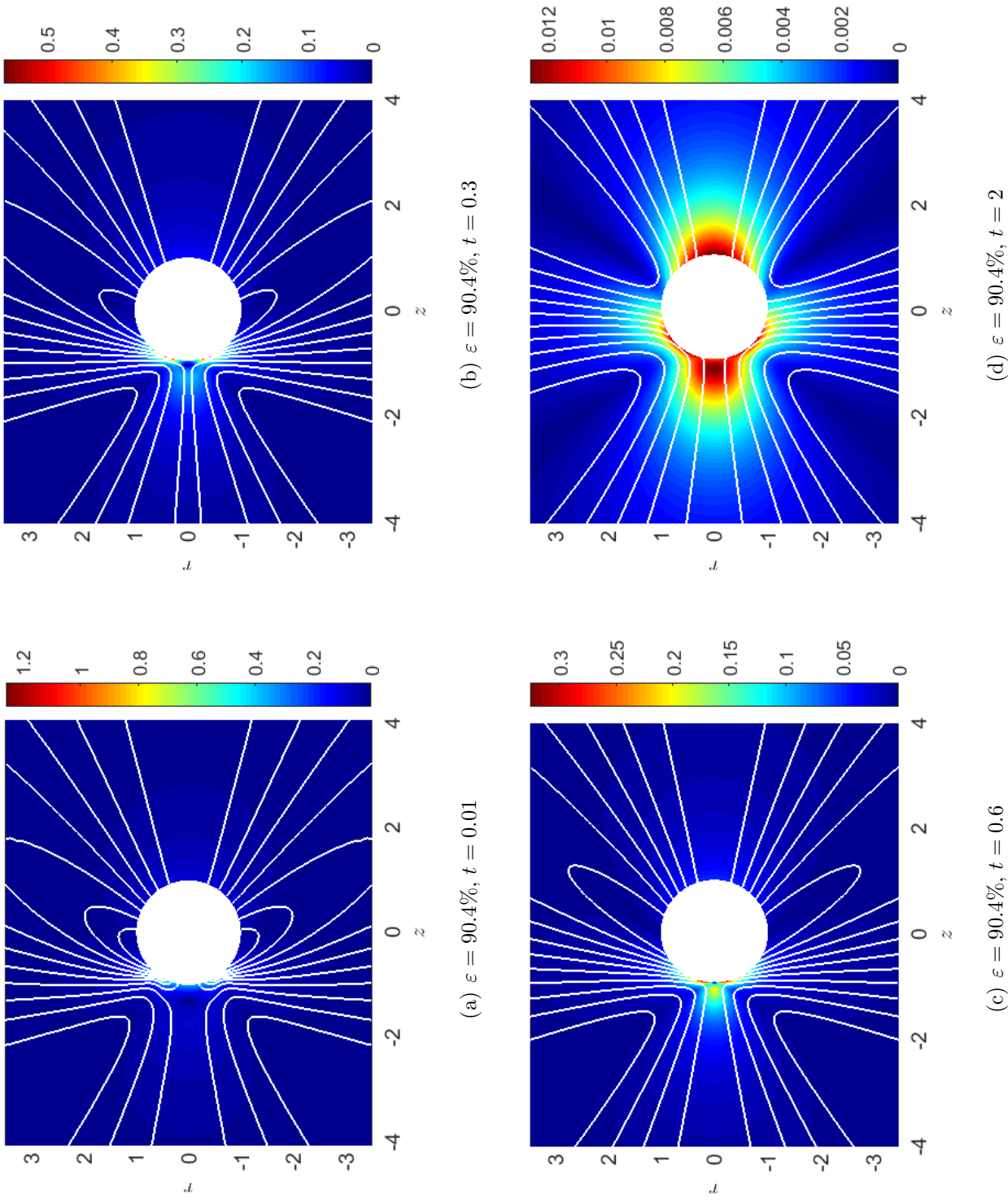
Fig. 3.11. **Temporal evolution of the velocity magnitude field and streamlines for the active bubble.** The evolution of the velocity magnitude $|V|$ of the outer viscous fluid over time. Time from early to later from (a) to (b) for $\varepsilon = 90.4\%$, $Re = 10^{-4}$, $Pe = 140$, and $Ma = 2$.
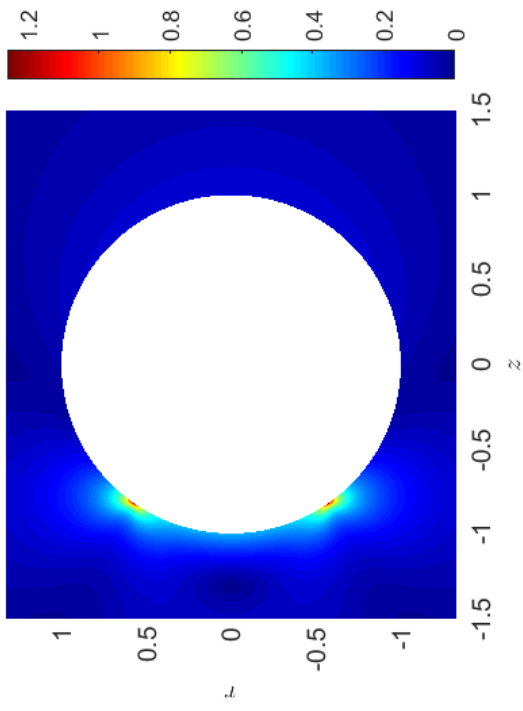
(a) $\varepsilon = 90.4\%$, $t = 0.01$
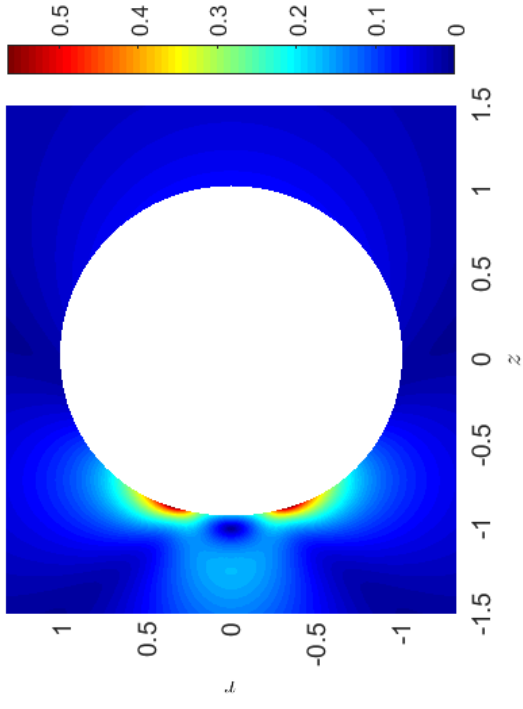
(b) $\varepsilon = 90.4\%$, $t = 0.3$
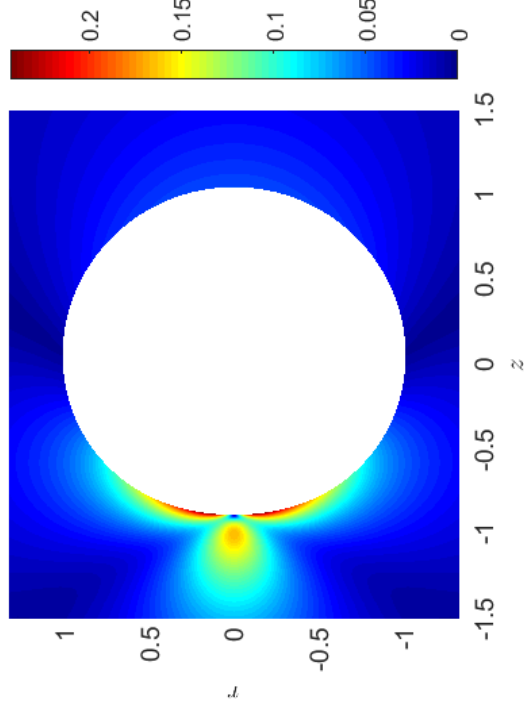
(c) $\varepsilon = 90.4\%$, $t = 0.6$
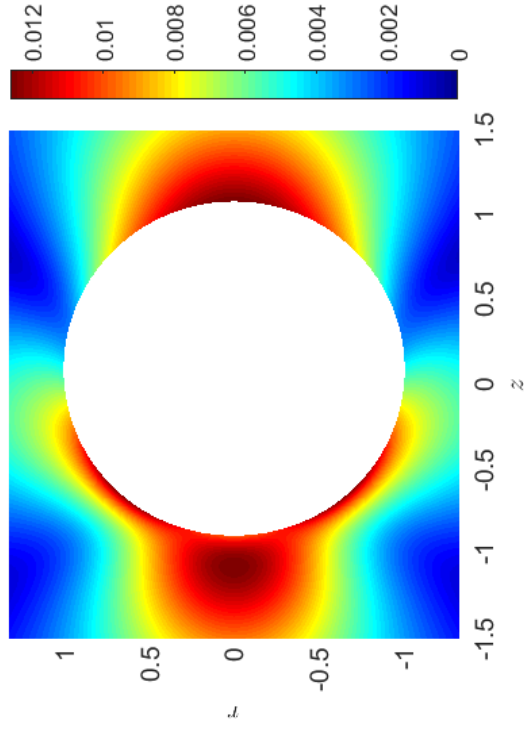
(d) $\varepsilon = 90.4\%$, $t = 2$

Fig. 3.12. **Temporal evolution of velocity magnitude field for the active bubble.** A magnified view of the evolution of velocity magnitude $|V|$ of the outer viscous fluid over time. Time from early to later from (a) to (b) for $\varepsilon = 90.4\%$, $Re = 10^{-4}$, $Pe = 140$, and $Ma = 2$.
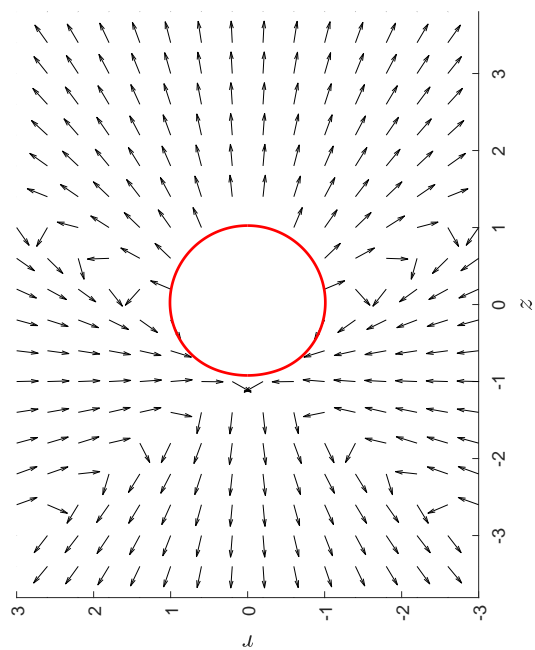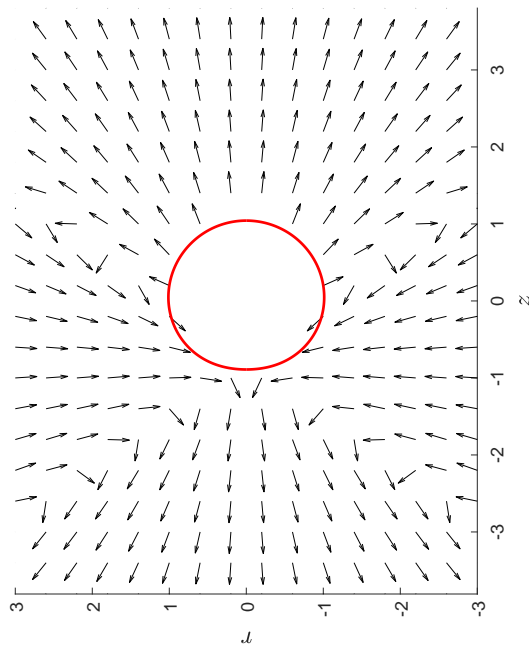
(a) $\varepsilon = 90.4\%$, $t = 0.01$

(b) $\varepsilon = 90.4\%$, $t = 0.3$

(c) $\varepsilon = 90.4\%$, $t = 0.6$
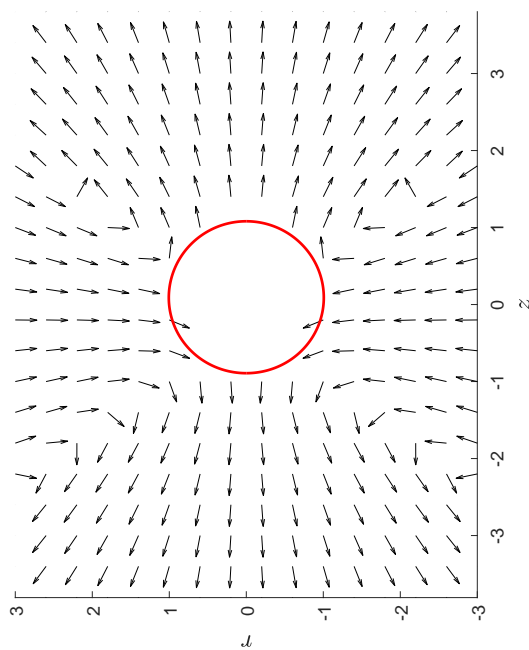
(d) $\varepsilon = 90.4\%$, $t = 2$

Fig. 3.13. **Temporal evolution of velocity arrow field for the active bubble.** The evolution of the velocity arrow field of the outer viscous fluid over time. Time from early to later from (a) to (b) for $\varepsilon = 90.4\%$, $Re = 10^{-4}$, $Pe = 140$, and $Ma = 2$.
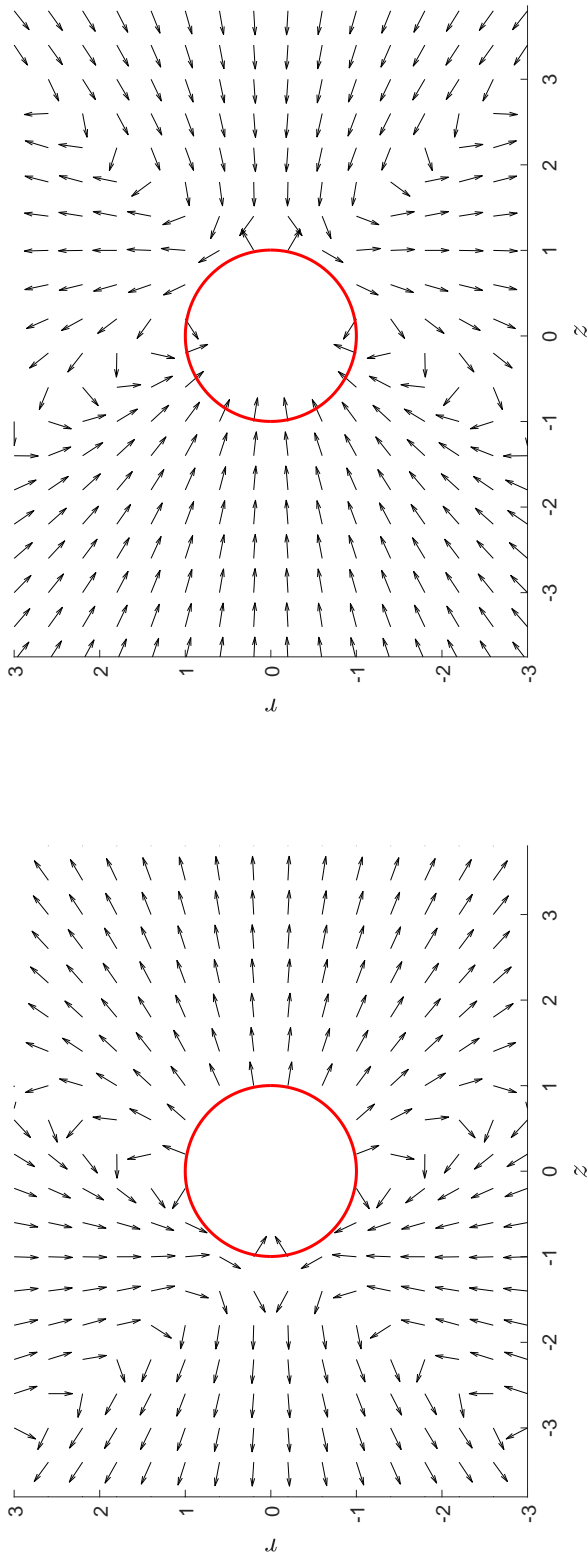
(a) $\varepsilon = 90.4\%$, $t = 0.01$

(b) $\varepsilon = 9.6\%$, $t = 0.01$

Fig. 3.14. **Initial hydrodynamic state bubble arrow field comparison for different initial surfactant coverages.** Compares a velocity arrow field for Left: $\varepsilon = 90.4\%$ at an early time as a pusher and Bottom: $\varepsilon = 9.6\%$ at an early time as a puller for bubbles with $Re = 10^{-4}$, $Pe = 140$, and $Ma = 2$
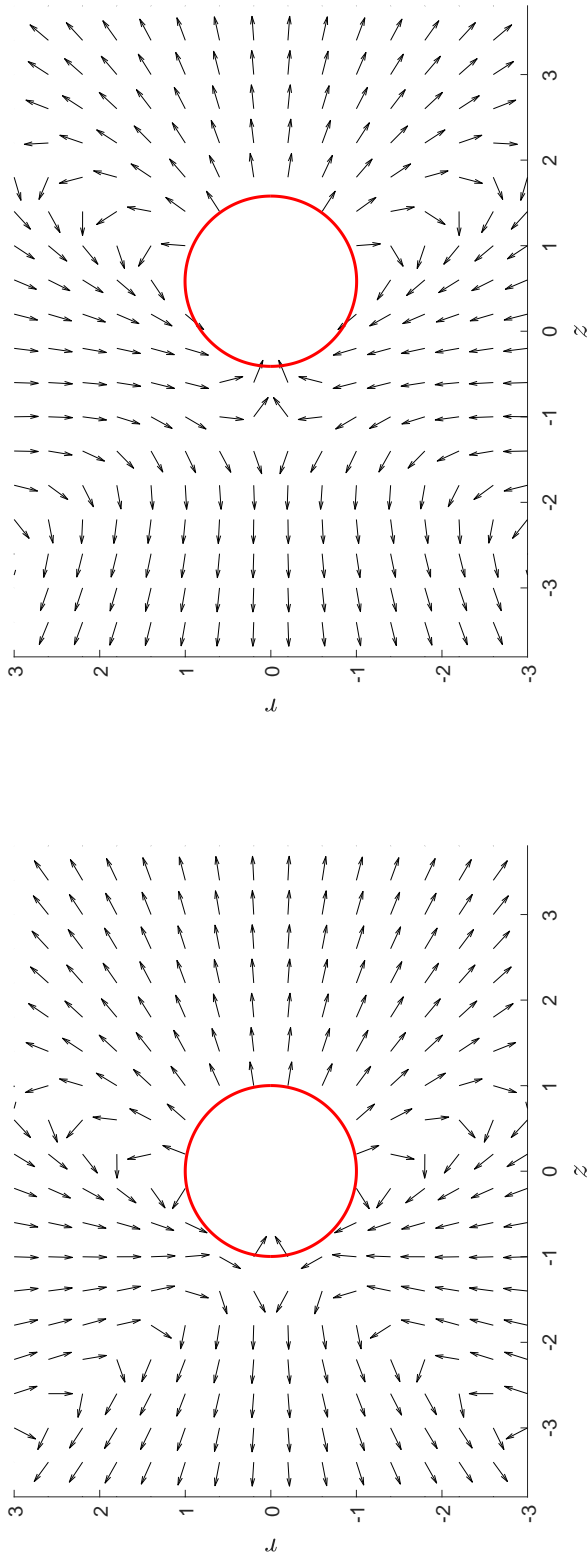
(a) $\varepsilon = 90.4\%$, $t = 0.01$

(b) $\varepsilon = 9.6\%$, $t = 6$

Fig. 3.15. **Similar hydrodynamic state bubble arrow field comparison for different initial sur-factant coverages.** Compares a velocity arrow field for Left: $\varepsilon = 90.4\%$ at an early time as a pusher and Right: $\varepsilon = 9.6\%$ at a late time as a pusher for bubbles with $Re = 10^{-4}$, $Pe = 140$, and $Ma = 2$

3.2.1 ε Parametric Study

As seen in the previous paragraphs, the initial surface coverage seems to have a strong influence on the maximum bubble displacement D. In order to have a better understanding of the influence of ε on the displacement of the bubble, a parametric study is performed and the results are shown in Figures 3.16 and 3.17 where the coverage ϵ is represented as a fraction of interface coated by surfactant instead of percentage with $\epsilon = 1$ indicating a bubble initially coated completely with surfactant.

Figure 3.16 shows that, generally the distance traveled by the bubble D increases with the fraction of uncovered surface $(1 - \epsilon)$ except when reaching the limit of completely clean surface, where D drops abruptly to zero. As the initial area of clean surface increases , the total displacement D curve detaches from the linear relationship of $D = 1 - \epsilon$ where it reaches a maximum and decreases toward the limit of an uncontaminated bubble $\epsilon = 0$ where $D = 0$.

Figure 3.17 shows the overall time T (defined as the time spent to travel 90% of the total distance D) and the average speed U (defined as $U \equiv D/T$) as a function of the extent of the contaminated section ε, for $Ma = 2$. Results show that ε has a strong effect on both T and U. The figure makes it clear that small contaminated areas generate faster motions and larger displacements.
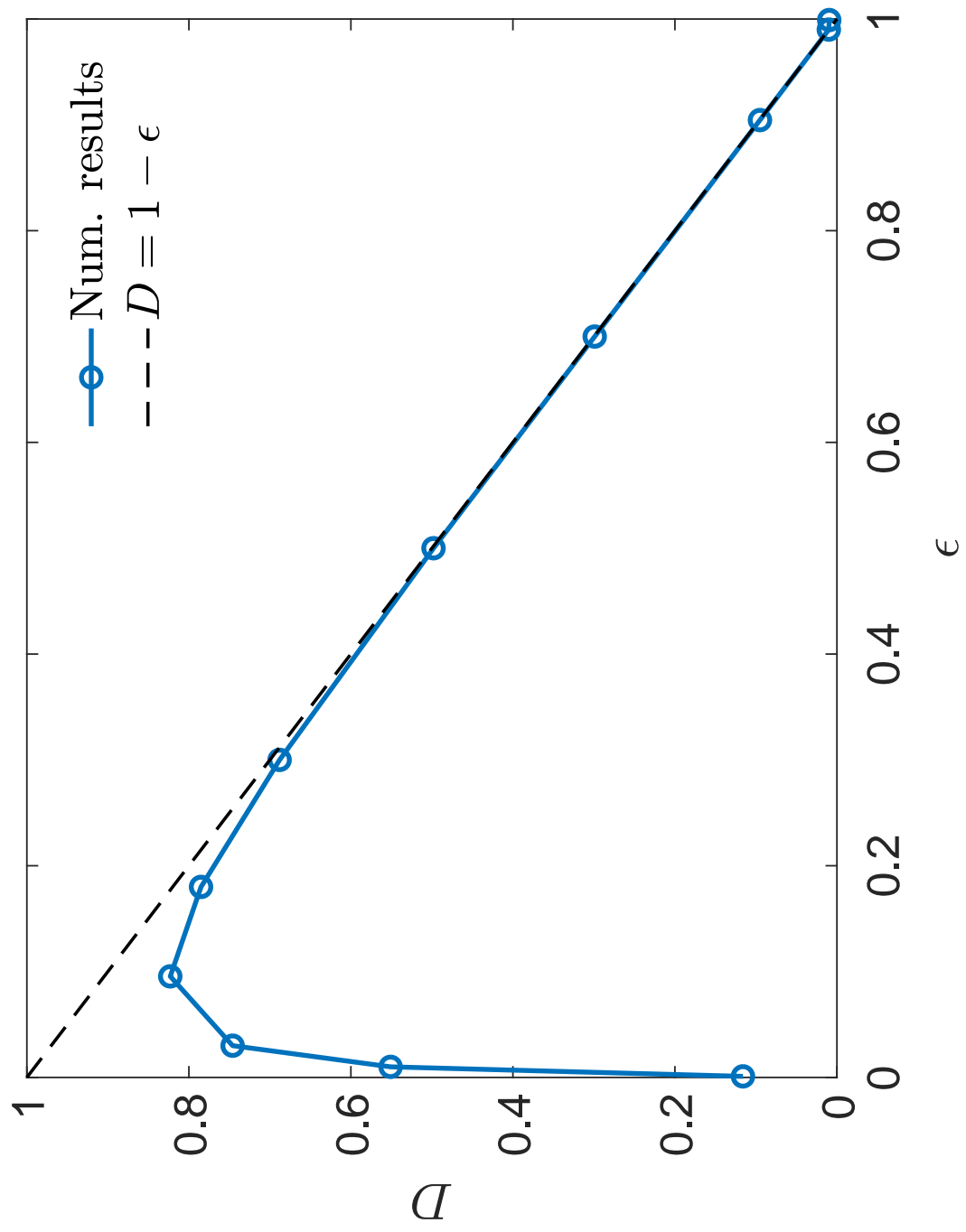
Fig. 3.16. **Influence of initial surfactant coverage on total bubble displacement.** A Parametric plot showing final bubble displacement D at various surfactant coverages ε. With a power law scaling of $D = 1 - \epsilon$ for bubbles with $Re = 10^{-4}$, $Pe = 140$, and $Ma = 2$
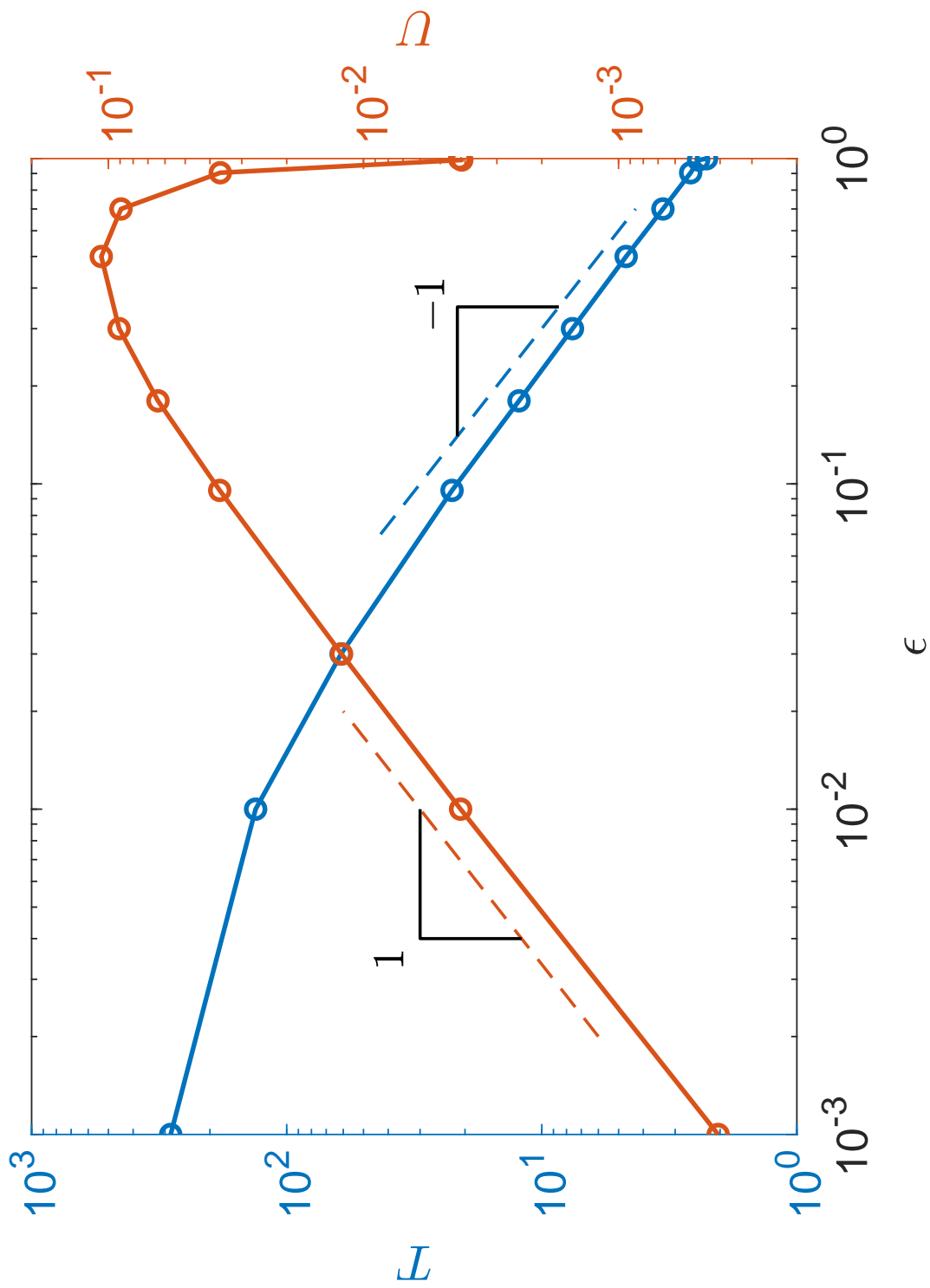
Fig. 3.17. **Influence of initial surfactant coverage on average bubble velocity and time of bubble movement.** A Parametric plot showing the average bubble velocity U (orange) and time to reach D ,T, (blue) at various surfactant coverages ϵ. With a power law scaling of 1 for U and -1 for T for bubbles with $Re = 10^{-4}$, $Pe = 140$, and $Ma = 2$

3.3 Influence of Marangoni Number Ma on Bubble Propulsion

This section describes the influence of a large Marangoni number Ma on the active motion of the small bubble. First, a thorough comparison between the case discussed in Chapter 2 with $Ma = 2$ and a case with a larger Marangoni number, $Ma = 20$ is performed. Both cases will have all other initial conditions remain the same with an initial coverage of $\varepsilon = 9.6\%$ ($\alpha = 0.2$) and a Peclet of $Pe = 140$, with the outer fluid having a high viscosity $Re = 10^{-4}$. This study will allow a more thorough understanding of the effect that stronger Marangoni flows have on the propulsion of an object as previously studied by [47]. Varying concentrations and varieties of chemically active species can alter the Marangoni impact.

The bubble with a larger Marangoni influence behaves very similar to the bubble with the lesser Marangoni effect studied in Chapter 2. The overall macroscopic hydrodynamic regimes of the Marangoni movement is very similar between these two cases for the duration of propulsion. The displacement d of the bubble center of mass z_M for $Ma = 2$ (solid orange line) and $Ma = 20$ (solid blue line) is seen in Figure 3.18 depicting displacement d versus time t shows a very similar trend in overall bubble movement. The bubble with $Ma = 20$ initiates movement at $t \approx 10^{-3}$ and the $Ma = 2$ bubble begins to move about a decade later at $t \approx 0.01$. The speed v of the bubble centers of mass v_M, seen in Figure 3.19 depicting velocity v versus time t, is very similar with the $Ma = 2$ bubble (solid orange line) slowing to a stop at $t \approx 10$ whereas $Ma = 20$ slows to a stop at $t \approx 1$ roughly a decade earlier. One of the more apparent differences seen when comparing the bubble center of mass speed is the velocity peak for $Ma = 20$ (solid blue line) at $t \approx 0.05$.

This peak is explained in Figure 3.20 where the front and back end velocities of the bubble are tracked over time. In this plot at $t \approx 0.05$, the $Ma = 20$ front end velocity v_F (solid blue line) is shown decreasing while the back end velocity v_B is increasing as the bubble approaches its maximum flattening f. This relationship between the center of mass velocity v_M peak for $Ma = 20$ and the peak bubble flattening, f shown
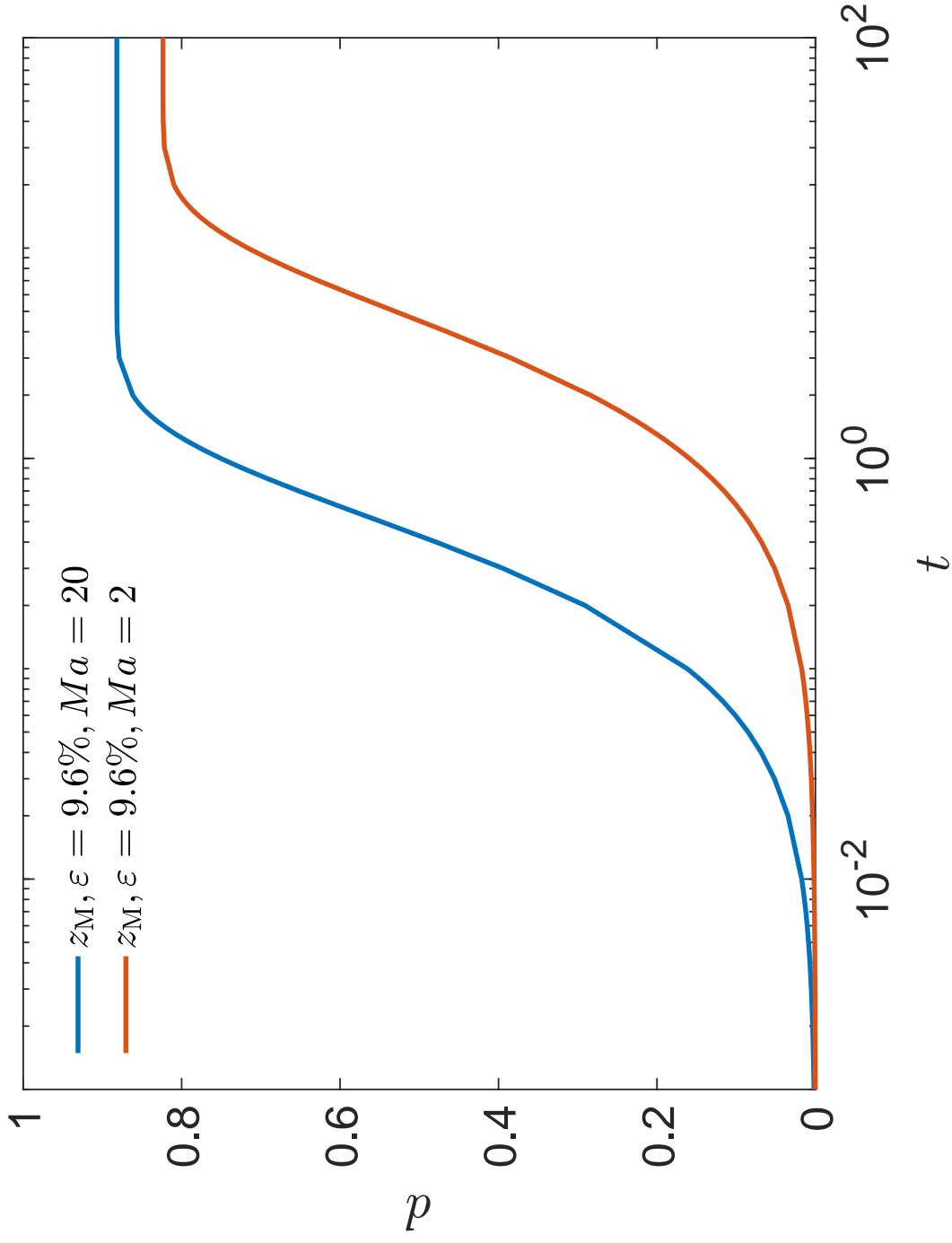
Fig. 3.18. **Temporal evolution of the bubble center of mass displacement for different surfactant strengths.** Comparing the displacement d of the center of mass z_M over time t of $Ma = 20$ (solid blue line) and $Ma = 2$ (solid orange line) for $\varepsilon = 9.6\%$, $Pe = 140$, and $Re = 10^{-4}$.
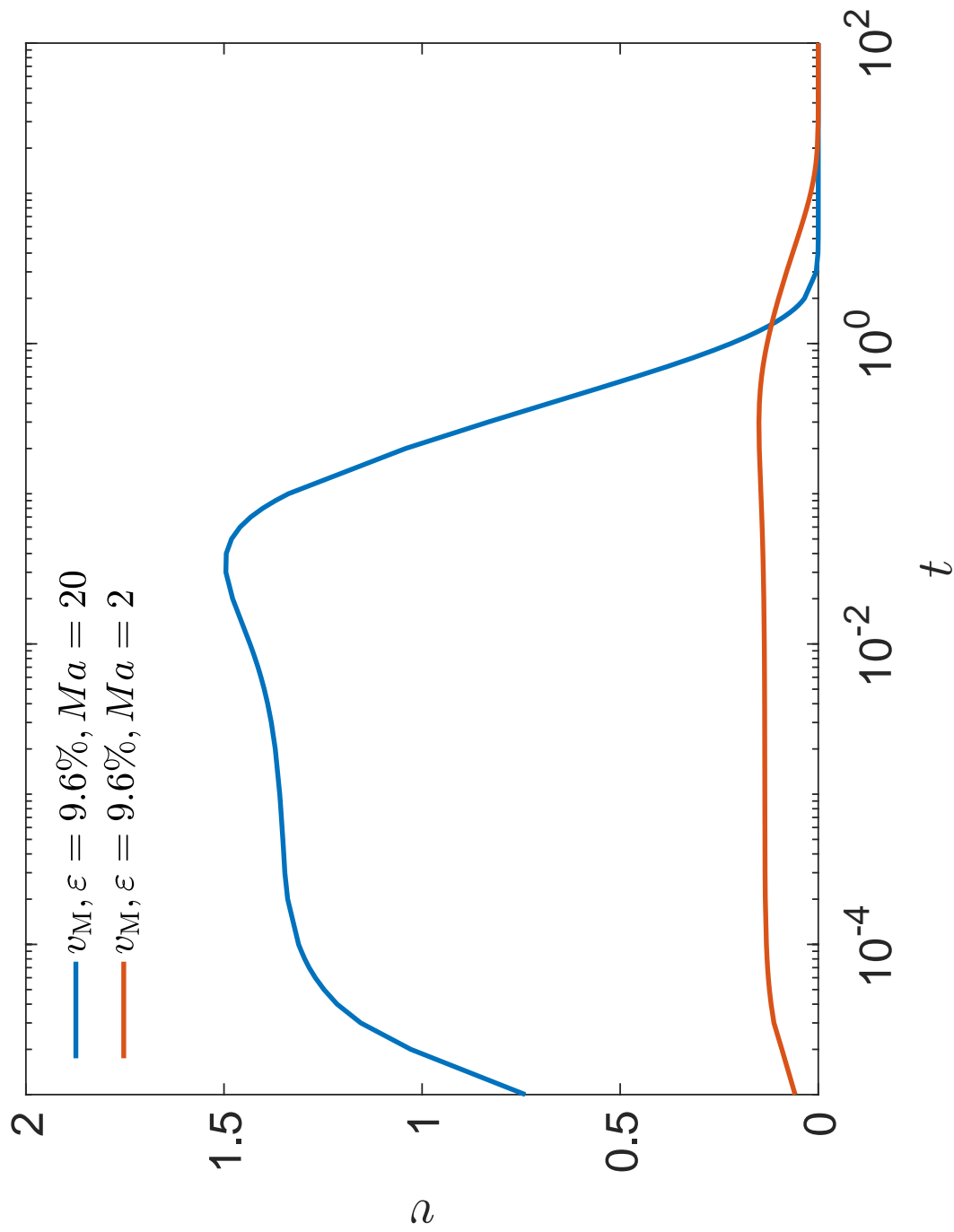
Fig. 3.19. **Temporal evolution of the bubble center of mass velocity for different surfactant strengths.** Comparing the velocity v of the center of mass v_M over time t of $Ma = 20$ (solid blue line) and $Ma = 2$ (solid orange line) for $\varepsilon = 9.6\%$, $Pe = 140$, and $Re = 10^{-4}$.
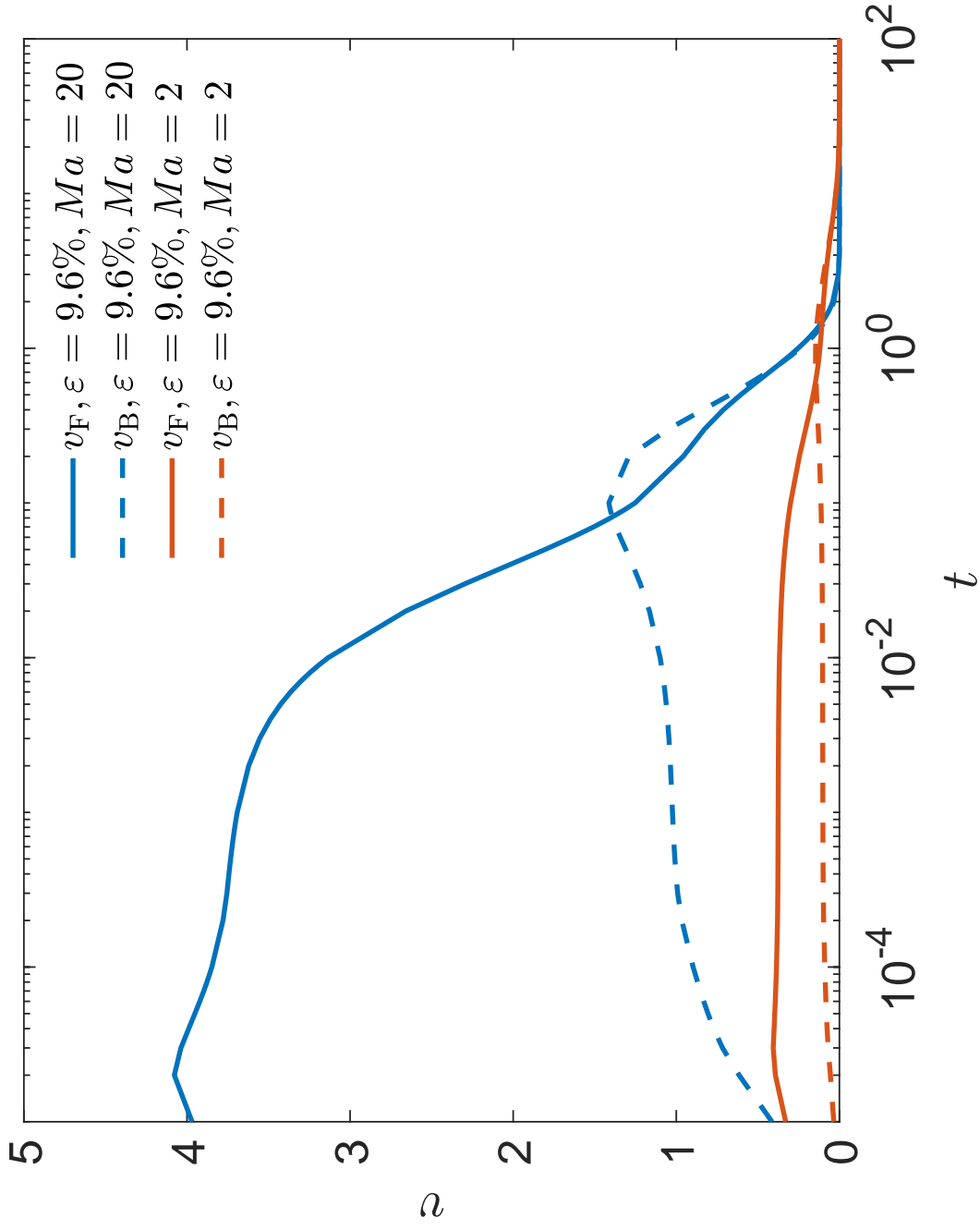
Fig. 3.20. **Temporal evolution of the bubble front and back end velocities for different surfactant strengths.** Comparing the velocity v of the bubble front v_F (solid line) and back v_B (dashed line) end over time t of $Ma = 20$ (blue) and $Ma = 2$ (orange) for $\varepsilon = 9.6\%$, $Pe = 140$, and $Re = 10^{-4}$.

in Figure 3.21 for $Ma = 20$ (solid blue line) explains that as the bubble approaches the maximum flattening peak, the combined movement of both front and back ends of the bubble generate a slight v_M spike.

Displacement of the front and back ends of the bubbles in Figure 3.22 closely match for the different Marangoni strengths,but are disconnected by a time factor of 10. Both the front ends of the different bubbles, with different Ma, moving first initially (solid lines) with the back ends (dashed lines) showing a delayed movement resulting in bubble elongation. The maximum flattening for $Ma = 2$ is approximately 25% of the max flattening for the $Ma = 20$ bubble shown in Figure 3.21. The interface shape at the time of maximum flattening for both cases, shown in Figure 3.23, is compared with the initial bubble interface shape. Larger Marangoni stresses result in greater deformation of the bubble interface, as well as a faster propulsion of the bubble. The earlier propulsion of the $Ma = 20$ bubble is supported by the earlier maximum flattening of the interface seen in Figure 3.23 (b) occurring at $t \approx 0.09$, whereas the $Ma = 2$ bubble experiences maximum flattening of the interface at a later time $t \approx 0.6$ (Figure 3.23 (a)). This is due to the surfactant migrating across the interface more quickly with the $Ma = 20$ bubble compared to the $Ma = 2$ bubble supported by Figure 3.24 in which the concentration γ on the interface is very similar between the two cases despite differing from a factor of 10 when comparing (a) and (b). The tangential velocity v_t generated by this surfactant front shown in Figure 3.25 supports the quicker moving Marangoni front where v_t is shown for similar locations of the concentration fronts of the $Ma = 2$ (a) and $Ma = 20$ (b) bubbles. The $Ma = 20$ bubble displays a much larger tangential velocity compared to $Ma = 2$ at these similar surfactant front locations (by a factor of 10).

The similarities between the two cases are also shown in the velocity magnitude $| V |$ field of the outer-fluid at three different times for each case shown in Figure 3.26. The streamlines are nearly identical for the instances shown, despite the similar hydrodynamic effects occurring a decade of time earlier for $Ma = 20$. The figure also

shows nearly identical velocity magnitude fields, where the contour that represents the velocity color gradient is decreased by a factor of 10 for $Ma = 2$.

Figure 3.27 shows an extremely similar hydrodynamic transition from pusher to puller for the $Ma = 20$ and $Ma = 2$ bubbles using the bulk fluid arrow field. This figure compares the macroscopic flows for $Ma = 2$ and $Ma = 20$ where arrow fields are compared when the surfactant front is at similar locations across the bubbles normalized arc-length. As previously discussed, the movement of the surfactant front occurs a decade of time earlier for $Ma = 20$ compared to the $Ma = 2$ bubble. Both Marangnoi cases are seen in the puller state at early times where the bulk fluid is pulled inward on the axis of propulsion from both in front of and behind the bubble for Figure 3.27 (a) and (d). Then in Figure 3.27 (b) and (e) both cases are seen transitioning from puller to pusher as the surfactant front is crossing the midpoint of both bubbles ($s \approx 0.5$). Lastly, the bubbles remain in their final hydrodynamic pushing state Figure 3.27 (c) and (f), where the outer-fluid being pushed away from in front and behind the bubble on the axis of propulsion, until the movement of the bubble ceases.
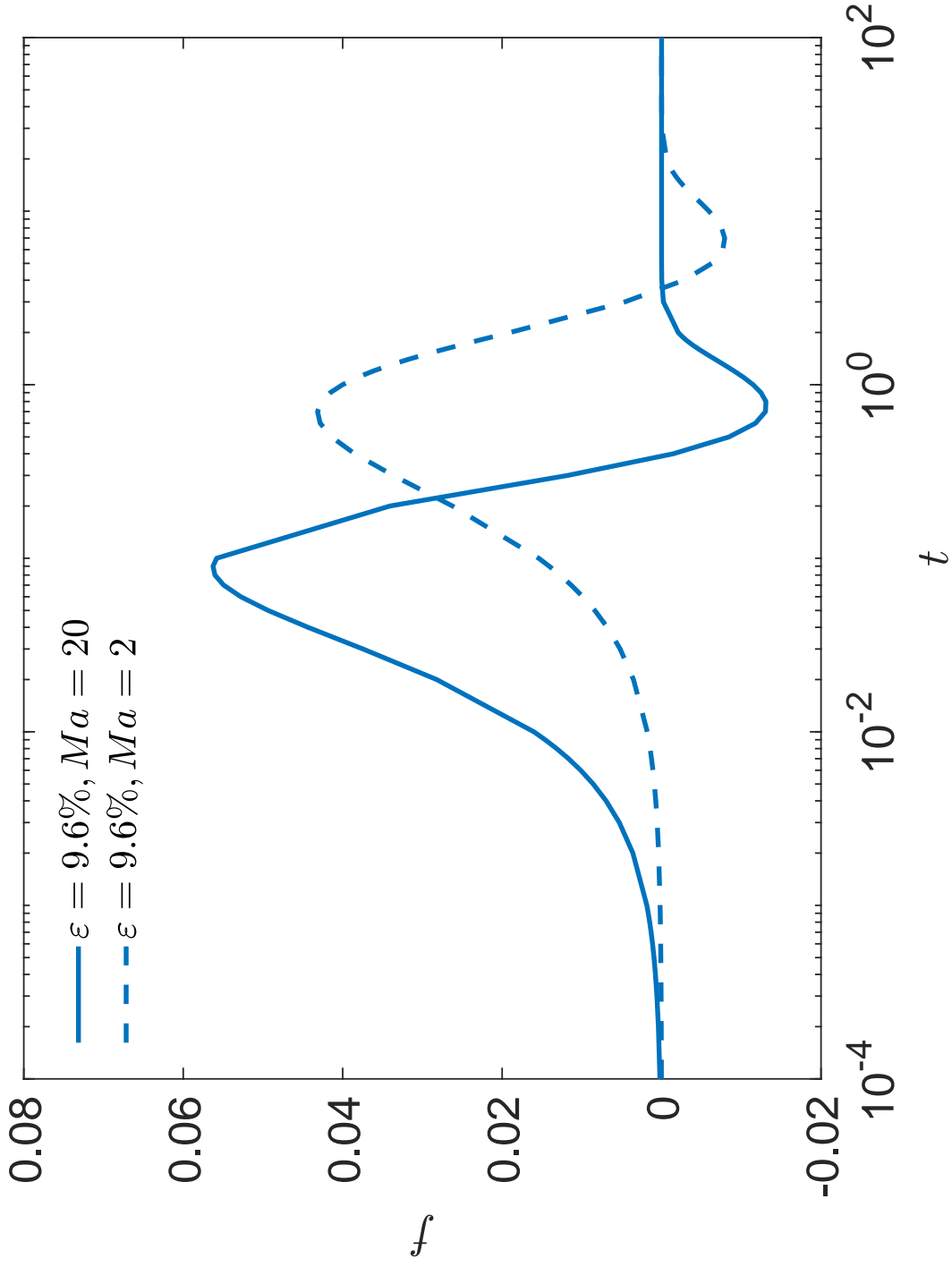
Fig. 3.21. **Temporal evolution of the bubble flattening of different surfactant strengths.** Comparing the flattening f over time t of the $Ma = 20$ (solid blue line) and $Ma = 2$ (dashed blue line) for $\varepsilon = 9.6\%$, $Pe = 140$, and $Re = 10^{-4}$. Flattening is described as $f = 1 - (b/a)^2$, where (a) is the maximum bubble size in the axial direction and (b) is the maximum size in the radial direction.
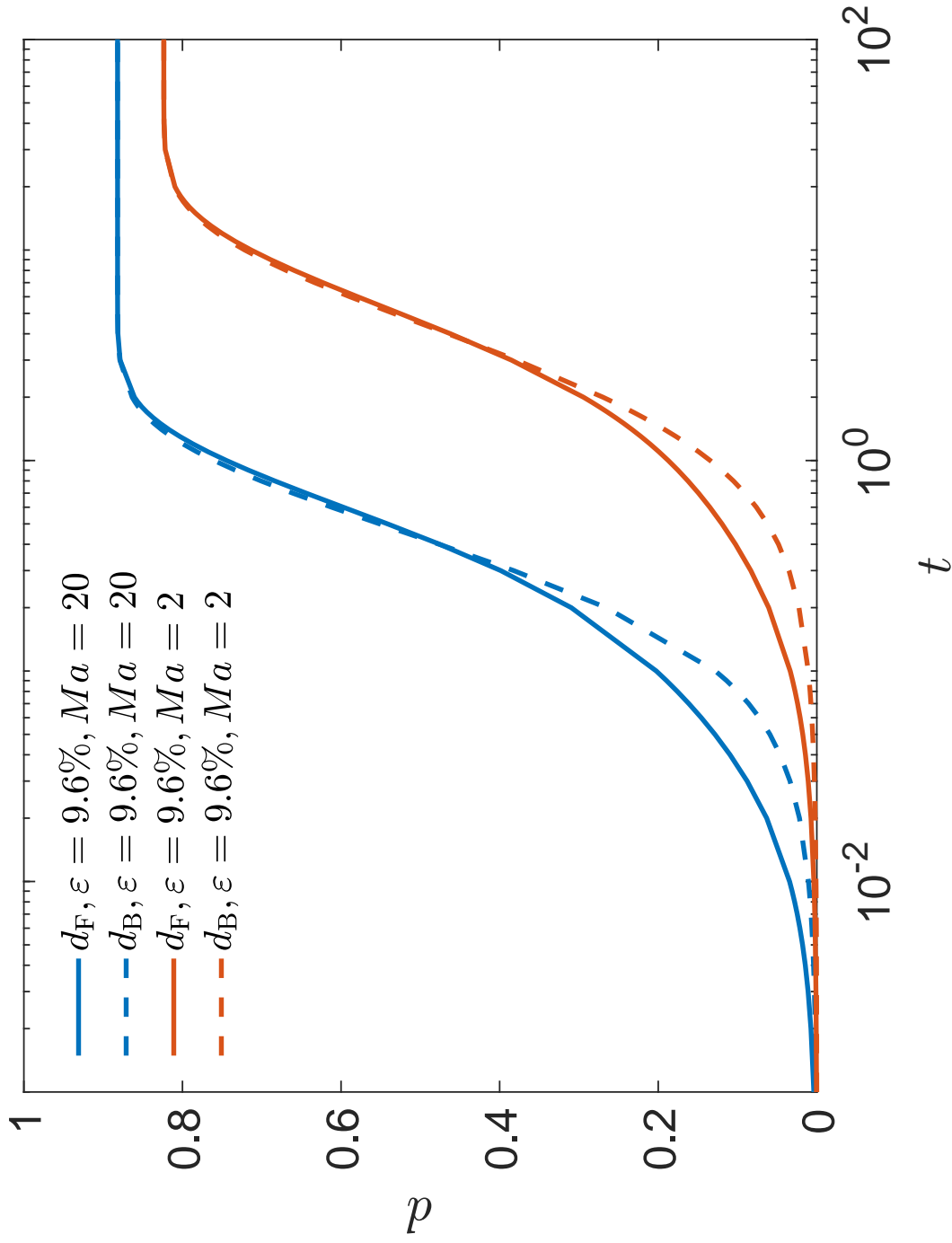
Fig. 3.22. **Temporal evolution of the bubble front and back end displacements for different surfactant strengths.** Comparing the displacement (d) of the bubble front d_F (solid line) and back d_B (dashed line) end over time t of $Ma = 20$ (blue) and $Ma = 2$ (orange) for $\varepsilon = 9.6\%$, $Pe = 140$, and $Re = 10^{-4}$.
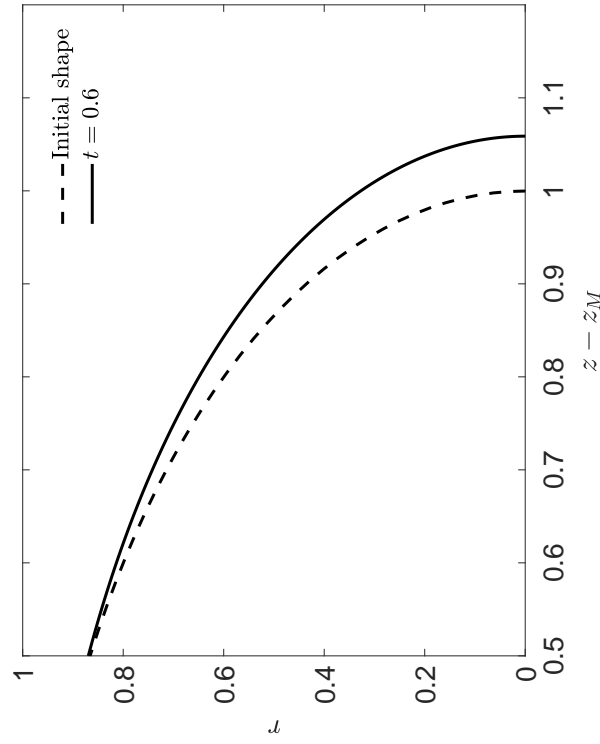
(a) $Ma = 2$
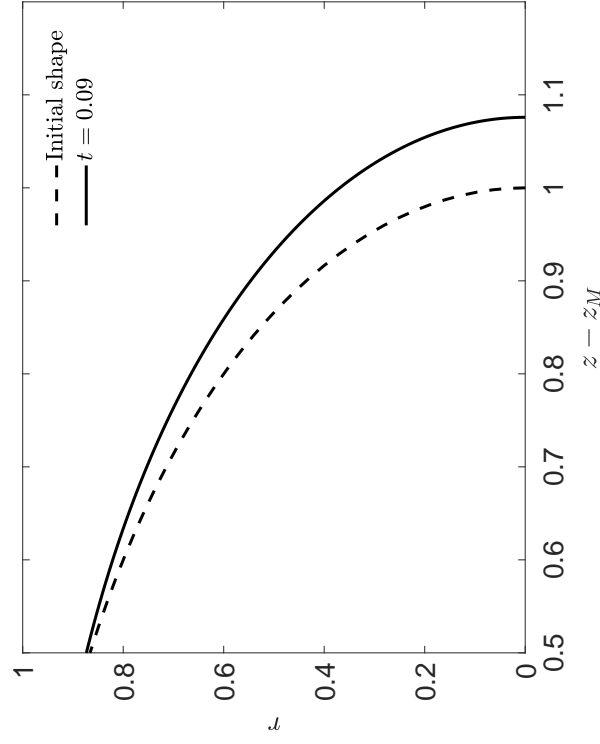
(b) $Ma = 20$

Fig. 3.23. **Maximum deformation interface shapes of bubbles with different surfactant strengths.** Comparing the maximum deformed interface shape (solid black line) against the initial bubble interface shape (dashed black line) for $\varepsilon = 9.6\%$, $Pe = 140$, and $Re = 10^{-4}$.
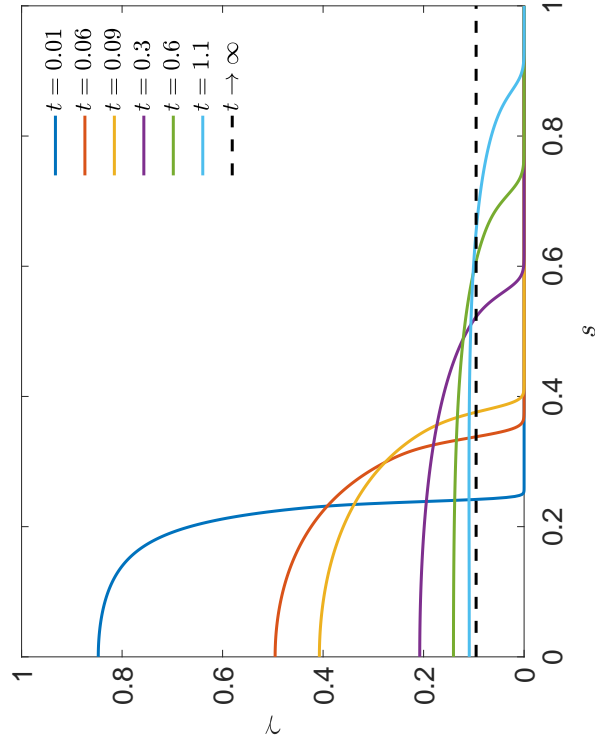
(a) $Ma = 2$
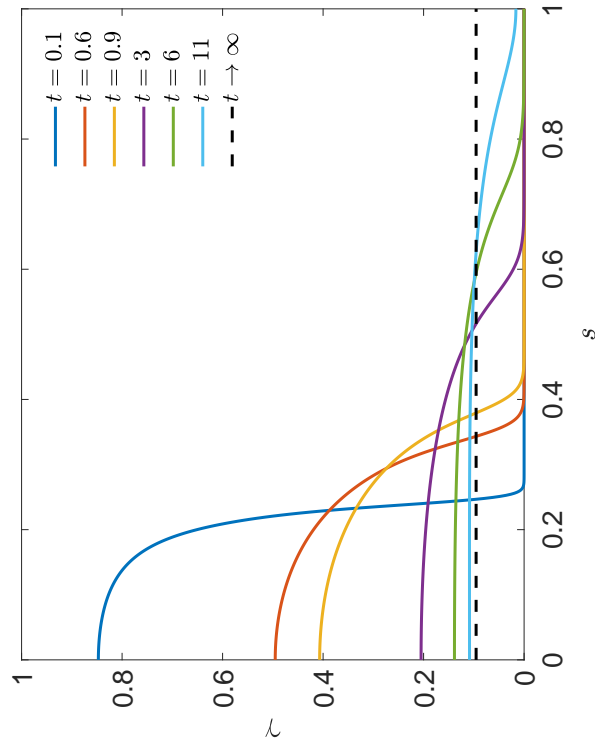
(b) $Ma = 20$

Fig. 3.24. **Influence of surfactant strength on the evolution of the concentration profiles on the bubble interface.** Comparing the surfactant concentration γ across the bubble length s at various times with similar γ profiles for $\varepsilon = 9.6\%$, $Pe = 140$, and $Re = 10^{-4}$.
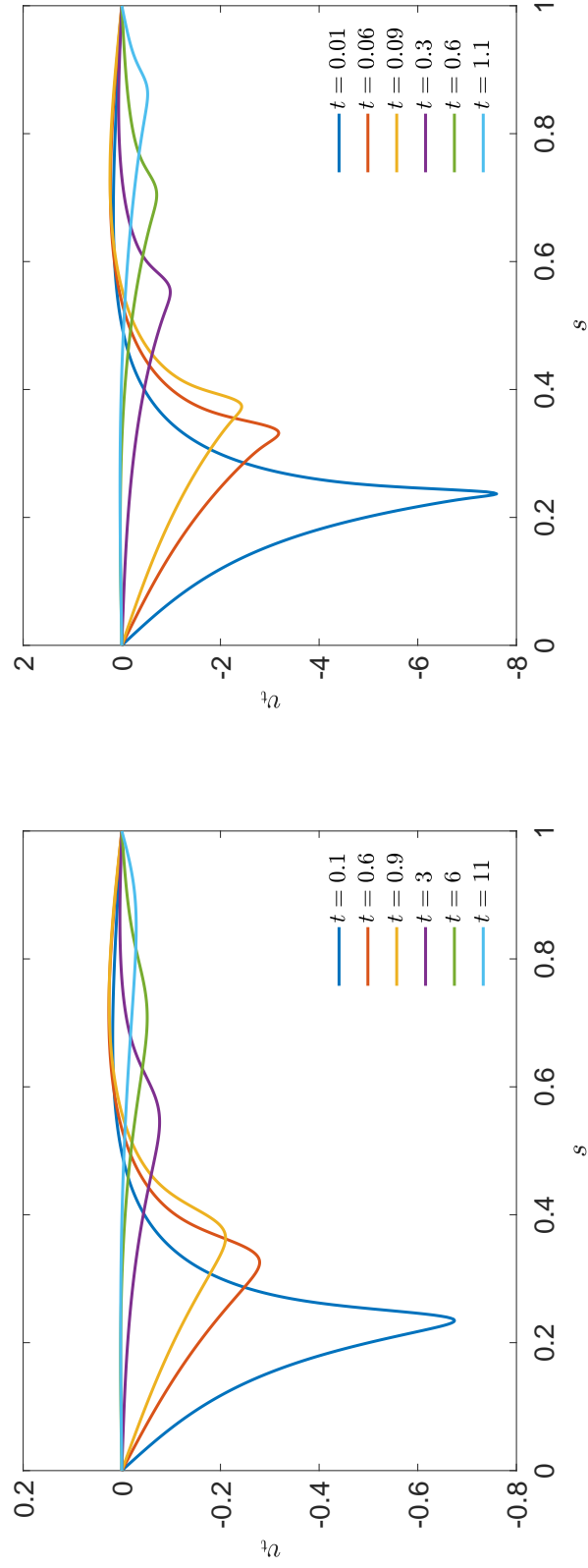
(a) $Ma = 2$

(b) $Ma = 20$

Fig. 3.25. **Influence of surfactant strength on the evolution of the tangential velocity profiles on the bubble interface.** Comparing the tangential velocity v_t across the bubble length s at various times with similar v_t profiles for $\varepsilon = 9.6\%$, $Pe = 140$, and $Re = 10^{-4}$.
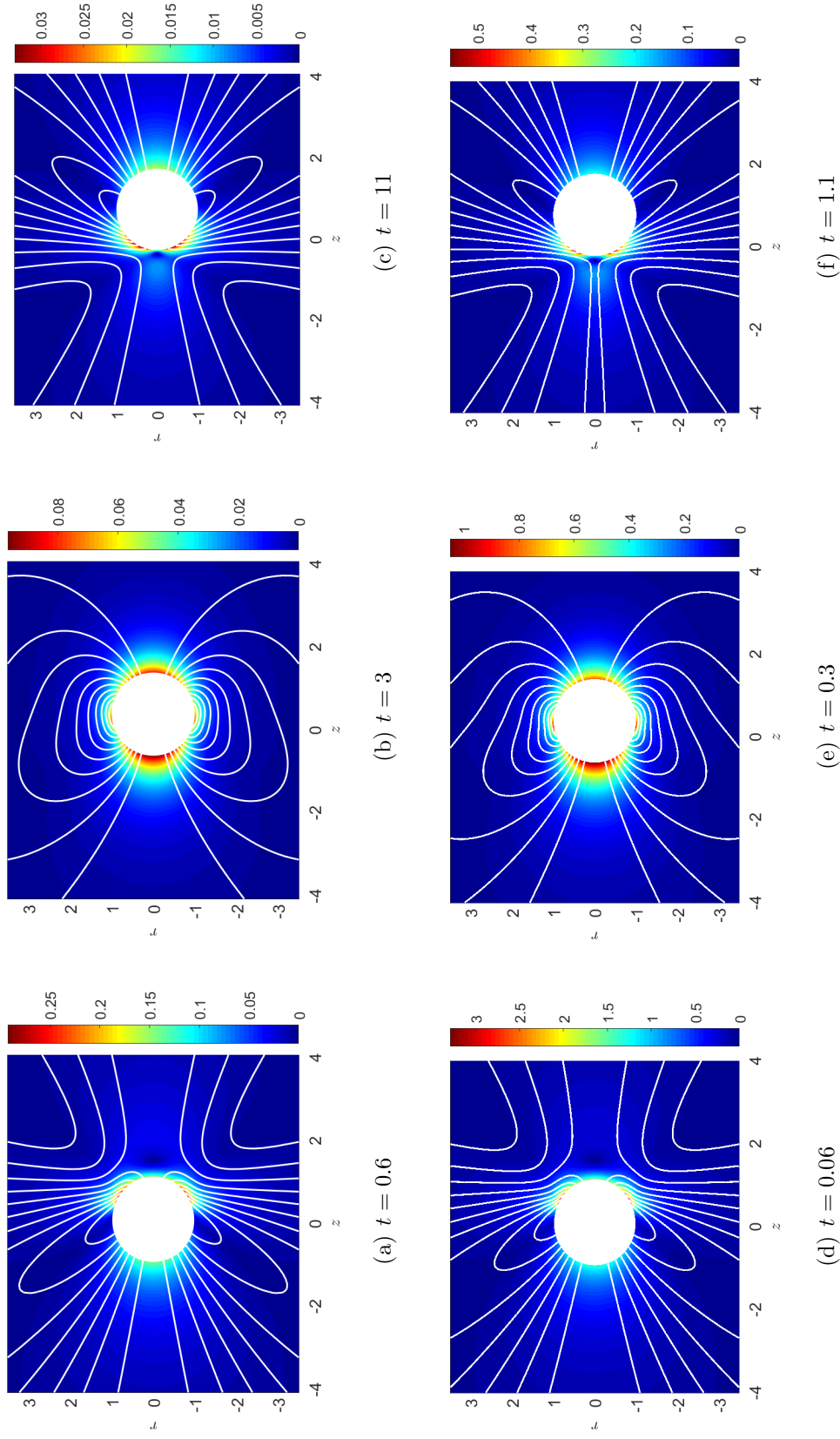
Fig. 3.26. **Influence of surfactant strength on the temporal evolution of the velocity magnitude field and streamlines for the active bubble.** The evolution of the velocity magnitude $|V|$ of the outer viscous fluid over time, along with streamlines. Earliest time shown starting from the left, with the latest time shown on the right with Top: $Ma = 2$ and Bottom: $Ma = 20$, $\varepsilon = 9.6\%$ and $Re = 10^{-4}$

(a) $Ma = 2$, $t = 0.6$

(b) $Ma = 2$, $t = 3$

(c) $Ma = 2$, $t = 11$

(d) $Ma = 20$, $t = 0.06$

(e) $Ma = 20$, $t = 0.3$

(f) $Ma = 20$, $t = 1.1$
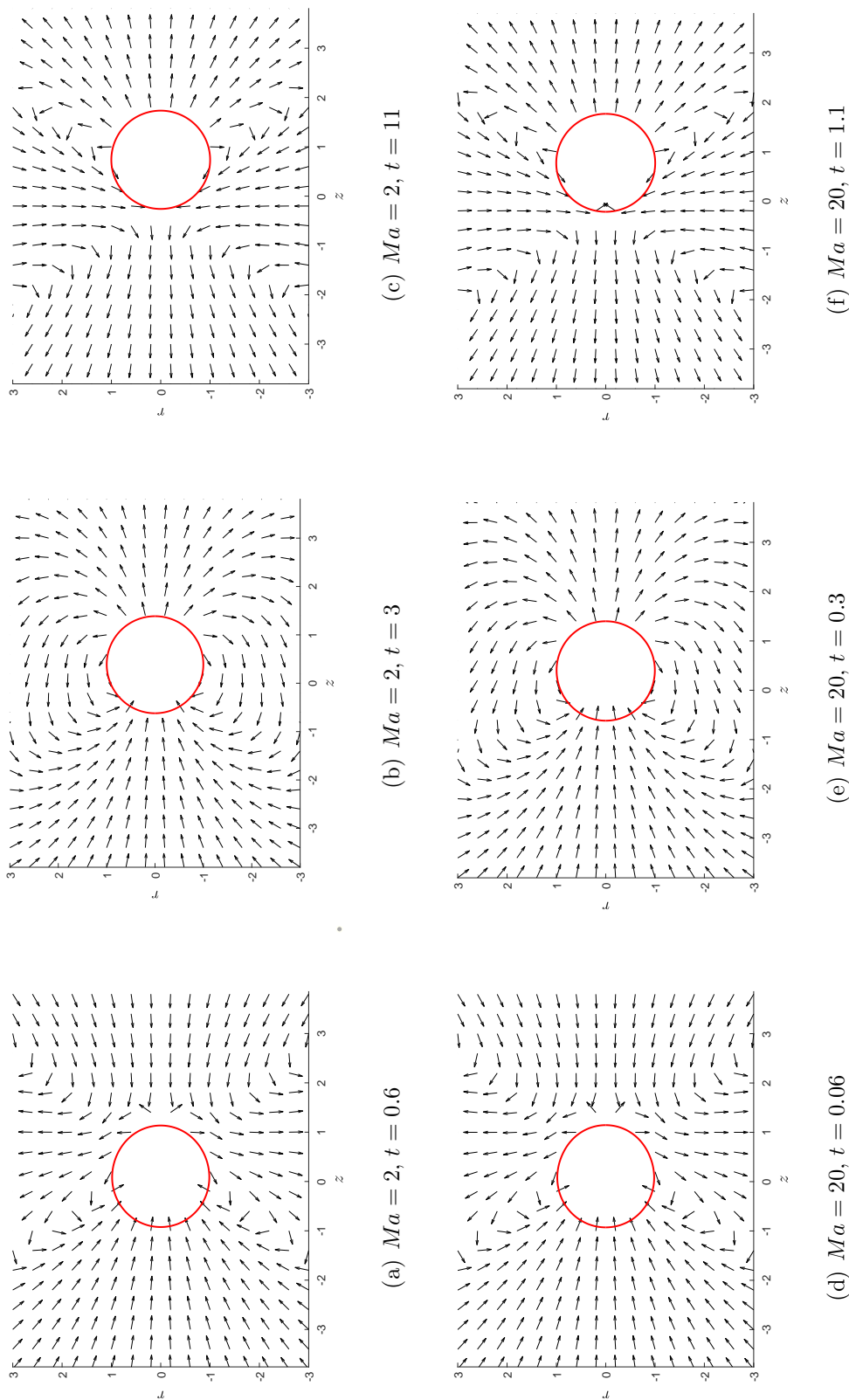
Fig. 3.27. **Influence of surfactant strength on the temporal evolution of the velocity arrow field for the active bubble.** The evolution of the velocity arrow field of the outer viscous fluid over time. Earliest time shown starting from the left, with the latest time shown at the right with Top: $Ma = 2$ and Bottom: $Ma = 20$, $\varepsilon = 9.6\%$, $Pe = 140$, and $Re = 10^{-4}$.

3.3.1 Ma **Parametric Study**

The previous section showed how the surfactant strength has a large influence on the average bubble velocity U and the final bubble displacement D. To have a comprehensive understanding of the impact of Ma on bubble displacement a parametric study was performed where results are shown in Figures 3.28, 3.29, and 3.30 with the coverage ε depicted as a fraction of coverage ϵ and not a percentage.

Figure 3.28 shows that the distance traveled by the bubble D

$$D \equiv \lim_{t \to \infty} z_M(t), \tag{3.2}$$

increases with the fraction of uncovered surface $(1-\epsilon)$, except when reaching the limit of clean surface where $D = 0$. Here, the surface activity (Ma) was evaluated for three values of the Marangoni number: $Ma = 0.2$ (weak surfactant), $Ma = 2$ (moderate surfactant). and $Ma = 20$ (strong surfactant). The maximum displacement, shown by $D = 1 - \epsilon$, increases and arises at smaller initial surfactant coverages as Ma increases. In fact, results of Figure 3.28 and 3.30 suggest that the limit of infinite $Ma, D \sim 1 - \epsilon$. This seems to be the maximum distance attainable by the bubble. This approximation fails for small coverages of weak surfactant because of the longer dampened impact that the interfacial surface tension gradient has on the macroscopic flows. Not only is $1 - \epsilon$ the fraction of initially clean surface, it is also equal to half the distance between the back end of the bubble $s = 1$ and the projection on the z-axis of the initial location of the surfactant front Z, described by $1 - \epsilon = (1 + Z)/2$ as seen in Figure 3.29.

The parametric plot shown by Figure 3.30 displays that Marangoni number has a weak influence on total displacement; with stronger surfactants $(Ma > 1)$ producing displacements similar to those from weak surfactants, although at faster speeds. The scaling of overall time T, defined as the time spent to travel 90% of the total distance D, versus Ma for strong surfactant effects $(Ma > 1)$ is $T \sim Ma^{-1}$. This supports why the interactions occurring in the $Ma = 20$ case occurred approximately 10x faster than the $Ma = 2$ case.
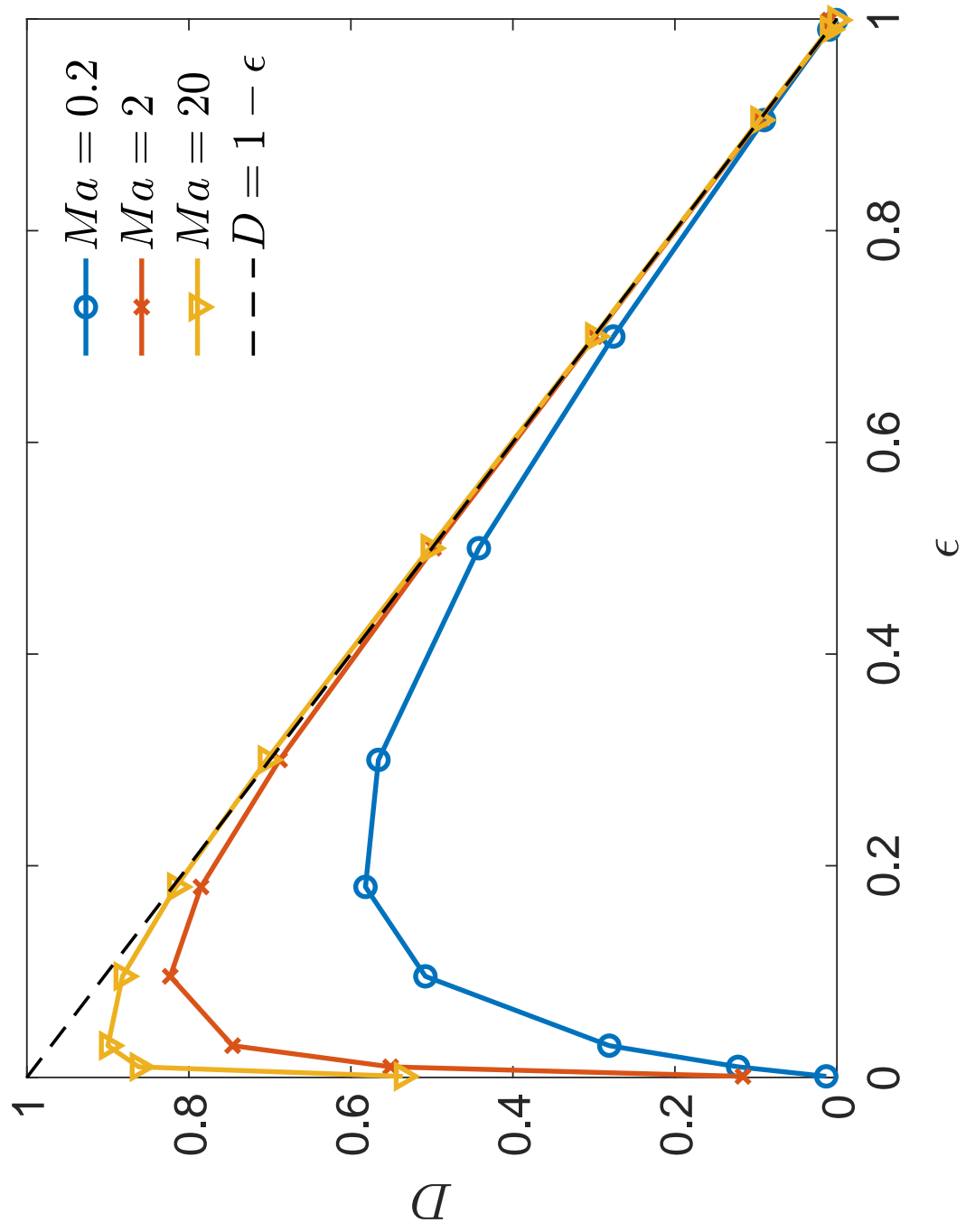
Fig. 3.28. **Influence of surfactant strength on total bubble displacement with various initial coverages.** A Parametric plot showing final bubble displacement D at various surfactant coverages ε. With a power law scaling of $D = 1 - \epsilon$ for bubbles with $Re = 10^{-4}$ and $Ma = 0.2$, $Ma = 2$, and $Ma = 20$.
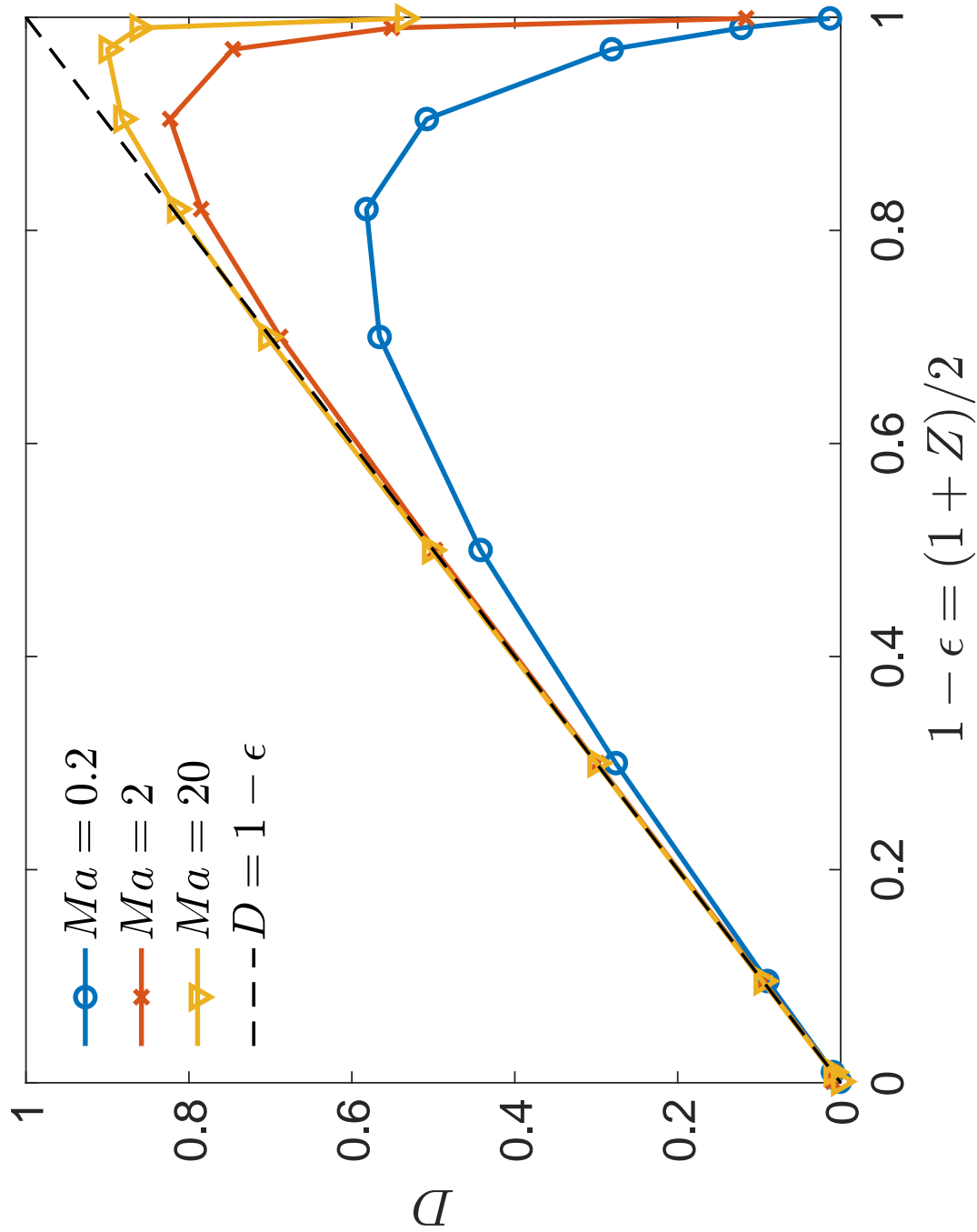
Fig. 3.29. **Influence of surfactant strength on total bubble displacement with various initial coverages.** A Parametric plot showing final bubble displacement D at various clean surface coverages $(1 - \epsilon)$. With a power law scaling of $D = 1 - \epsilon$ for bubbles with $Re = 10^{-4}$ and $Ma = 0.2$, $Ma = 2$, and $Ma = 20$.
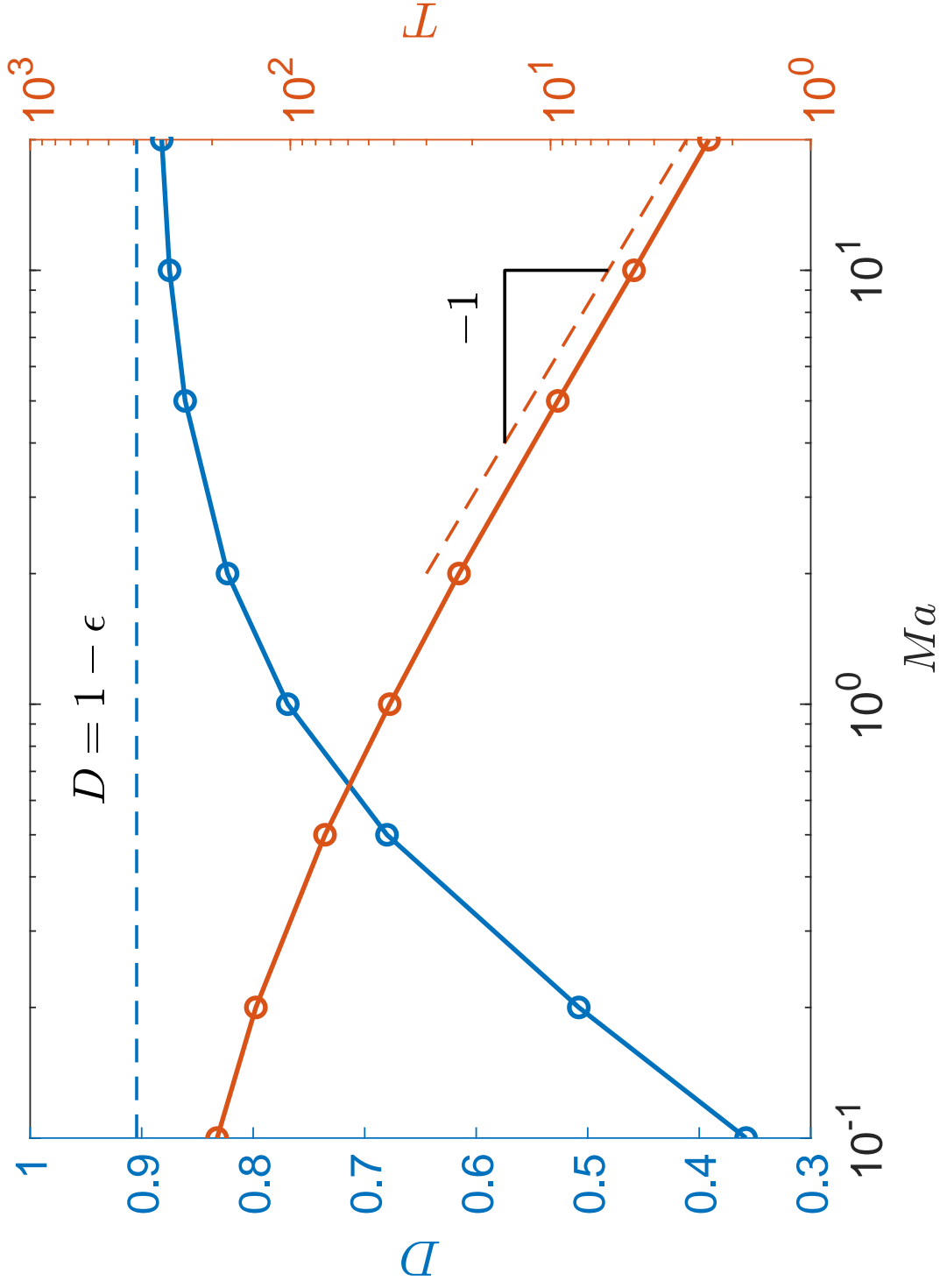
Fig. 3.30. **Influence of surfactant strength on total bubble displacement and time of bubble movement.** A Parametric plot showing final bubble displacement D (orange) and time to reach D, T, (blue) at various surfactant strengths Ma. With a maximum movement approaching the displacement limit of $D = 1 - \varepsilon$ (dashed blue line) and a scaling of $(T \sim 1/Ma)$ for large surfactant strengths $(Ma > 1)$ for bubbles with $Re = 10^{-4}$ and $\varepsilon = 9.6\%$.

3.4   Influence of Tube Radius R_t on Bubble Propulsion

This section discusses the effect that a smaller capillary tube radius R_t (seen in Figure 3.31) has on Marangoni driven propulsion along the axis of propulsion. Here two bubble cases are examined, where both have a coverage of $\varepsilon = 9.6\%$, Marangoni of $Ma = 2$, and Peclet of $Pe = 10^5$ with an outer-fluid viscosity of $Re = 1$. The cases discussed include a tube with a very large radius $R_t = 20$ and a tube with a very small radius of $R_t = 1.1$ leaving a gap 10% of R between the tube and the bubble initially centered at $z = 0$. A result of this study will be further understanding of self-induced propulsion comparing the mechanisms involved with active microbubbles in a free system versus a narrow capillary similar to a blood vessel ([14], [15]).

The bubble in the small tube $R_t = 1.1$ possesses qualities that are similar to the bubble in the large tube $R_t = 20$ at early times. For early periods in the propulsion process (up to $t \approx 0.1$), both cases share almost identical movements when tracking the front and back of the bubble; as seen by the displacement of the bubble center of mass (z_M) and the bubble ends (d_F and d_B) (seen in Figures 3.33 and 3.32). The bubble ends have nearly identical speeds (v_F and v_B) (seen in Figure 3.34) at early times (up to $t \approx 10^{-3}$).

A major discrepancy is then seen at later times (at $t \approx 10^{-3}$) in Figure 3.35 with the velocity of the center of mass v_M of the $R_t = 20$ (solid orange line) bubble moving in the positive direction on the axis of propulsion, whereas the $R_t = 1.1$ (solid blue line) bubble has a negative velocity until $t \approx 1$ when the bubble center of mass velocity becomes positive. Figure 3.33 supports this evidence of a negative velocity of the center of mass by showing that after $t \approx 0.1$, the back end of the $R_t = 1.1$ bubble is seen moving slightly in the negative direction along with the Marangoni flows interacting with the nearby tube causing the bubble front end to flatten, driving the center of mass backward. According to Figure 3.33, after $t \approx 0.1$, both ends of the $R_t = 20$ begin to move forward with the back end d_B (dashed orange line) lagging slightly behind the front end d_F (solid orange line), whereas for $R_t = 1.1$
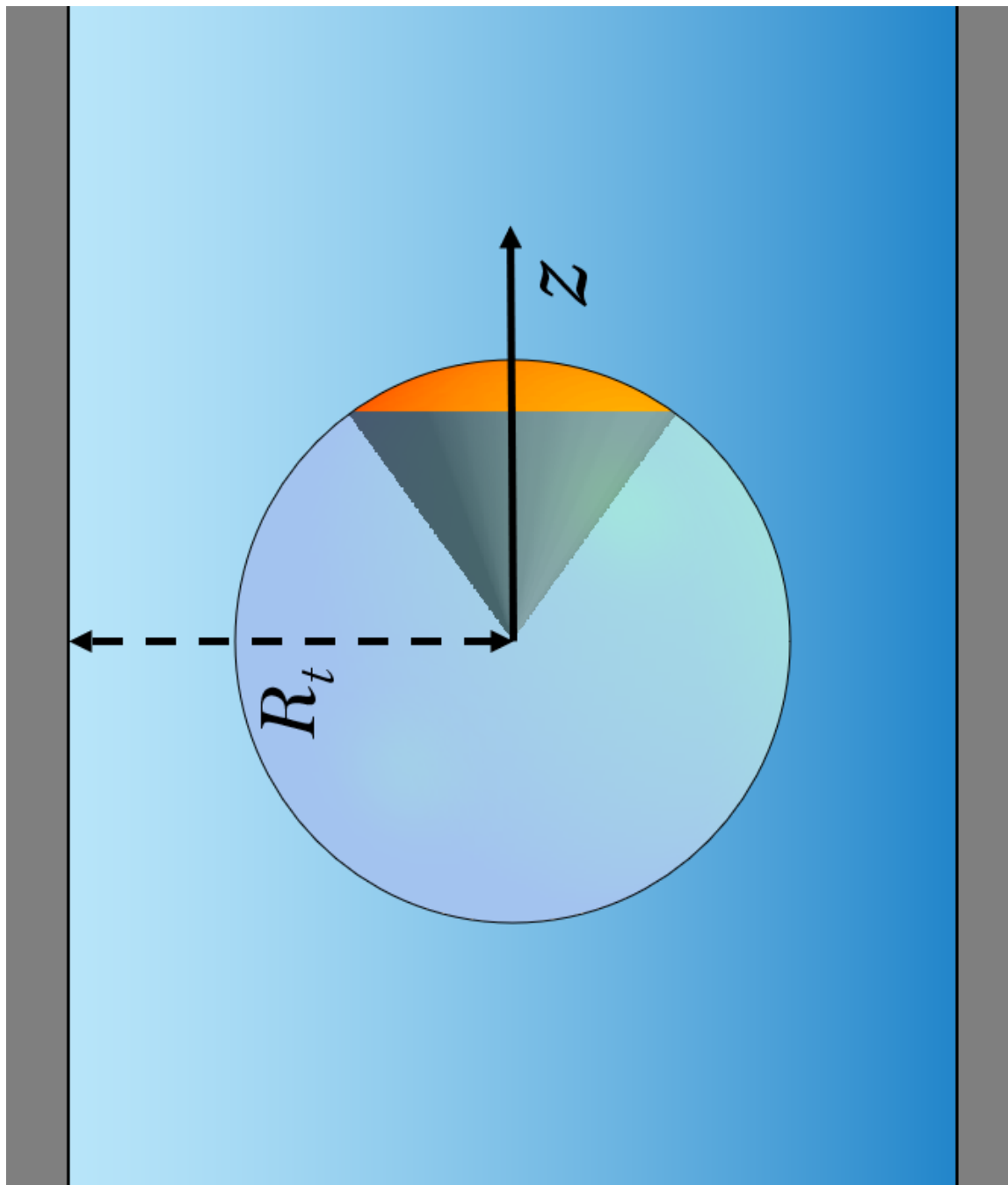
Fig. 3.31. **Sketch displaying the definition of R_t.**
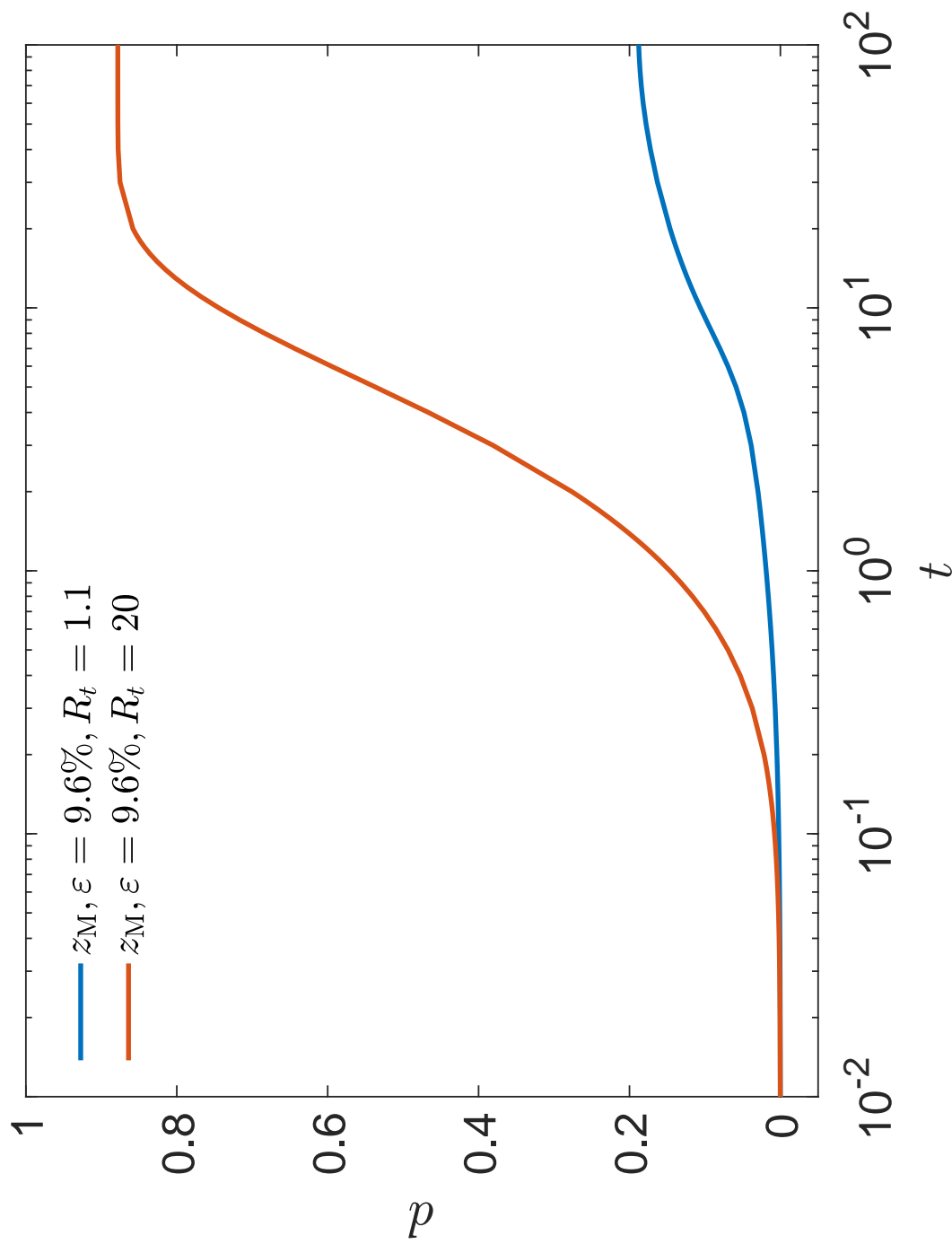
Fig. 3.32. **Temporal evolution of the bubble center of mass displacement for different tube radii.** Comparing the displacement d of the center of mass z_M over time t of $R_t = 1.1$ (blue line) and $R_t = 20$ (orange line) for $\varepsilon = 9.6\%$, $Re = 1$, $Ma = 2$, and $Pe = 10^4$.
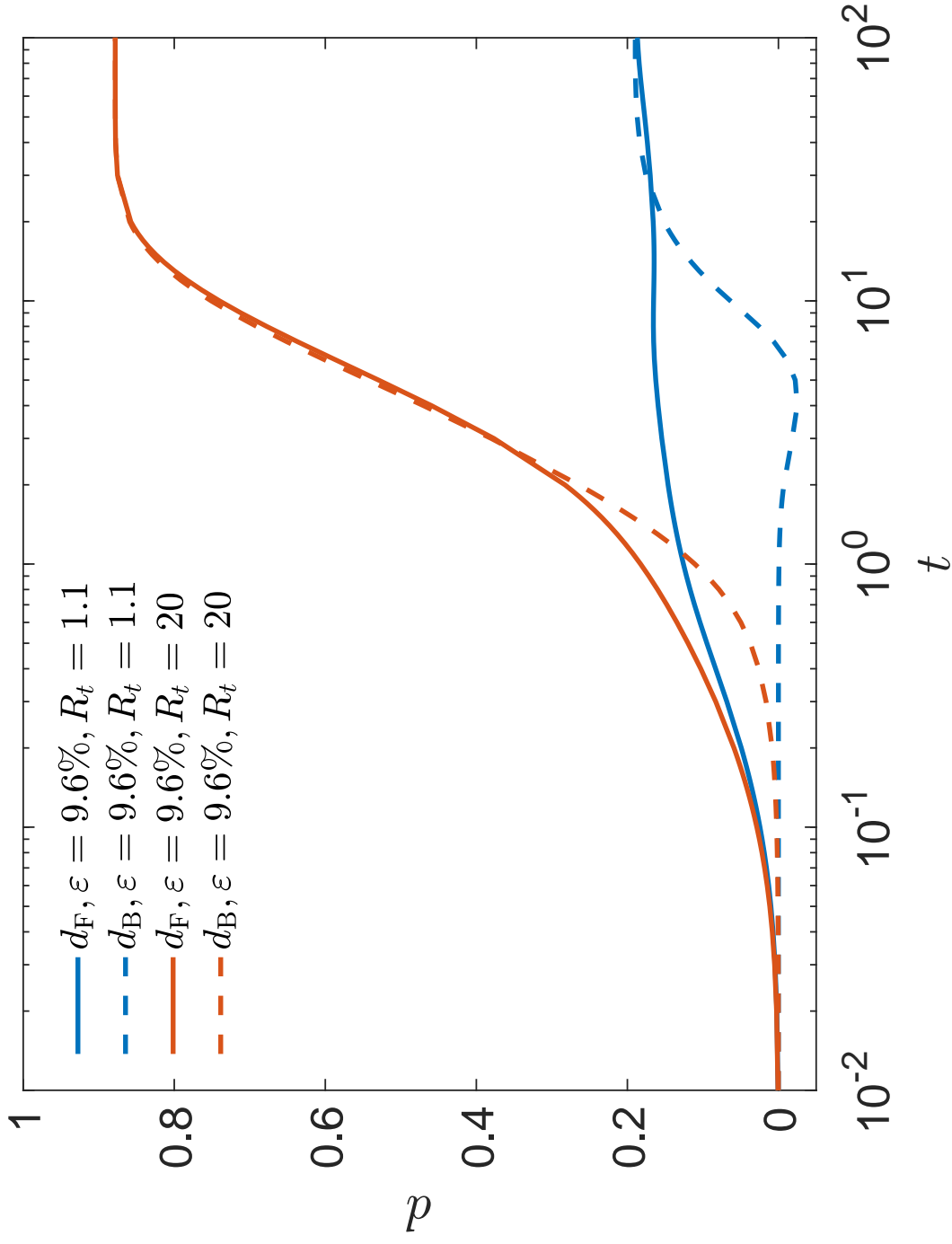
Fig. 3.33. **Temporal evolution of the bubble front and back end displacements for different tube radii.** Comparing the displacement d of the bubble front d_F (solid line) and back d_B (dashed line) ends over time t of $R_t = 1.1$ (blue) and $R_t = 20$ (orange) for $\varepsilon = 9.6\%$, $Re = 1$, $Ma = 2$, and $Pe = 10^4$.
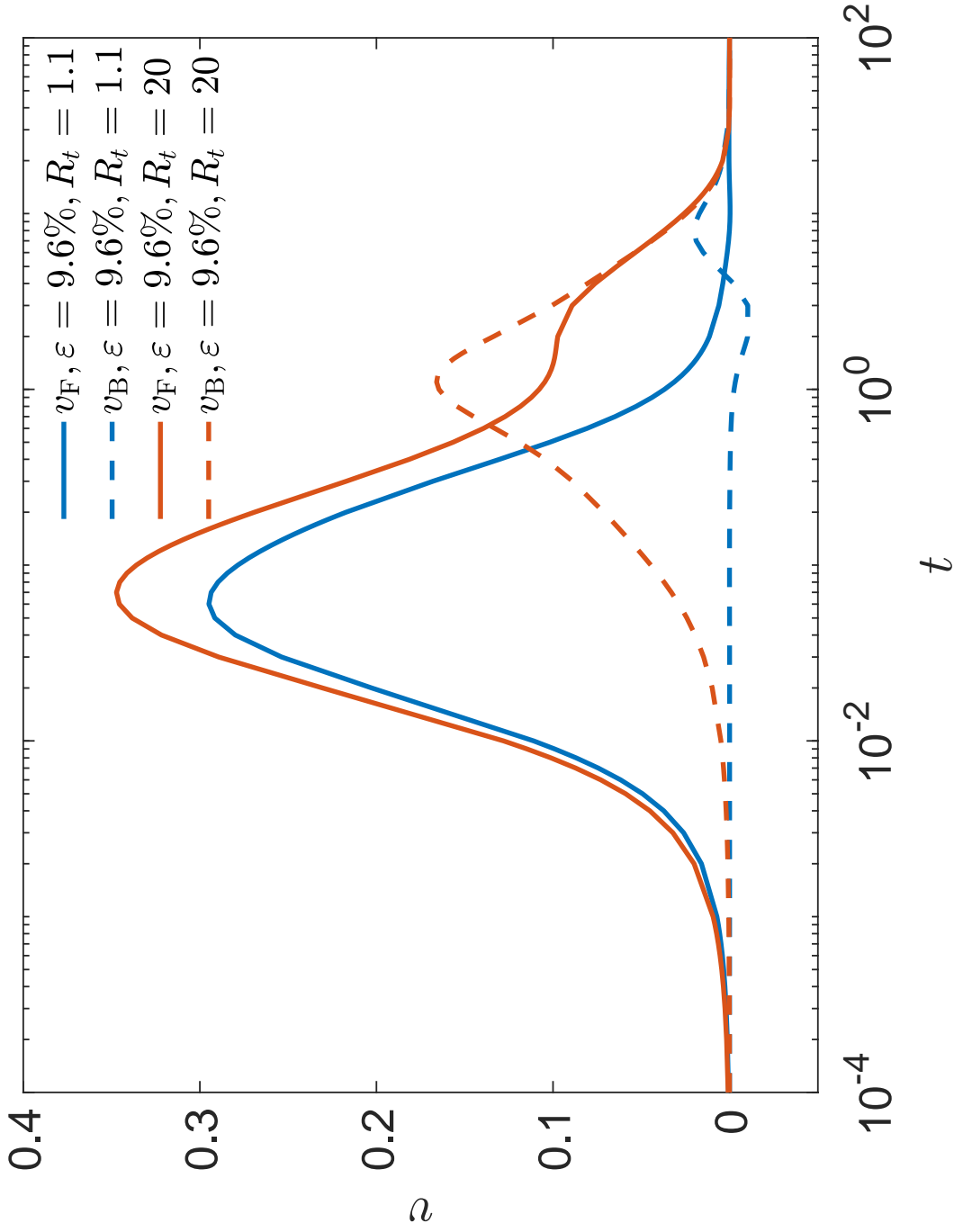
Fig. 3.34. **Temporal evolution of the bubble front and back end velocities for different tube radii.** Comparing the velocity v of the bubble front v_F (solid line) and back v_B (dashed line) ends over time t of $R_t = 1.1$ (blue) and $R_t = 20$ (orange) for $\varepsilon = 9.6\%$, $Re = 1$, $Ma = 2$, and $Pe = 10^4$.
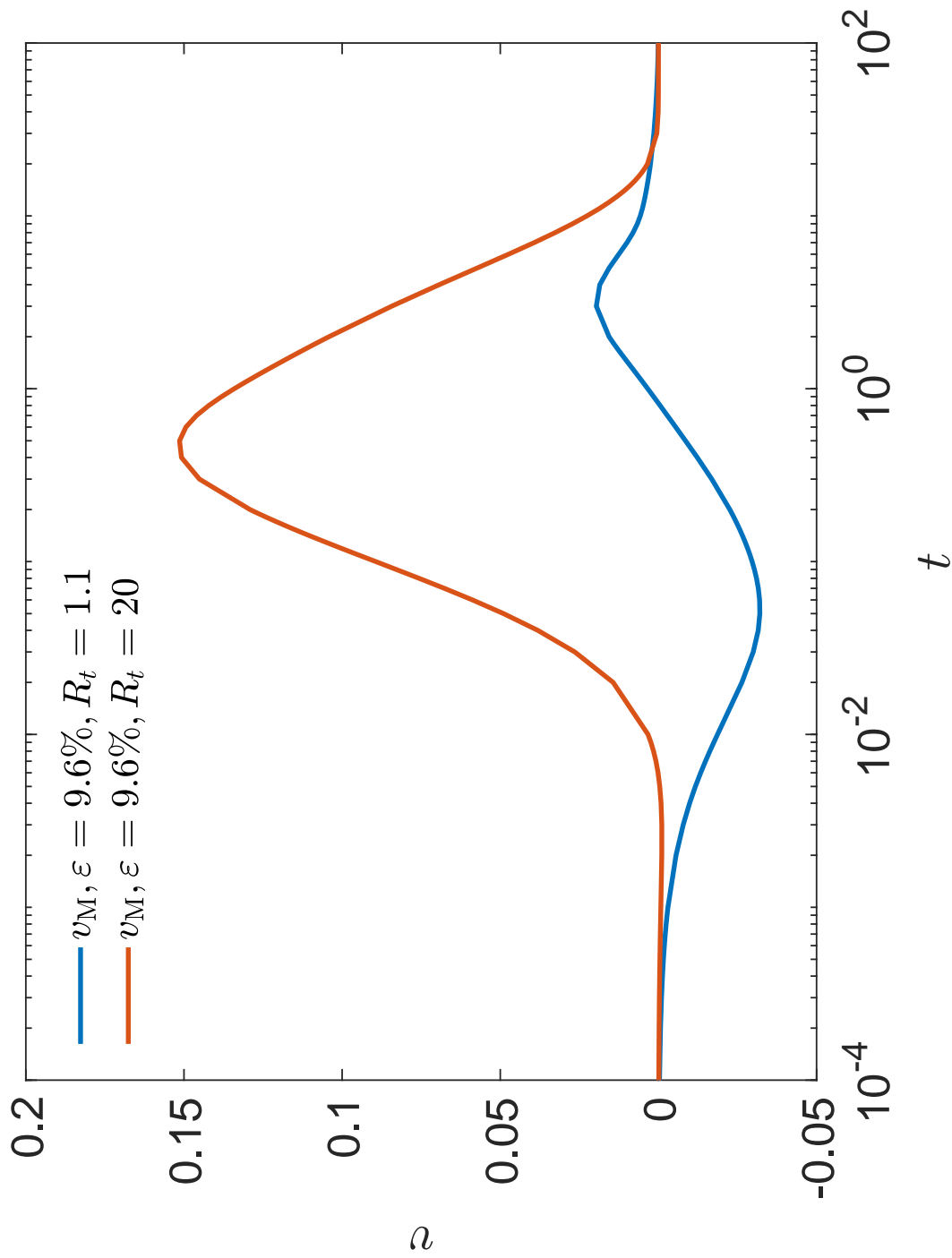
Fig. 3.35. **Temporal evolution of the bubble center of mass velocity for different tube radii.** Comparing the velocity v of the center of mass v_M over time t of $R_t = 1.1$ (blue line) and $R_t = 1.1$ (orange line) for $\varepsilon = 9.6\%$, $Re = 1$, $Ma = 2$, and $Pe = 10^4$.

the front end d_F (solid blue line) moves for decades of time before the back end d_B (dashed blue line) begins to move forward at $t \approx 5$. The movement of the back end d_B only occurred when the surfactant front passed the center of the bubble normalized arc-length $s = 0.5$ at $t \approx 5$ shown in Figure 3.36(b) with the solid purple line.

The Marangoni flow influenced by the surfactant front is unable to obtain the previously seen puller hydrodynamic state of the $R_t = 20$ bubble shown by the outer-fluid arrow velocity plot in Figure 3.37(a) at $t \approx 0.6$, with fluid being pulled from the front end of the bubble towards the back. Similarly, Figure 3.37(d) shows the $R_t = 1.1$ bubble pulling fluid from the front end of the bubble. However, the flow is constricted by the proximity of the bubble to the tube walls which prevents the Marangoni flows from reaching the back end until the surfactant front on the bubble interface passes the constricted region between the bubble and the wall at (e) $t \approx 5$ where the pusher active motion state is able to be completed.

The impact that the tube radius has on the interfacial Marangoni flows can be seen in Figure 3.38 when comparing the tangential velocities v_t on the bubble interfaces at similar surfactant front locations for $R_t = 20$ (a) and $R_t = 1.1$ (b). Tangential velocities are slightly larger for $R_t = 20$ with the v_t seen deforming for $R_t = 1.1$ at $s \approx 0.4$ where the proximal tube begins to interfere with the Marangoni stresses. Figure 3.36 shows that the presence of a nearby tube slows the migration of the surfactant front with the surfactant front at similar locations on the normalized arc-length s occurring at later times for $R_t = 1.1$ compared to $R_t = 20$.

As a result of the nearby boundary, the Marangoni flows generated at the front region of the bubble are unable to influence the rear section of the $R_t = 1.1$ bubble in order to propel it at early times $t < 5$, shown in Figure 3.33. During these early times $t < 5$ displacement d of the bubble front end d_F (solid blue line) increases while the bubble back end d_B (dashed blue line) remains relatively immobile. This results in the bubble elongating roughly two times more that the bubble with a larger tube radius of $R_t = 20$. This is seen in the maximum flattening value f of $R_t = 1.1$ being roughly double that of $R_t = 20$ seen in Figure 3.39.

When comparing the interface shape at the times of maximum flattening, seen in Figure 3.40, $R_t = 20$ (a) shows visibly less elongation compared to $R_t = 1.1$. The outer-fluid velocity field in Figure 3.41 (a) shows the of maximum elongation $(t \approx 0.6)$ for $R_t = 20$ occurring at a location of a large surface tension gradient (seen in Figure 3.36 (a) by the solid blue line). Alternatively, Figure 3.41 (e) shows the velocity field at the time of maximum elongation for $R_t = 1.1$ occurring at $t \approx 5$ where the Marangoni stresses are interacting with the nearby tube boundary magnifying the bubble compression as opposed to the larger surface tension gradients at times earlier than $t \approx 5$ (seen in Figure 3.36 (b)).

The macroscopic hydrodynamics of the bubble in the narrow tube $(R_t = 1.1)$ differ from the hydrodynamics seen in the free bubble $R_t = 20$. The $R_t = 20$ bubble displays the pulling hydrodynamics (seen in the outer-fluid arrow field Figure 3.37 (a)) until $t \approx 3$ where it transitions to the pushing state for the remainder of the bubble swimming (seen in Figure 3.37 (c)). This differs from the bubble in the narrow tube $R_t = 1.1$, where in Figure 3.37 (d) the bubble is seen pulling fluid from in front and pushing fluid from behind at early times. However, when the surfactant front passes the center of the bubble at $s \approx 0.5$ (seen in Figure 3.36 (b) by the solid purple line at $t = 5$) the Marangoni flows generated by the surfactant front interacts with the wall and a gap between the bubble interface and the wall is formed allowing for fluid to flow back towards the rear of the bubble at $t \approx 5$ as seen in Figure 3.37 (e). This allows for the $R_t = 1.1$ bubble to become a puller at $t \approx 5$ with fluid being pulled from in front of the bubble to behind due to the Marangoni flows compressing the bubble and allowing the flow to reach behind the bubble. At later times, shown in Figure 3.37(f), the bubble regains its circular shape constricting the fluid flow resulting in hydrodynamics returning to a similar state shown in Figure 3.37 (d).

(a) $R_t = 20$

(b) $R_t = 1.1$
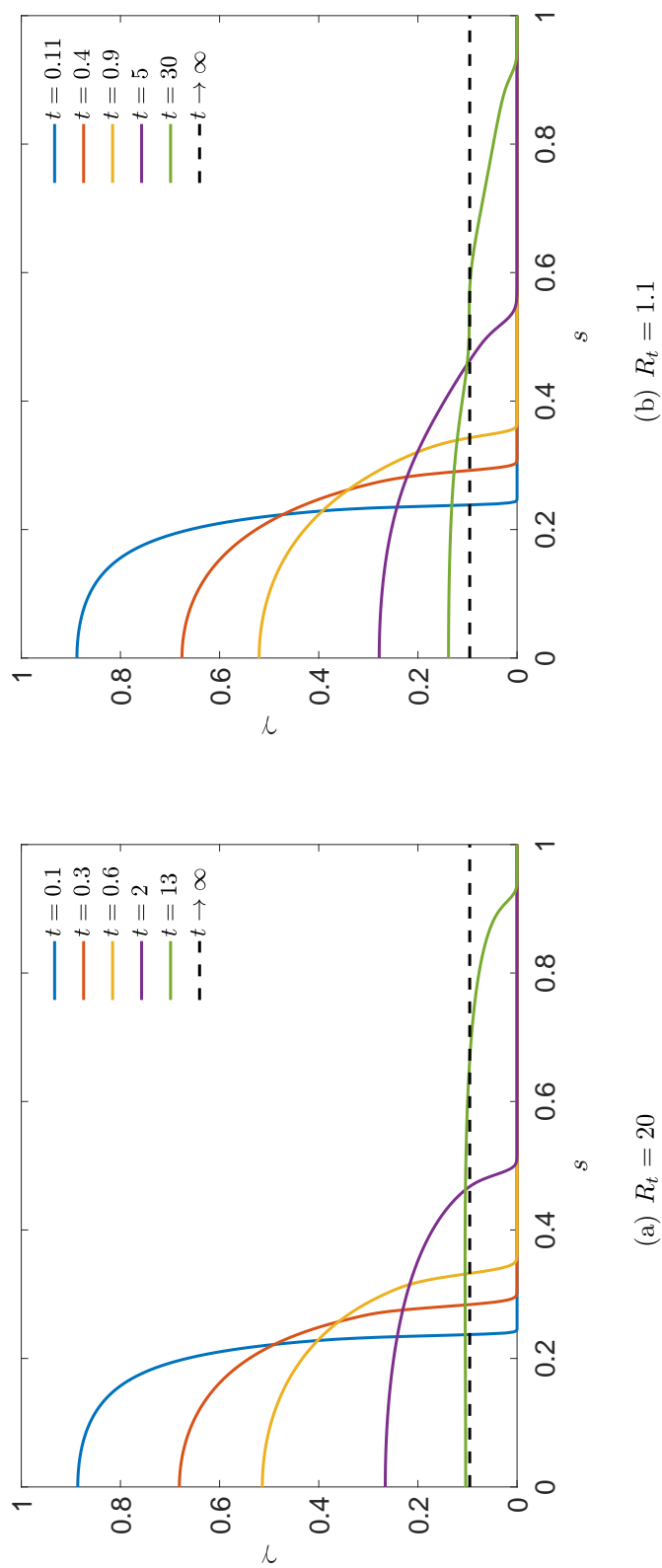
Fig. 3.36. **Influence of tube radii on the evolution of the concentration profiles on the bubble interface.** Comparing the surfactant concentration γ across the bubble normalized arc-length s at various times with similar γ profiles for $\varepsilon = 9.6\%$, $Re = 1$, $Ma = 2$, and $Pe = 10^4$.

(a) $t = 0.6$

(b) $t = 2$

(c) $t = 13$

(d) $t = 0.9$

(e) $t = 5$
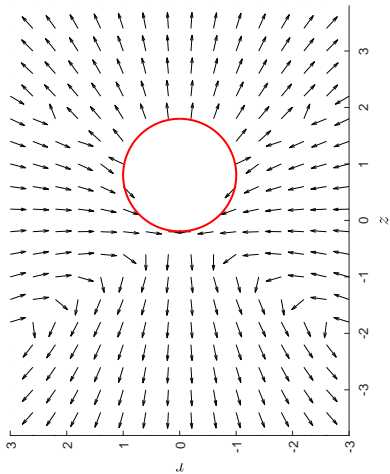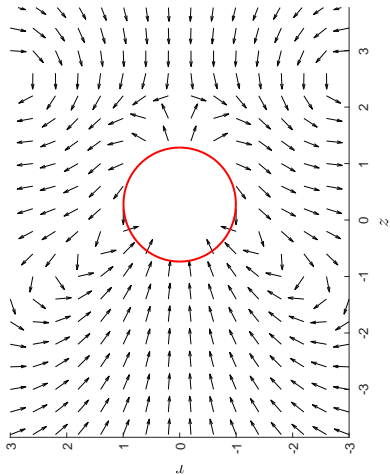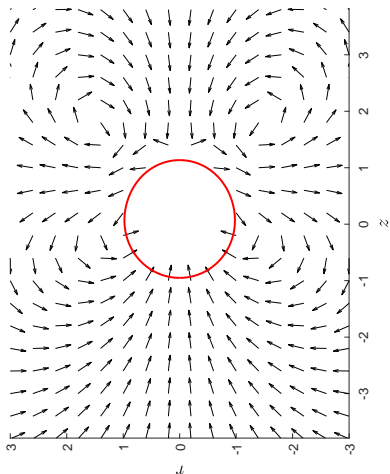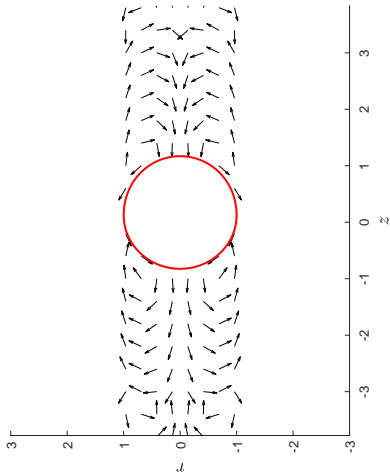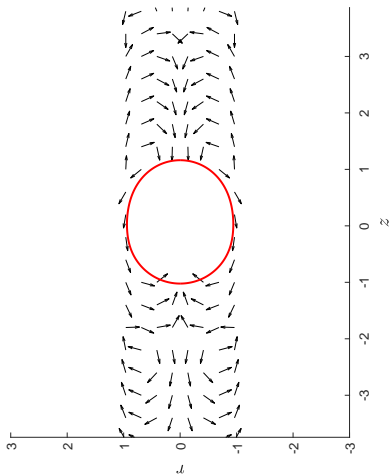
(f) $t = 30$
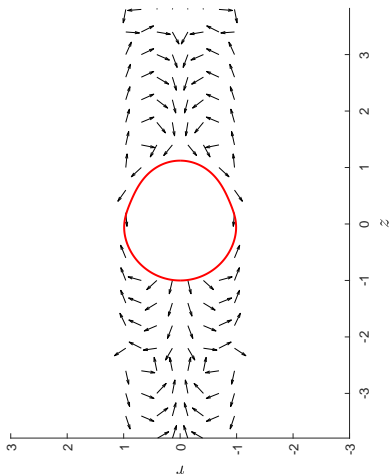
Fig. 3.37. **Influence of tube radii on the temporal evolution of the velocity arrow field for the active bubble.** The evolution of the arrow velocity field of the outer viscous fluid over time. Earliest time shown starting at the left, with the latest time shown at the right with the Top: $R_t = 20$ and Bottom: $R_t = 1.1$, $\varepsilon = 9.6\%$, $Re = 1$, $Ma = 2$, and $Pe = 10^4$.

(a) $R_t = 20$

(b) $R_t = 1.1$
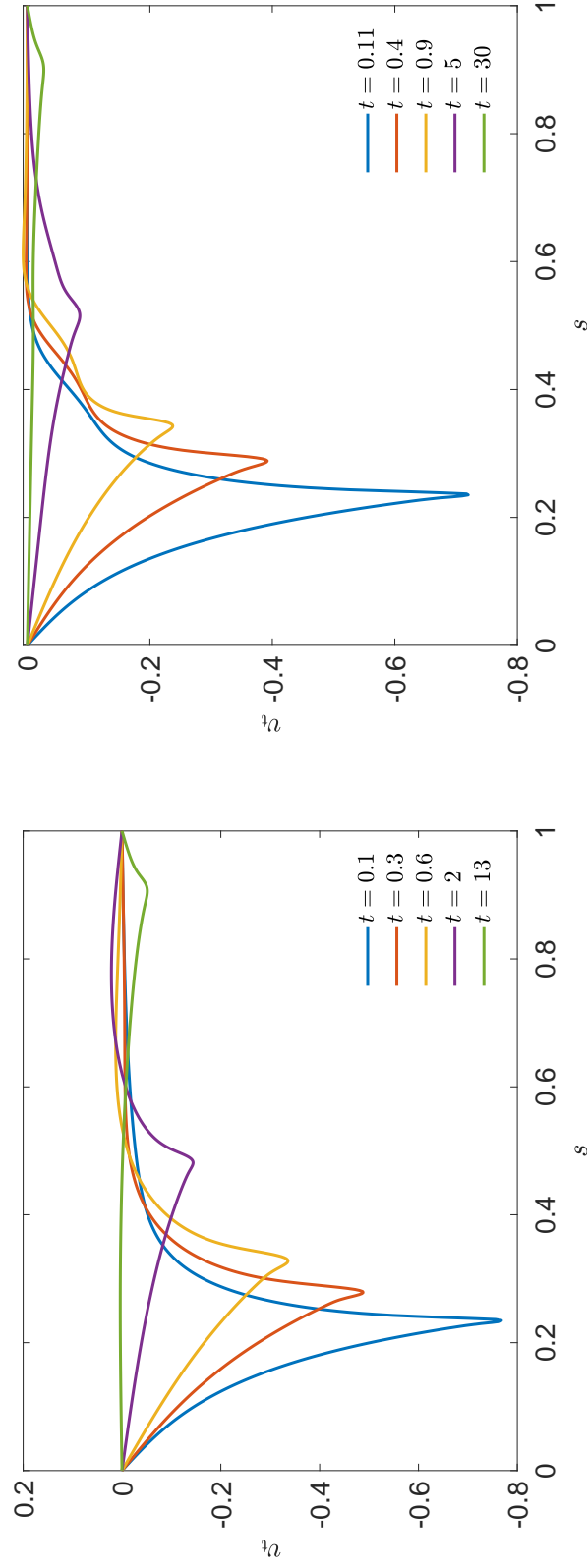
Fig. 3.38. **Influence of tube radii on the evolution of the tangential velocity profiles on the bubble interface.** Comparing the tangential velocity v_t across the bubble normalized arc-length s at various times with similar v_t profiles for $\varepsilon = 9.6\%$, $Re = 1$, $Ma = 2$, and $Pe = 10^4$.
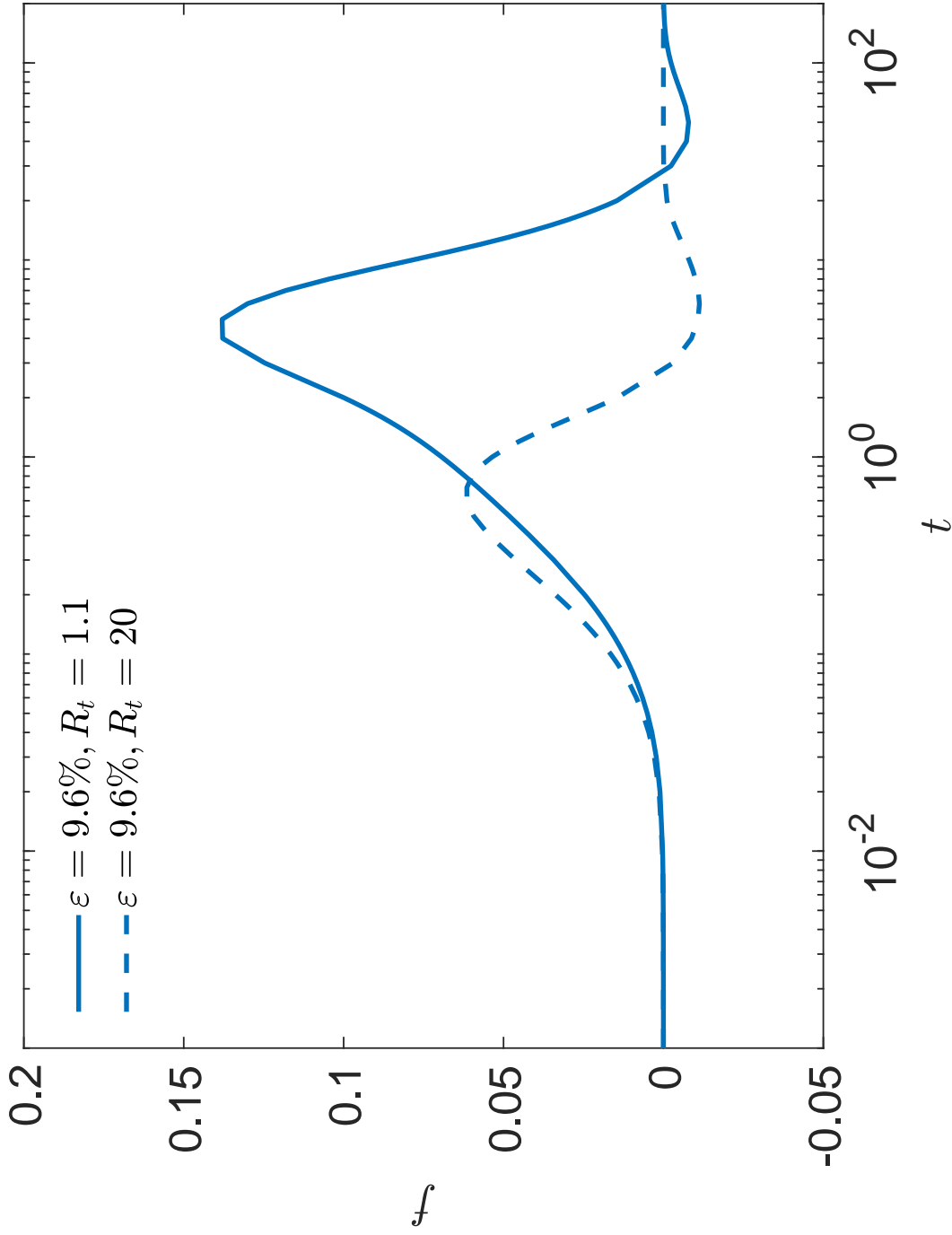
Fig. 3.39. **Temporal evolution of the bubble flattening of different tube radii.** Comparing the flattening f of the $R_t = 1.1$ (solid blue line) and $R_t = 20$ (dashed blue line) for $\varepsilon = 9.6\%$, $Re = 1$, $Ma = 2$, and $Pe = 10^4$. Flattening is described as $f = 1 - (b/a)^2$, where a is the maximum bubble size in the axial direction and b is the maximum size in the radial direction.
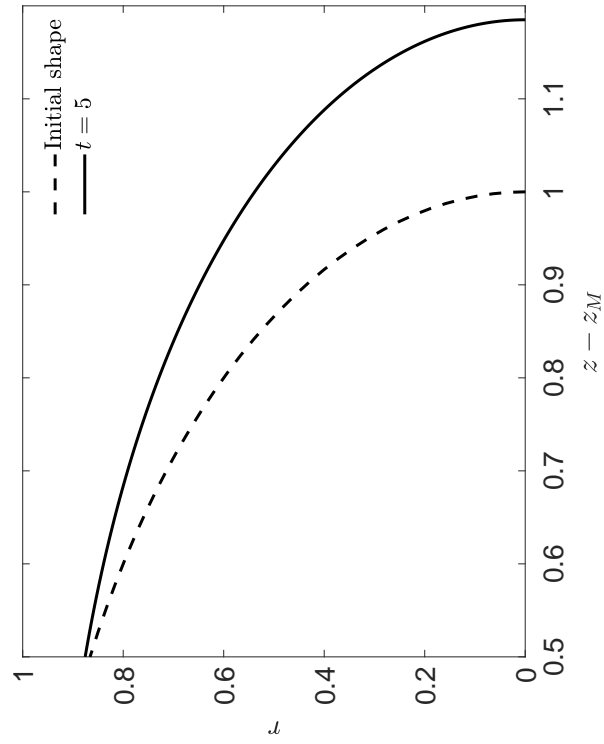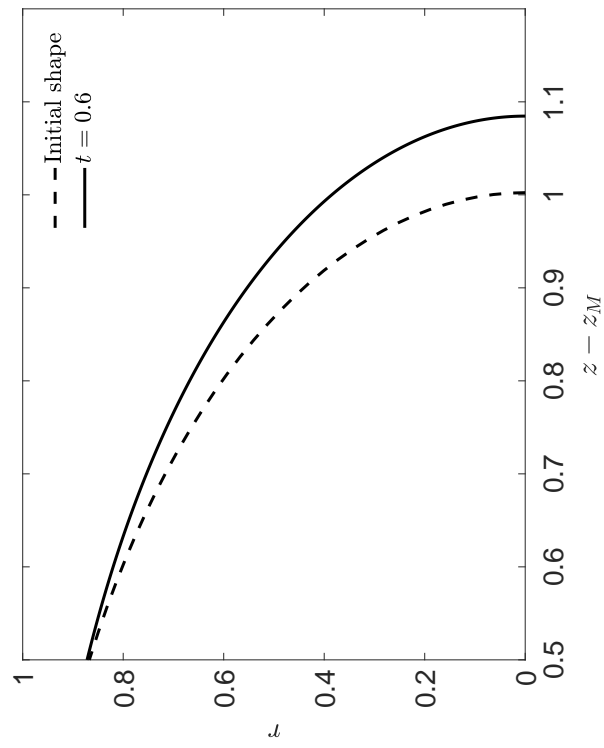
Fig. 3.40. **Maximum deformation interface shapes of bubbles with different tube radii.** Comparing the maximum deformed interface shape (solid black line) against the initial bubble interface shape (dashed black line) for $\varepsilon = 9.6\%$, $Re = 1$, $Ma = 2$, and $Pe = 10^4$.
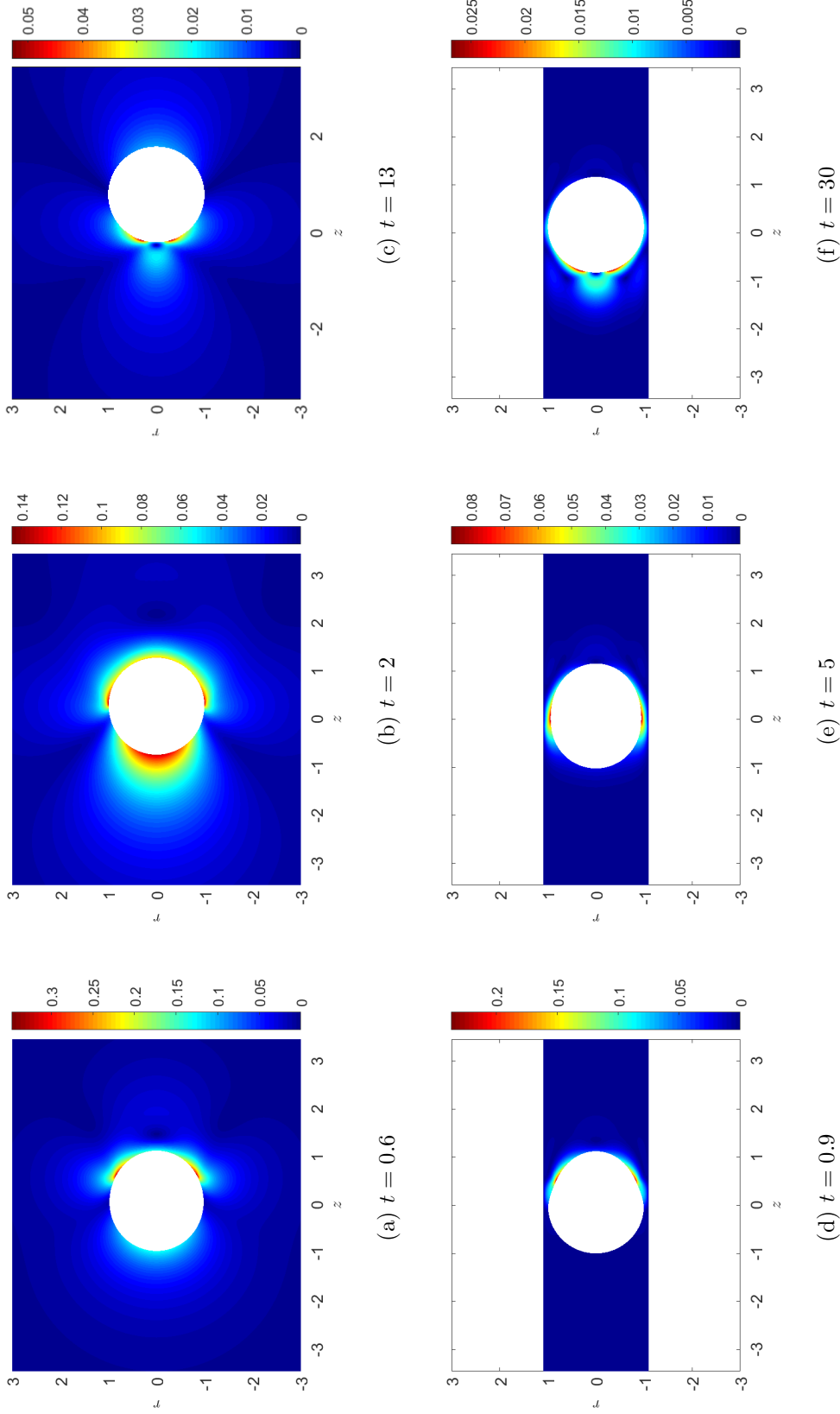
Fig. 3.41. **Influence of tube radii on the temporal evolution of the velocity magnitude field for the active bubble.** The evolution of the velocity magnitude $|V|$ of the outer viscous fluid over time. Earliest time shown starting at the left, with the latest time shown at the right with the Top: $R_t = 20$ and Bottom: $R_t = 1.1$, $\varepsilon = 9.6\%$, $Re = 1$, $Ma = 2$, and $Pe = 10^4$.

3.4.1 R_t **Parametric Study**

The movement of the center of mass z_M for the different tube radii vary greatly as seen in Figure 3.32 where the total distance D travelled by the bubble for $R_t = 20$ was $D \approx 0.878$, whereas for $R_t = 1.1$ the total distance was $D \approx 0.189$. A parametric study was completed to show how D changes with differing R_t. Figure 3.42 shows that D versus R_t follows a logarithmic growth curve with the maximum distance the bubble being able to travel being $D \approx 0.88$ while the minimum bubble displacement trending towards $D = 0$ as $R_t \to R$.

The Figure 3.43 plot shows the overall time (T, defined as the time spent to travel 90% of the total distance D) and the average speed (defined as $U \equiv D/T$) as a function of the capillary tube radius R_t. Smaller tube radius resulted in a longer duration of movement with a slower velocity. In conclusion, a tube radius has a negative impact on active self-propelled bubble movement.
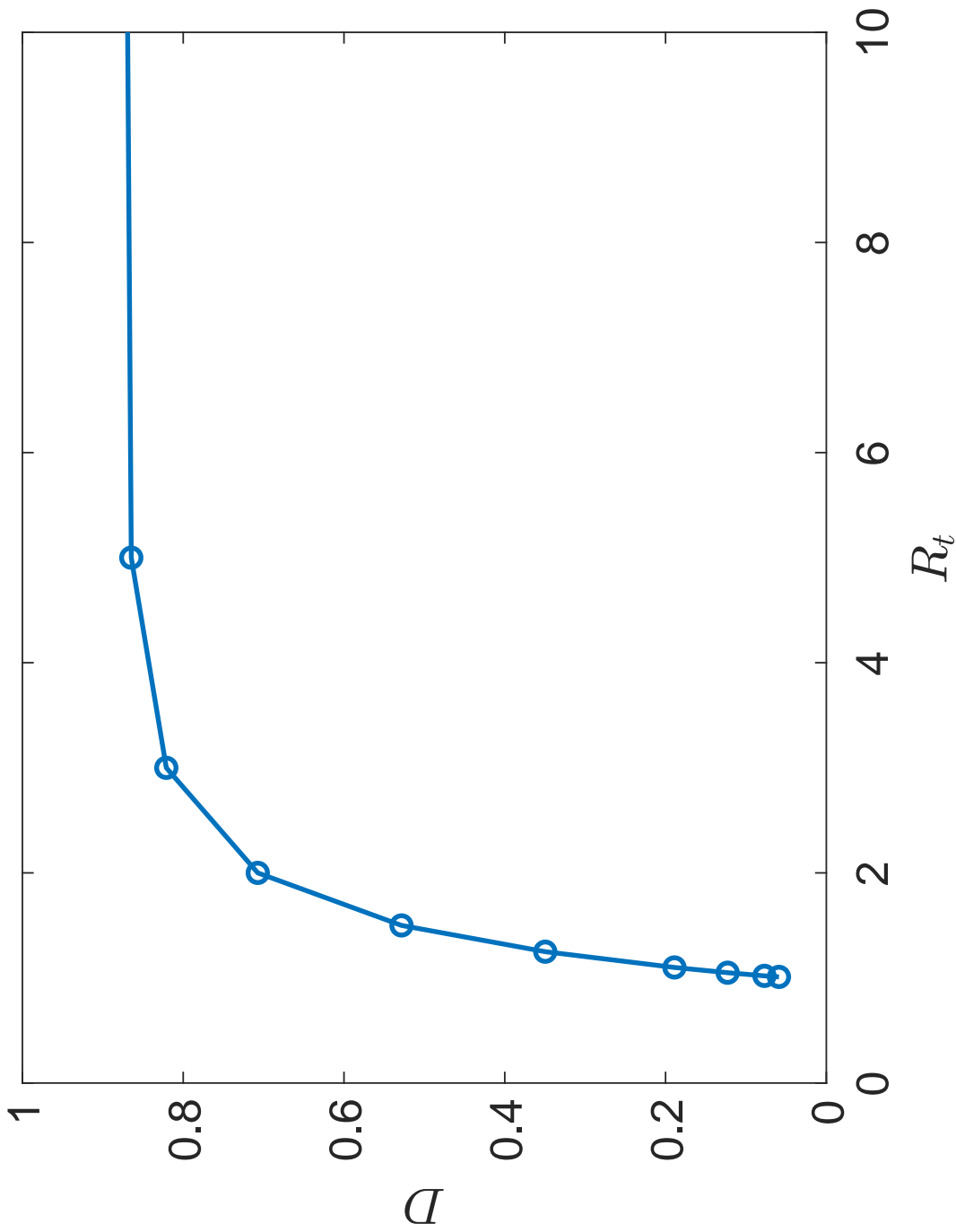
Fig. 3.42. **Influence of tube radius on total bubble displacement.** A Parametric plot showing final bubble displacement D at various tube radii R_t for bubbles with $Re = 1$, $Ma = 2$, and $Pe = 10^4$.
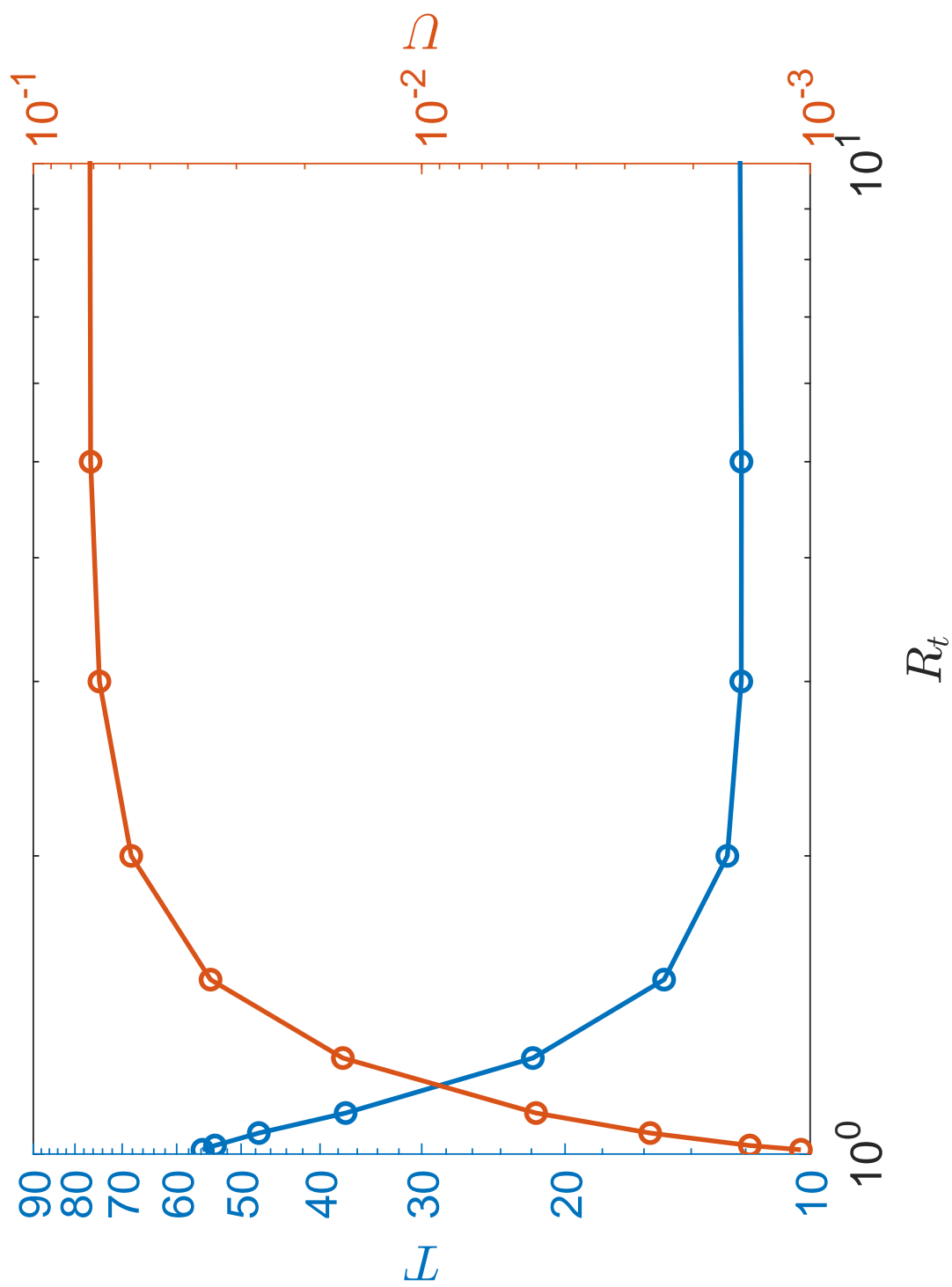
Fig. 3.43. **Influence of tube radius on average bubble velocity and time of bubble movement.** A Parametric plot showing bubble showing the average bubble velocity U (orange) and time to reach D, T, (blue) at various tube radii R_t for bubbles with $Re = 1$ $Ma = 2$, and $Pe = 10^4$.

3.5 Conclusion

This chapter investigated a variety of parameters to more fully understand the bubble self-propulsion mechanisms. These parameters included the impact of the initial size of surfactant coverage, the impact of various surfactant strengths, and the impact of tubular boundaries at various distances away from the bubble and their impact on the bubble propulsion. Previous similar works over these parameters influencing active motion include the impact of various fixed coverages of surface-active species on particles previously studied by [39], the influence of various surfactant strengths on particle propulsion previously studied by [47], and the influence of a small tube on Marangoni flows for a bubble or drop interface being previously investigated by [46], [14], and [15].

Results showed that the extent of contaminated area of the interface has a strong effect on the total bubble displacement and speed. Smaller initially contaminated regions were shown to typically achieve faster speeds and larger displacements. These results are relevant to the study of long-term bubble migration, which may bring large bubble groups far from equilibrium. Bubbles can easily be brought far away from equilibrium by a small contaminated fraction of the interface and remain far from equilibrium for a long time with very slow dynamics. The surfactant strength also has an impact on displacement with the stronger surfactants creating larger displacements than weaker surfactants along with quicker bubble movement. The investigation of tube radius revealed that smaller tube radii constricted the Marangoni stresses in the bulk fluid resulting in a dampened movement of the bubble when compared to the bubble propelling in a larger tube.

4. SUMMARY AND OUTLOOK

In this research, the interfacial mechanisms and external flows of contaminated bubble self-propulsion were thoroughly investigated. Characterization of various regimes created by the presence of surface active species on the bubble interface were tested along with the influence of neighboring boundaries on the performance of bubble active motion. The free-surface mechanisms of Marangoni flows created by gradients in surfactant concentration resulting in particle movement were studied using an accurate computational model. Better understanding of self-induced bubble movement generated by Marangoni flows was gained by simultaneously solving the Navier-Stokes, continuity, kinematic, and conservation of surfactant equations.

The second chapter of this thesis focused on understanding the mechanics associated with the active motion of bubbles harnessing these Marangoni flows. Simulations enabled an in depth investigation of the physical mechanisms of interfacial motion created by surfactant gradients being coupled with the flows of the bulk liquid through the transfer of momentum. The simulations were benchmarked against theoretical predictions from literature of surfactant spreading on thin viscous films. The results were used to describe how asymmetric surfactant coverage produces hydrodynamic flows in the outer fluid resulting in bubble propulsion. A transition of self-induced propulsion hydrodynamic states was observed with the bubble transitioning from a puller at early times into a pusher at later times. This transition occurred when the Marangoni stresses transition from acting on the front half of the bubble to the back half, following the surfactant gradient. These pusher and puller dynamics are important when understanding how large numbers of particles with these dynamics are interacting with one another.

The third chapter of this thesis advanced the bubble propulsion investigation completed in Chapter 2 to a parametric study of initial surfactant coverage, surfactant

strength, and tube radius on the active bubble movement. Results showed that the extent of contaminated area of the interface has a strong effect on the total bubble displacement and speed, with smaller initially contaminated regions typically achieving faster speeds and larger displacements. The surfactant strength also has an impact on displacement with the stronger surfactants creating larger displacements than weaker surfactants. The investigation of tube radius revealed that smaller tube radii constricted the Marangoni stresses in the bulk fluid resulting in a dampened movement of the bubble compared to the bubble swimming in a larger tube. These computations allowed for accurate characterization of Marangoni propulsion with various surfactant properties and in various neighboring tubular boundaries.

Understanding the extent of Marangoni propulsion due to chemical species is recognized as important in many industrial and biomedical processes. These range from the cleaning of bio-films and industrial food processing equipment to drug capsule and microfluidic device propulsion. Transport of surfactant on the bubble interface is also seen in environmental and natural processes such as the cleaning of oil spills and microorganism swimming. A more accurate understanding of these microfluidic mechanisms of surfactant induced swimming allows for enhanced regulation of bubble movement in chemical, food, biomedical, and pharmaceutical industries.

This research focused on characterizing self-propulsion regimes created by the existence of contaminants and the influence these contaminants have on active bubble motion. Next steps include generating experimental results to test the regimes discovered by the simulated model. A remaining question is how solubility of the surfactant would alter the self-propulsion mechanism. Further research should include an investigation of an active bubble propelled to a nearby wall to help understand mechanisms of bubble attachment to surfaces in microbubble cleaning.

REFERENCES

REFERENCES

[1] O. E. Jensen and J. B. Grotberg, "Insoluble surfactant spreading on a thin viscous film: shock evolution and film rupture," *Journal of Fluid Mechanics*, vol. 240, p. 259288, 1992.

[2] L. E. Scriven and C. V. Sternling, "The marangoni effects," *Nature*, vol. 187, no. 4733, pp. 186–188, 1960.

[3] V. G. Levich, *Physicochemical hydrodynamics.*, ser. Prentice-Hall international series in the physical and chemical engineering sciences. Englewood Cliffs, N.J.: Prentice-Hall, 1962.

[4] C.-S. Yih, "Three-dimensional motion of a liquid film induced by surface-tension variation or gravity," in *Selected Papers By Chia-Shun Yih: (In 2 Volumes)*. World Scientific, 1991, pp. 958–963.

[5] T. E. Angelini, M. Roper, R. Kolter, D. A. Weitz, and M. P. Brenner, "Bacillus subtilis spreads by surfing on waves of surfactant," *Proceedings of the National Academy of Sciences*, vol. 106, no. 43, pp. 18 109–18 113, 2009.

[6] S. Trinschek, K. John, and U. Thiele, "Modelling of surfactant-driven front instabilities in spreading bacterial colonies," *Soft matter*, vol. 14, no. 22, pp. 4464–4476, 2018.

[7] G. Billard and C. Bruyant, "Sur un mode particulier de locomotion de certains stenus," *CR Soc. Biol*, vol. 59, p. 102, 1905.

[8] T. H. Seah, G. Zhao, and M. Pumera, "Surfactant capsules propel interfacial oil droplets: an environmental cleanup strategy," *ChemPlusChem*, vol. 78, no. 5, pp. 395–397, 2013.

[9] G. Zhao and M. Pumera, "Marangoni self-propelled capsules in a maze: pollutants sense and actin complex channel environments," *Lab on a Chip*, vol. 14, no. 15, pp. 2818–2823, 2014.

[10] S. Thutupalli, D. Geyer, R. Singh, R. Adhikari, and H. A. Stone, "Flow-induced phase separation of active particles is controlled by boundary conditions," *Proceedings of the National Academy of Sciences*, vol. 115, no. 21, pp. 5403–5408, 2018.

[11] D. G. Crowdy, "Wall effects on self-diffusiophoretic janus particles: a theoretical study," *Journal of fluid mechanics*, vol. 735, pp. 473–498, 2013.

[12] W. Uspal, M. N. Popescu, S. Dietrich, and M. Tasinkevych, "Self-propulsion of a catalytically active particle near a planar wall: from reflection to sliding and hovering," *Soft Matter*, vol. 11, no. 3, pp. 434–438, 2015.

[13] L. Baraban, D. Makarov, R. Streubel, I. Monch, D. Grimm, S. Sanchez, and O. G. Schmidt, "Catalytic janus motors on microfluidic chip: deterministic motion for targeted cargo delivery," *ACS nano*, vol. 6, no. 4, pp. 3383–3389, 2012.

[14] J. Zhang, D. M. Eckmann, and P. S. Ayyaswamy, "A front tracking method for a deformable intravascular bubble in a tube with soluble surfactant transport," *Journal of Computational physics*, vol. 214, no. 1, pp. 366–396, 2006.

[15] K. Mukundakrishnan, P. Ayyaswamy, and D. Eckmann, "Bubble motion in a blood vessel: shear stress induced endothelial cell injury," *Journal of biomechanical engineering*, vol. 131, no. 7, 2009.

[16] S. Lertruamporn, M. Thongpiam, P. Saikhwan, and Y.-M. Chew, "Investigation of fabric cleaning using fluid dynamic gauging: Effects of fine bubbles," in *2nd Annual InterPore UK Chapter conference (Joint with the Particle Characterisation Interest Group of the Royal Society of Chemistry)*, 2016.

[17] E. P. Kalogianni, E. M. Varka, T. D. Karapantsios, and S. Pegiadou, "Dynamic surface activity of phenylalanine glycerol- ether surfactant solutions measured by a differential maximum bubble pressure tensiometer," *Langmuir*, vol. 22, no. 1, pp. 46–51, 2006.

[18] R. Clift, J. R. Grace, and M. E. Weber, *Bubbles, drops, and particles*. Courier Corporation, 2005.

[19] R. L. Stefan and A. J. Szeri, "Surfactant scavenging and surface deposition by rising bubbles," *Journal of colloid and interface science*, vol. 212, no. 1, pp. 1–13, 1999.

[20] G. Bleys and P. Joos, "Adsorption kinetics of bolaform surfactants at the air/water interface," *The Journal of Physical Chemistry*, vol. 89, no. 6, pp. 1027–1032, 1985.

[21] D. Langevin, "Bubble coalescence in pure liquids and in surfactant solutions," *Current Opinion in Colloid & Interface Science*, vol. 20, no. 2, pp. 92–97, 2015.

[22] M. Miyamoto, S. Ueyama, N. Hinomoto, T. Saitoh, S. Maekawa, and J. Hirotsuji, "Degreasing of solid surfaces by microbubble cleaning," *Japanese journal of applied physics*, vol. 46, no. 3R, p. 1236, 2007.

[23] A. Agarwal, W. J. Ng, and Y. Liu, "Principle and applications of microbubble and nanobubble technology for water treatment," *Chemosphere*, vol. 84, no. 9, pp. 1175–1180, 2011.

[24] J. Thomson, "Xlii. on certain curious motions observable at the surfaces of wine and other alcoholic liquors," *The London, Edinburgh, and Dublin Philosophical Magazine and Journal of Science*, vol. 10, no. 67, pp. 330–333, 1855.

[25] H. Matsuno, T. Ohta, A. Shundo, Y. Fukunaga, and K. Tanaka, "Simple surface treatment of cell-culture scaffolds with ultrafine bubble water," *Langmuir*, vol. 30, no. 50, pp. 15 238–15 243, 2014.

[26] J. C. Slattery, *Interfacial Transport Phenomena*. Springer New York : Imprint: Springer, 1990.

[27] R. Aris, *Vectors, Tensors and the Basic Equations of Fluid Mechanics*, ser. Dover Books on Mathematics. Newburyport: Dover Publications, 2012.

[28] H. A. Stone, "A simple derivation of the time-dependent convective-diffusion equation for surfactant transport along a deforming interface," *Physics of Fluids A: Fluid Dynamics*, vol. 2, no. 1, pp. 111–112, 1990.

[29] H. Wong, D. Rumschitzki, and C. Maldarelli, "On the surfactant mass balance at a deforming fluid interface," *Physics of Fluids*, vol. 8, no. 11, pp. 3203–3204, 1996.

[30] S. Hansen, G. Peters, and H. Meijer, "The effect of surfactant on the stability of a fluid filament embedded in a viscous fluid," *Journal Of Fluid Mechanics*, vol. 382, pp. 331–349, 1999.

[31] D. Campana, J. Di Paolo, and F. Saita, "A 2-d model of rayleigh instability in capillary tubes–surfactant effects," *International Journal of Multiphase Flow*, vol. 30, no. 5, pp. 431–454, 2004.

[32] V. Dravid, S. Songsermpong, Z. Xue, C. M. Corvalan, and P. E. Sojka, "Two-dimensional modeling of the effects of insoluble surfactant on the breakup of a liquid filament," *Chemical Engineering Science*, vol. 61, no. 11, pp. 3577–3585, 2006.

[33] R. Taylor and O. C. Zienkiewicz, *The finite element method.* Butterworth-Heinemann, 2013.

[34] J. Donea, A. Huerta, J.-P. Ponthot, and A. Rodriguez-Ferran, "Arbitrary lagrangian-eulerian methods, volume 1 of encyclopedia of computational mechanics, chapter 14," *John Wiley & Sons Ltd*, vol. 3, pp. 1–25, 2004.

[35] S. COMSOL AB, "Sweden. comsol multiphysics version 5.4," 2018.

[36] A. M. Winslow, "Numerical solution of the quasilinear poisson equation in a nonuniform triangle mesh," *Journal of Computational Physics*, vol. 135, no. 2, pp. 128–138, 1997.

[37] P. R. Amestoy, I. S. Duff, J.-Y. L'Excellent, and J. Koster, "A fully asynchronous multifrontal solver using distributed dynamic scheduling," *SIAM Journal on Matrix Analysis and Applications*, vol. 23, no. 1, pp. 15–41, 2001.

[38] O. E. Jensen, "The spreading of insoluble surfactant at the free surface of a deep fluid layer," *Journal of Fluid Mechanics*, vol. 293, p. 349378, 1995.

[39] M.-J. Huang, J. Schofield, and R. Kapral, "Chemotactic and hydrodynamic effects on collective dynamics of self-diffusiophoretic janus motors," *New Journal of Physics*, vol. 19, no. 12, p. 125003, 2017.

[40] S. Herminghaus, C. C. Maass, C. Krüger, S. Thutupalli, L. Goehring, and C. Bahr, "Interfacial mechanisms in active emulsions," *Soft matter*, vol. 10, no. 36, pp. 7008–7022, 2014.

[41] K. Son, D. R. Brumley, and R. Stocker, "Live from under the lens: exploring microbial motility with dynamic imaging and microfluidics," *Nature Reviews Microbiology*, vol. 13, no. 12, pp. 761–775, 2015.

[42] E. F. Keller and L. A. Segel, "Model for chemotaxis," *Journal of theoretical biology*, vol. 30, no. 2, pp. 225–234, 1971.

[43] I. O. Götze and G. Gompper, "Mesoscale simulations of hydrodynamic squirmer interactions," *Physical Review E*, vol. 82, no. 4, p. 041921, 2010.

[44] L. Stricker, "Numerical simulation of artificial microswimmers driven by marangoni flow," *Journal of Computational Physics*, vol. 347, pp. 467–489, 2017.

[45] S. Thutupalli, R. Seemann, and S. Herminghaus, "Swarming behavior of simple model squirmers," *New Journal of Physics*, vol. 13, no. 7, p. 073021, 2011.

[46] Z. Y. Luo, X. L. Shang, and B. F. Bai, "Marangoni effect on the motion of a droplet covered with insoluble surfactant in a square microchannel," *Physics of Fluids*, vol. 30, no. 7, p. 077101, 2018.

[47] E. Bormashenko, Y. Bormashenko, R. Grynyov, H. Aharoni, G. Whyman, and B. P. Binks, "Self-propulsion of liquid marbles: Leidenfrost-like levitation driven by marangoni flow," *The Journal of Physical Chemistry C*, vol. 119, no. 18, pp. 9910–9915, 2015.